# Lithium intercalation into titanium dichalcogenide single crystals under pressure

Von der Naturwissenschaftlichen Fakultät
der Gottfried Wilhelm Leibniz Universität Hannover
zur Erlangung des Grades
Doktor der Naturwissenschaften
Dr. rer. nat.

genehmigte Dissertation
von
Dipl.-Geow. Robert Knobel
geboren am 26. Januar 1983 in Celle

2013

| | |
|---|---|
| Referent: | Prof. Dr. Harald Behrens |
| Korreferent: | Prof. Dr. Michael Wark |
| Tag der Promotion: | 06.11.2013 |

# Acknowledgements

It goes without saying that this thesis would not have been possible without the help and support of many people.

To begin with, I would like to thank Prof. Dr. Harald Behrens for the encouraging support and for the helpful discussions throughout the work on this thesis and our publications. I also want to thank him, as well as Prof. Dr. Michael Wark, for the examination of my thesis and Prof. Dr. Jürgen Böttcher for chairing the examination committee.

I would like to thank PD Dr. Ingo Horn for the support in the setup of the measurement cell and the instruction in the LASER ablation technique. I also want to thank Dr. Stephan Schuth for the instruction in the operation of the ThermoScientific Element XR mass spectrometer. I want to thank my project partner Nele Schwarzburger who provided high quality crystals and standards materials throughout our project. I would also like to thank the workshop staff who helped in the construction of the high pressure cell and the sample preparation, namely, Ullrich Kroll, Markus Köhler, Fabian Christ, Otto Diedrich and Björn Ecks. What is more, I want to thank Hans-Christoph Schwartz for recording confocal microscopical images of LASER craters at the Laboratory of Nano and Quantum Engineering (LNQE).

Additionally, I would like to thank to thank the proofreaders, Christian Fischer and Lars Schomburg, for their patience in reading this thesis and their valuable feedback.

Special thanks go to my colleagues for the great time I had at the institute. I want to thank André Stechern, Eric Wolff and Alexander Bartels, with whom I spent my lunch breaks over the past years. It has also been a pleasure discussing ornithological questions with them in the park after lunch but I have to admit that I am a bit relieved, having escaped the “death spiral”. I want to thank Anna-Maria Welsch for the many interesting science- and not-so-science-related conversations. I also want to express my appreciation for the enjoyable collaboration in the thermodynamics tutorial. I would like to thank my office colleague Sebastian Roß, who was a helpful discussion partner in scientific questions and VBA programming issues.

I would like to thank my best friends, Christian, Bastian, Dennis, Marcel and Hannes, who could always cheer me up in times I felt frustrated with my work.

I would like to express my deep gratitude to my parents, to whom I owe the most, for their everlasting support and faith.

Finally, I would like to thank my girlfriend Natalie. It is hard to overstate my gratitude for her patience, steady encouragement and support during the finishing of this thesis.

# Kurzfassung

In dieser Studie wurde der Mechanismus der Interkalation von Lithium (Li) in Titan-Dichalkogenid-Einkristalle der Zusammensetzung $TiX_2$ (X = S, Se, Te) untersucht. Insbesondere die Druckabhängigkeit der Interkalationskinetik stand dabei im Fokus der Arbeit. Die Kristalle wurden mit n-Butyllithium (BuLi) in n-Hexan in verschiedenen Versuchsanordnungen als Funktion von hydrostatischem und uniaxialem Druck interkaliert.

Experimente unter hydrostatischem Druck wurden bei unterschiedlicher Interkalationsdauer (5 d und 20 d), Temperatur (293 bis 363 K) und Druck (10 bis 500 MPa) durchgeführt. Für die Interkalation unter uniaxialem Druck wurde eine neue Zelle entwickelt. In den Experimenten wurden $TiS_2$ Proben bei einer Temperatur von ca. 306 K und Drücken von einer Atmosphäre bis zu 885 MPa interkaliert.

Anschließend wurden Lithium-Gehaltsprofile parallel zur kristallographischen *a/b-Ebene* der Proben mittels fs-LA-ICP-OES und -MS (femtosecond-LASER Ablation- Inductively Coupled Plasma-Optical Emission Spectroscopy und -Mass Spectrometry) bestimmt. Die Messung der Proben erfolgte in einer Vakuum Heiz- und Kühlzelle (Instec HCS621V), die für eine Verwendung als Ablationszelle modifiziert wurde.

Nach den Experimenten wurde bei einem Teil der Proben ein Aufblättern der $TiX_2$-Schichten sowie Risse in den Schichten beobachtet. Solche Proben zeigten häufig einen gestörten Profilverlauf. Proben ohne sichtbare Degradationserscheinungen lieferten Profile mit der Form einer Fehlerfunktion. Diese wurden an die spezifische Lösung des zweiten Fick'schen Gesetzes für die gegebenen Randbedingungen angeglichen. Aus den Anpassungen wurden Lithium-Diffusivitäten ($D_{Li}$) sowie Lithium-Gehalte am Rand der Proben ($x_{Li,S}$) ermittelt.

Bei der Auswertung wurde eine künstliche Verlängerung der Profile korrigiert, die aus der Größe des LASER Spots während der Ablation resultiert. Anhand von Modellrechnungen wurde eine Korrekturformel für Diffusionskoeffizienten bestimmt. Die Modellrechnungen konnten experimentell bestätigt werden.

Aufgrund der Degradationserscheinungen konnten aus den hydrostatischen Experimenten nicht für alle Versuchsbedingungen Werte für $D_{Li}$ und $x_{Li,S}$ erhalten werden. Bei 500 MPa und Raumtemperatur ergeben sich ähnliche Werte für die Lithium-Diffusivitäten in $TiS_2$ ((1.07 bis 2.41) $\cdot 10^{-15}$ $m^2 \cdot s^{-1}$) und $TiSe_2$ ((1.48 bis 2.10) $\cdot$ $10^{-15}$ $m^2 \cdot s^{-1}$), während die Diffusivität in $TiTe_2$ deutlich geringer ist ((0.07 bis 0.55) $\cdot$ $10^{-15}$ $m^2 \cdot s^{-1}$). Zudem nimmt die Li-Diffusivität in $TiTe_2$ signifikant mit zunehmendem Druck ab. Die Lithium-Randgehalte sind in $TiS_2$ (x = 0.15 bis 0.36) kleiner im Vergleich zu $TiSe_2$ (0.66 bis 0.71) und $TiTe_2$ (0.59 bis 0.99).

Aus den Experimenten unter uniaxialem Druck konnten Werte für $D_{Li}$ (1.2 bis 4.7 $\cdot$ $10^{-15}$ $m^2 \cdot s^{-1}$) und $x_{Li,S}$ (0.12 bis 0.22) zwischen Atmosphärendruck und 885 MPa bestimmt werden. Die Werte zeigen keine signifikante Druckabhängigkeit.

Die Diffusivitäten, die in dieser Arbeit bestimmt wurden, liegen im unteren Bereich der Diffusivitäten, die durch Schwarzburger [2013] unter Atmosphärendruck bestimmt wurden ($D_{Li,TiS2}$ = (0.12 bis 1.04) $\cdot 10^{-14}$ $m^2 \cdot s^{-1}$, $D_{Li,TiSe2}$ = (0.52 bis 1.14) $\cdot 10^{-14}$ $m^2 \cdot s^{-1}$, $D_{Li,TiTe2}$ = (0.10 bis 0.48) $\cdot 10^{-14}$ $m^2 \cdot s^{-1}$). Die $x_{Li,S}$ Werte aus den hydrostatischen Experimenten sind leicht erhöht gegenüber den Experimenten von Schwarzburger [2013] sowie bei uniaxialem Druck.

Die Ergebnisse dieser Arbeit deuten darauf hin, dass die Ionizität der Ti-X Bindung sowie die Größe der Zwischenschicht-Lücke (van der Waals Lücke) der verschiedenen Titan-Dichalkogenide eine entscheidende Rolle bei dem Einbau von Lithium und der Druckabhängigkeit der Diffusivität spielen.

**Schlagwörter**: Interkalation, Diffusion, Lithium

# Abstract

In this thesis the mechanisms of lithium (Li) intercalation in titanium dichalcogenide single crystals $TiX_2$ (X = S, Se, Te) were investigated, with a main emphasis on the pressure dependence of intercalation kinetics. The samples were intercalated with n-butyl lithium (BuLi) in n-hexane in different experimental settings under hydrostatic and uniaxial pressure.

The hydrostatic intercalation experiments were conducted at variable experimental durations (5 d and 20 d), temperature (293 to 363 K) and pressure (10 to 500 MPa). A new cell was developed for the intercalation experiments under uniaxial pressure. In the experiments $TiS_2$ samples were intercalated at a temperature of approx. 306 K and pressures between 0.1 MPa (atmospheric pressure) to 885 MPa.

After the hydrostatic and uniaxial pressure experiments, lithium content profiles were measured parallel to the crystallographic *ab-plane*, using femtosecond-LASER Ablation-Inductively Coupled Plasma-Optical Emission Spectroscopy and -Mass Spectrometry (fs-LA-ICP-OES and -MS). The samples were analyzed in a vaccuum heating and cooling stage (Instec HCS621V), which was modified to be used as an ablation cell.

At a part of the samples fanning of the $TiX_2$ layers, as well as formation of cracks in the layers was observed after the experiments. The content-distance profiles of samples, at which signs of degradation were observed often showed a strong deviation from error function shape. Samples without visible signs of degradation yielded profiles that could be fitted well to the specific solution of Fick's second law for the given boundary conditions. Lithium diffusivities ($D_{Li}$) and lithium contents at the crystal edges ($x_{Li,S}$) were determined from the fits.

An artificial elongation of the profiles, which results from the size of the LASER spot during ablation, was corrected. A correction formula for the diffusion coefficients was developed on the basis of model calculations. These model calculations could be confirmed experimentally.

Because of the sample degradation, values for $D_{Li}$ and $x_{Li,S}$ could not be determined for all experimental conditions. At 500 MPa and room temperature lithium diffusivities are in the same range for $TiS_2$ ((1.07 to 2.41) $\cdot 10^{-15}$ $m^2 \cdot s^{-1}$) and $TiSe_2$ ((1.48 to 2.10) $\cdot 10^{-15}$ $m^2 \cdot s^{-1}$), while lithium diffusivity in $TiTe_2$ is significantly lower ((0.07 to 0.55) $\cdot 10^{-15}$ $m^2 \cdot s^{-1}$). Moreover, diffusivities of Li in $TiTe_2$ decrease significantly with increasing pressure. Lithium surface contents are lower for $TiS_2$ (x = 0.15 to 0.36) than for $TiSe_2$ (0.66 to 0.71) and $TiTe_2$ (0.59 to 0.99).

From experiments under uniaxial pressure values for lithium diffusivities ($D_{Li}$ = 1.2 to 4.7 $\cdot 10^{-15}$ $m^2 \cdot s^{-1}$) and lithium surface contents ($x_{Li,S}$ = 0.12 to 0.22) could be determined for $TiS_2$ at all experimental conditions. These values do not show significant pressure dependence.

Diffusivities that are presented in this work are in the lower range of diffusivities determined by Schwarzburger [2013] at ambient pressure ($D_{Li,TiS2}$ = (0.12 to 1.04) $\cdot 10^{-14}$ $m^2 \cdot s^{-1}$, $D_{Li,TiSe2}$ = (0.52 to 1.14) $\cdot 10^{-14}$ $m^2 \cdot s^{-1}$, $D_{Li,TiTe2}$ = (0.10 to 0.48) $\cdot 10^{-14}$ $m^2 \cdot s^{-1}$). Lithium surface contents from hydrostatic experiments are slightly elevated compared to ambient pressure experiments as well as uniaxial pressure experiments.

The findings presented in this work indicate, that the ionicity of the Ti-X bonding as well as the size of the interlayer space (van der Waals gap) of the different titanium dichalcogenides play a crucial role for the insertion of lithium and the pressure dependence of diffusivity.

**Keywords:** Intercalation, Diffusion, Lithium

# Table of contents

# List of figures

# List of tables

# List of abbreviations

| | |
|---|---|
| *a* | Crystallographic *a*-axis |
| *b* | Crystallographic *b*-axis |
| BuLi | n-Butyllithium |
| *c* | Crystallographic *c*-axis |
| C | Concentration |
| *cps* | Counts per second |
| *d* | Distance |
| d | Day |
| *D* | Diffusion coefficient |
| EDX | Energy-dispersive X-ray spectroscopy |
| erf | Error function |
| fs | Femtosecond |
| Hz | Hertz |
| ICP | Inductively coupled plasma |
| *I* | Intensity |
| K | Kelvin |
| L | Litre |
| LA | Laser-Ablation |
| M | Molar concentration |
| MS | Mass spectrometer |
| min | Minute |
| OES | Optical emission spectroscopy |
| *P* | Pressure |
| X | S, Se oder Te |
| *r* | Radius |
| *t* | Experimental duration |
| *T* | Temperature in K |
| s | Second |
| $\tilde{\upsilon}$ | Wave number |
| *V* | Volume |
| *x* | Orientation in space |
| $x_S$(Li) | Stoichiometric factor of lithium in $Li_xTiX_2$ at the edge of the crystal |
| $x_0$ | Stoichiometric factor of lithium in $Li_xTiX_2$ in the interior of the crystal |
| *y* | Orientation in space |
| *y* | Non-stoichiometry in $Ti_{1+y}X_2$ |
| *z* | Orientation in space |

| | |
|---|---|
| $z$ | Ratio of LASER spot diameter over profile length |
| Å | Angström |
| Ø | Diameter |
| $\eta$ | Viscosity |
| $f$ | Frequency |
| $\sigma$ | Standard deviation |

# Preface

Rechargeable batteries play an important role as energy storage materials, especially for portable devices that demand a constant and significant power supply such as mobile phones or laptops. The lithium-ion battery is a member of the family of rechargeable batteries. In these batteries intercalation compounds are used as electrode materials. The process of intercalation is a reversible insertion of molecules, atoms or ions into a host material. In the case of lithium-ion batteries, lithium-ions are intercalated into the positive electrode during discharge and intercalated into the negative electrode during charge (Fig. 1).

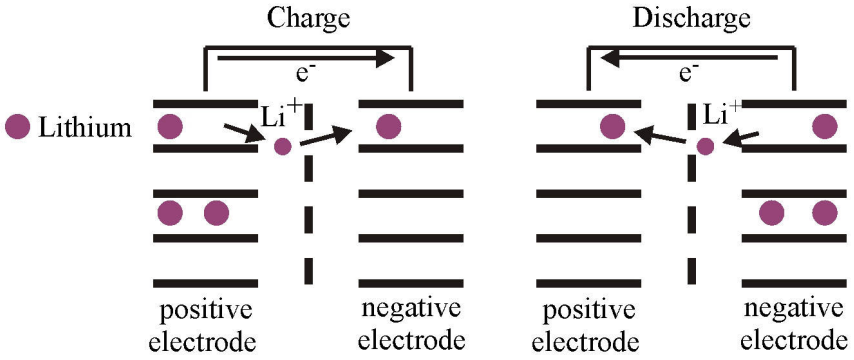


Fig. 1: Schematic drawing of the charge and discharge of a lithium-ion battery.

A big part of the research on cathode materials for lithium-ion batteries focused on layered materials such as $LiVSe_2$, $LiCoO_2$, $LiNiO_2$, $LiNi_yMn_yCo_{1-2y}O_2$ and $LiTiS_2$ [Whittingham 2004]. Among the layered dichalcogenides $LiTiS_2$ was the most appealing because it is the lightest [Whittingham 2004]. Therefore many investigations have already been made on the intercalation process of Li in $TiS_2$ and on properties of the intercalation product $Li_xTiS_2$ ($0.07 \leq x \leq 1.03$) including NMR spectrometric studies on Li self diffusion [Kleinberg and Silbernagel 1980, Folinsbee et al. 1986, Matsumoto and Nagai 1987, Wilkening 2005, Wilkening et al. 2006, Wilkening and Heitjans 2008].

However, the kinetics of intercalation still is poorly understood. A comparative experimental study of intercalation kinetics in dependence on the anion in the isostructural compounds $TiX_2$ (with X = S, Se, Te), which has not been performed so far, could provide new information on the process. Experimental studies investigating the intercalation compounds of $TiSe_2$ [Bensch et al. 2009, Patel and Balchin 1983, Silbernagel 1975] and especially $TiTe_2$ are rare [Patel and Balchin 1985].

In the studies named above fine-grained crystalline powders were used and chemical diffusion of lithium played a minor role. Though, in some studies titanium dichalcogenide single crystals were intercalated [Whittingham 1976, Chianelli 1976, Hibma 1980, Jaegermann et al. 1994, Klipstein et al. 1987] indicating strain effects during intercalation of single crystals, i.e. formation of cracks [Chianelli 1976] and inhomogenous intercalation degrees [Hibma 1980].

Therefore, elaborated investigations of chemical diffusion coefficients in $TiS_2$ single crystals were conducted by Schwarzburger et al. [2012]. These studies revealed that strain induced by the intercalation are also important for the intercalation kinetics. Moreover, the chemical intercalation of lithium often led to degradation of the crystals. In particular, cleavages parallel to the sheets reached deeply into crystals. As a consequence, some of the measured lithium content distance profiles resulted from a superposition of lithium solid state diffusion and migration of the liquid into fractures and thus yielded elevated diffusion coefficients.

The aim of this work is to study the mechanisms and the kinetics of intercalation with a focus being on the role of the expansion of the host lattice as well as the influence of the anion in the host lattice on intercalation kinetics.

Therefore the isostructural compounds $TiX_2$ (X = S, Se, Te) are studied as model materials. A theoretical introduction about these compounds, the process of intercalation and the effect of pressure application on titanium dichalcogenides is given in PART A of this thesis.

Single crystals of the dichalcogenides were intercalated chemically with n-Butyllithium in n-hexane as lithium source. Subsequently, space resolved measurements of lithium contents in the crystals were conducted. To reduce diffusion of lithium in the crystals during the analytical session, it was necessary to cool the samples. For this purpose, a commercially available cooling stage was modified to be used as an ablation cell. Details of the analytical techniques as well as the starting materials and their characterisation are presented in Part B.

As the LASER spot was often large compared to the profile length, two effects of the spot diameter on the measured profiles were considered, i.e. an artificial elongation of the profiles and the uncertainty of the position of the crystal edge in the profiles. A correction for the artificial elongation and a procedure to define the edge position were developed, which are also described in PART B.

The findings are published in an abridged version in [Schwarzburger et al. 2012] while PART B of this thesis gives a detailed description and discussion.

The experiments were conducted under application of hydrostatic and uniaxial pressure. The application of pressure counteracts the expansion of the crystal lattice, which is why these experiments can provide information about its role for the intercalation kinetics. Moreover, the application of pressure counteracts the splitting of the single crystals parallel to the sheets, which led to a superposition of different transport processes in ambient pressure studies [Schwarzburger et al. 2012], i.e. migration of the solution and solid state diffusion. However, samples intercalated at high pressures also show fanning of the crystal sheets, albeit less severe compared to ambient pressure. Therefore an accurate assessment of the samples using optical microscopy was crucial, as well as an assessment of each measured profile for local degradation is not necessarily visible in microscopic images. A new cell was developed for intercalation experiments under uniaxial pressure. Experimental details as well as results and conclusions related to our initial objectives are presented in PART C (hydrostatic pressure experiments) and PART D (uniaxial pressure experiments).

A summary is given at the end of this thesis.

# Part A - Basics: Properties of titanium dichalcogenides, the mechanisms of lithium intercalation and the effect of pressure application

## A.1 Titanium dichalcogenides $TiX_2$ (X = S, Se, Te)

The three isostructural compounds $TiS_2$, $TiSe_2$ and $TiTe_2$ were used in this work. They exhibit a $CdI_2$ type crystal structure (space group P3m1) in which Ti cations are coordinated octahedrally by chalcogen anions. The Ti cations fill all octahedral positions in alternate layers, so that X-Ti-X sheets are formed through covalent bonds. Adjacent sheets are weakly bonded by van der Waals forces. Therefore the gap between the X-Ti-X sheets is often called van der Waals gap. The structure of the dichalcogenides is displayed in Fig. 2.

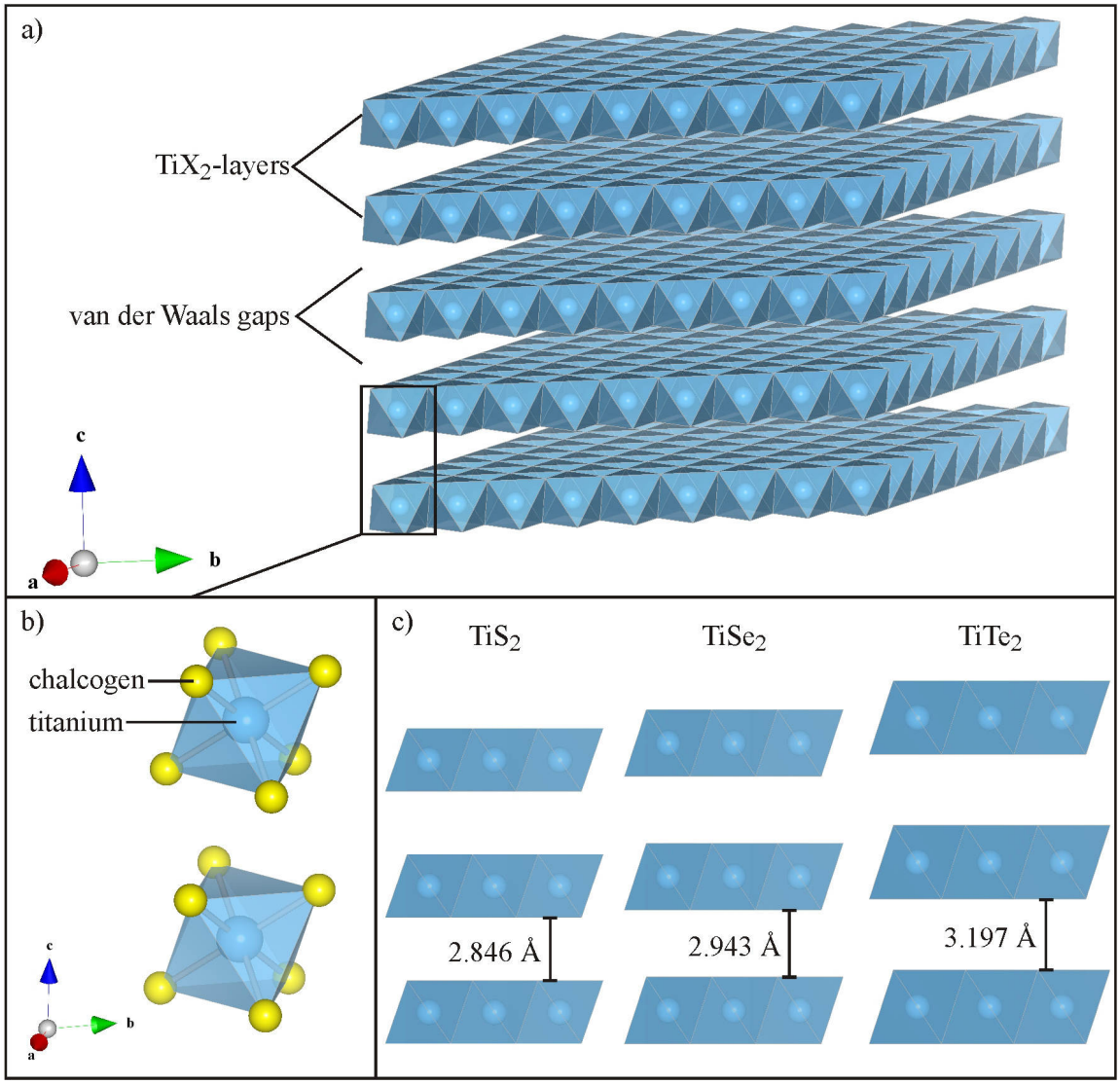


Fig. 2: Illustrations of the $TiX_2$ crystal structures. a) shows several $TiX_2$ layers and the van der Waals gaps between the layers. b) shows two $TiX_6$ octahedra above each other. It can be seen that the stacking sequence of the chalcogen layers in direction of the crystallographic *c-axis* is ABAB. c) illustrates the different sizes of the $TiX_2$ layers and the van der Waals gaps for the different dichalcogenides. The actual size of the ions in the structure is not considered in the illustrations.

Due to the weak bonding, foreign atoms can be inserted into the van der Waals gap, i.e. intercalation. The bonding anisotropy also results in anisotropy of physical properties like electronic and ion conductivity and compressibility. Therefore the layered chalcogenides are often referred to as two dimensional materials. The diffusivity of ions is higher along the sheets by several orders of magnitude than perpendicular to them [Schwarzburger et al. 2012]. The compressibility is much higher perpendicular to the sheets, which can basically be ascribed to a compression of the van der Waals gap, while the sheets themselves are less compressible due to covalent bonding. The properties of the chalcogenides vary in dependence of the size of the chalcogen anions. Therefore, the chalcogenides are described below in the order of their period in the periodic table.

### A.1.1 $TiS_2$

Among the compounds used in this work, titanium disulphide possesses the smallest anion in the structure with the highest electronegativity. It is also the lightest and has the smallest unit cell. The lattice parameters are $a$ = 3.41 Å and $c$ = 5.69 Å. The interlayer distance, i.e. the width of the van der Waals gap is 2.846 Å. $TiS_2$ was reported to exhibit semiconducting properties [Wiegers 1980, Friend et al. 1982, Klipstein et al. 1981, Clerc et al. 1996, Doublet et al. 1998], but was also be reported to be semimetallic more recently [Fang et al. 1997, Reshak and Auluck 2003]. The ionicity of the Ti-S bond was reported to be approx. 22 % [Hibma 1980]. The stiffness in the direction of the *c-axis* (55 GPa) is higher compared to $TiSe_2$ [Schärli and Levy 1986]. This is probably due to the higher electrostatic repulsion, because of the higher charge of the chalcogen layers.

### A.1.2 $TiSe_2$

The lattice parameters of $TiSe_2$ are $a$ = 3.540 Å and $c$ = 6.008 Å and the interlayer distance is 2.943 Å. Titanium diselenide is a semimetall [Friend et al. 1982, Klipstein et al. 1981, Doublet et al. 1998, Fang et al. 1997]. The ionicity of the Ti-Se bond was reported to be approx. 18 % [Hibma 1982]. The stiffness in the direction of the c-axis is 39 GPa [Stirling et al. 1976].

### A.1.3 $TiTe_2$

Tellurium is the largest of the anion of the chalcogenides in this study. The lattice parameters of $TiTe_2$ are $a$ = 3.777 Å and $c$ = 6.498 Å and the interlayer distance is 2.943 Å. Titanium ditelluride was reported to possess metallic properties [Doublet et al. 1998]. The Ti-Te bond was reported to be closer to neutrality compared to the other chalcogenides with an ionicity of approx. 9 % [Hibma 1982], which is consistent with the lower difference in electronegativity between titanium and tellurium. Moreover, Kim et al. reported a higher bond overlap population for the interlayer Te-Te bond, which indicates a stronger bonding [1998]. No data about the compressibility were available to us, but it is expected to be higher compared to the other chalcogenides, as the electrostatic repulsion between the layers is lower.

## A.2 The process of intercalation

In this work single crystals of the layered chalcogenides were intercalated chemically using n-butyl lithium (BuLi) dissolved in n-hexane as the source of lithium. The mechanism of this reaction can be divided into several steps. Fig. 3 shows these schematically on the basis of a model presented by Levy et al. [1979] with further findings from isotope exchange studies by Schwarzburger [2013] included.

The adapted model of the intercalation process includes the following steps:

(1) Transport of n-butyl lithium in the liquid to the crystal;

(2) Chemisorption of BuLi on the crystal surface;

(3) Hopping of butyl radicals between lithium atoms at the crystal surface;

(4) Combination of two butyl radicals forming octane at the crystal surface and charge transfer from lithium to the host lattice;

(5) Expansion of the host lattice, incorporation of lithium ions in the host material and chemical diffusion into the crystal.

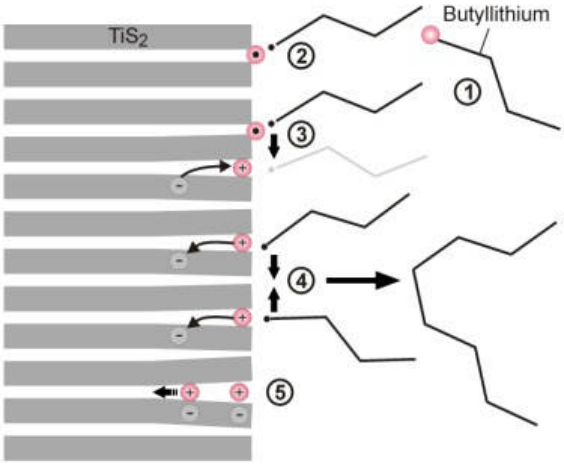


Fig. 3: Schematic illustration of the fundamental steps during lithium intercalation.

The comparative studies presented here provide information about the rate of lithium insertion, as well as the intercalation degree in dependence on the experimental conditions and the type of anion. A better understanding of the mechanisms in the intercalation process can be fostered when the experimental findings are related to the steps of the intercalation process. The steps are described in the following with regard to the conducted experiments.

### A.2.1 Transport of lithium to the crystal surface

The first step of intercalation is the transport of BuLi to the surface of the crystal. To discuss the question, whether the transport in the solution is fast enough to provide sufficient supply of Li to the crystal surface a comparative consideration was made. If the product of concentration times diffusivity (C · D) at the crystal/liquid interface is larger for the liquid than for the crystal, and if transport controls the intercalation process, lithium inserted in the crystal surface will rapidly migrate into the crystal interior. Thus, the remaining concentration of lithium in the surface is low compared to the equilibrium concentration.

Assuming a non-convective system, low transport rates in the liquid (step 1) can originate either from low Li concentration or low diffusivity of the Li-species or both. The diffusion coefficient of butyl lithium in n-hexane has been estimated according to Stoke's Law:

$$D_{BuLi} = \frac{k \cdot T}{6 \cdot \pi \cdot \eta \cdot r} \qquad (1)$$

where $k$ is the Boltzmann constant, T is the temperature, η is the viscosity of n-hexane and r is the hydrodynamic radius of the moving species.

In the hydrostatic pressure experiments both the samples and the solution is under pressure. As viscosity data for n-hexane were only available for pressures up to 100 MPa [Lemmon et al. 2012], values for higher pressures were estimated by linear extrapolation up to 500 MPa (Fig. 4).

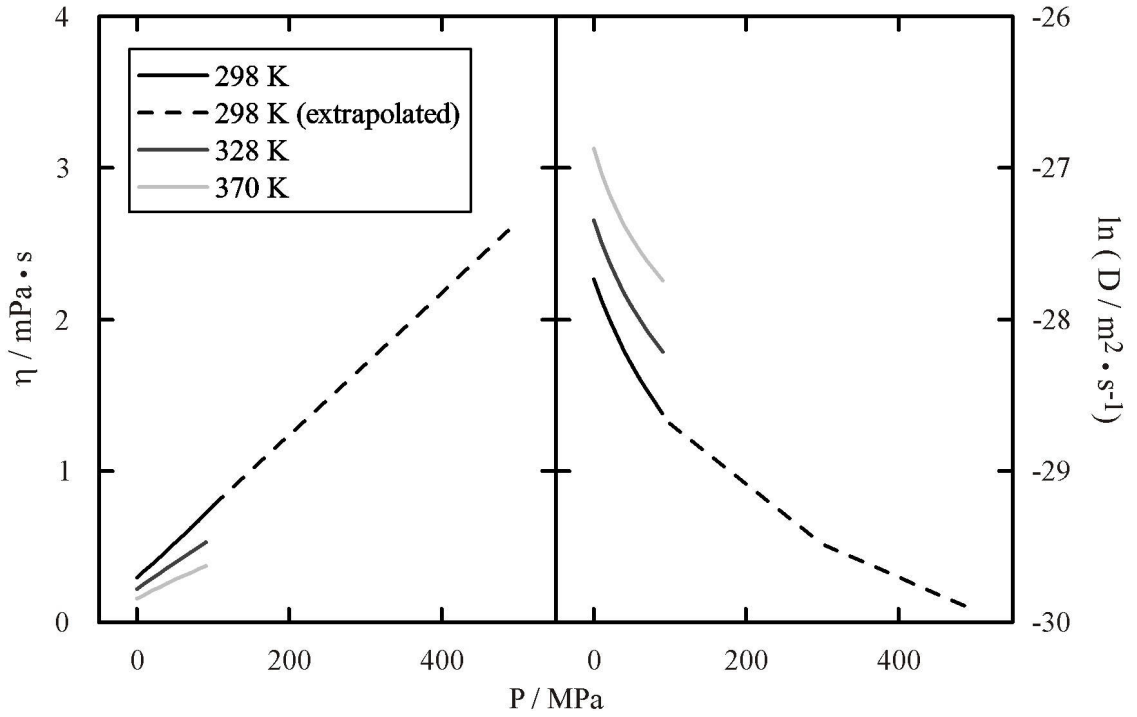


Fig. 4: Viscosity of n-hexane [Lemmon et al. 2012] and corresponding diffusivities of hexameric BuLi clusters in n-hexane.

The hydrodynamic radius has been estimated to be approx. 800 pm, assuming butyl lithium molecules to move as hexameric clusters in the solution [Kottke and Stalke 1993].

A worst case scenario was considered to show that a sufficient supply can be provided by diffusive lithium transport in the solution, i.e. lowest supply of Li in the solution and fastest uptake of lithium into the crystals. However, the convective Li transport in the liquid is probably much faster.

### A.2.2 Chemisorption and charge transfer from Li to the host lattice

More crucial for the intercalation kinetics are the chemisorption and the charge transfer of Li to the host lattice.

Isotope exchange studies [Schwarzburger 2013] provided information about these steps. Titanium disulfide crystals were intercalated using BuLi, with an isotope ratio that was assumed to be natural (7.59 % $^{6}$Li and 92.41% $^{7}$Li), and homogenized. The crystals were then inserted into an enriched Bu$^{6}$Li solution. The resulting profiles showed that $^{7}$Li was depleted at the crystal edge and increased to the interior where it reached the initial value, while the $^{6}$Li content was enriched at the crystal edge and decreased to the interior. The overall lithium content stayed constant with the distance to the crystal edge (the initial lithium content, which was approx. 0.5 wt %). This means that $^{7}$Li in the crystal was exchanged by $^{6}$Li from the solution. This exchange reaction shows that the intercalation of Li is reversible. Thus, butyl radicals do not necessarily recombine directly to form octane but can also react with Li from the crystal. At high BuLi concentrations the probability of butyl radicals recombining is higher. This could be rate-determining, provided lithium diffuses readily into the crystal after the recombination.

Intercalation experiments were conducted in dependence of the BuLi concentration by Schwarzburger et al. [2012]. Lithium transport reached deeper into the crystals at high concentrations of the solution. However, a stronger degradation of the crystals was observed at higher BuLi concentrations. This degradation results in the solid state diffusion being superimposed by penetration of the fluid into the crystals. Thus, it was not possible to quantify the impact of this step for the kinetics in form of concentration dependent diffusion coefficients.

The charge transfer of lithium to the host lattice is the driving force of the intercalation process. The energy gain from charge transfer differs for the different chalcogenides and will therefore affect the

intercalation kinetics. An inhomogeneous insertion during the intercalation in $TiS_2$ single crystals was observed by Schwarzburger et al. [2012]. In other words: the insertion preferably took place at sites that had already been intercalated. This can be ascribed to less strain energy that is needed at these sites to expand the van der Waals gap, which is discussed in detail below (A.2.3). Strictly speaking, the difference in energy gain from electron transfer, and the energy that is required to expand the gap is determining whether expanded sites are preferred or not. However, data for the energy gain have not been available to us until now. Therefore profound analyses of these effects will not be possible.

According to calculations by Nagelberg and Worrel [1981] the chemical potential of Li intercalated in titanium disulfide is also determined by the repulsive interaction between intercalated ions. The charge transfer leads to an ionization of Li atoms. The contribution of the repulsive interaction between intercalated atoms is proportional to the fraction of sites that is occupied and the degree of ionization of the intercalant ion. The repulsive interaction between the positive intercalant is screened by the chalcogen electrons in the van der Waals gap.

Previous studies reported that the charge transfer of Li to the host structures of $TiS_2$ [e.g. Silbernagel 1975, Umrigar et al. 1982, Clerc et al. 1997] and $TiSe_2$ [Jaegermann et al. 1994] is close to 1 electron per intercalated Li atom, which is located in the vicinity of sulphur in the case of $TiS_2$. Hence, the ionization is similar for these compounds. The repulsive interaction decreases with the distance between two intercalated atoms. For two nearest neighbours this is given by the lattice parameter *a*, which increases from S to Te. From $TiS_2$ to $TiSe_2$ the lattice parameter *a* increases by approx. 4%, and we assume that the repulsive interaction is similar for both compounds.

It is expected that the repulsive interaction between the intercalated lithium ions are important in homogenous media rather than for our experimental constraints, i.e. a concentration gradient.

### A.2.3 Incorporation of lithium ions in $TiX_2$ and expansion of the lattice

The intercalation of Li into the van der Waals gaps of $TiX_2$ is accompanied by structural changes. However, the crystal symmetry remains unchanged for all chalcogenides. The most prominent structural change is the expansion of the lattice parallel to the crystallographic *c-axis* with increasing x in $Li_xTiX_2$. Using periodic Hartree-Fock studies, Clerc et al. [1997] demonstrated for $TiS_2$ that this is mainly due to an expansion of the Van der Waals gap (increase by 0.49 Å between $x = 0$ and $x = 1$). At high *x* values an additional contribution results from expansion of the S-Ti-S-layers (up to 0.1 Å). The lattice expansion at full intercalation is lower for $TiSe_2$ with 0.48 Å [Rimmington and Balchin 1974] and $TiTe_2$ with 0.41 Å [Patel and Balchin 1985] due to the size of the van der Waals gap which is initially larger (A.1). The increase of the *c* lattice parameter in dependence of x in $Li_xTiX_2$ is given in Fig. 5:

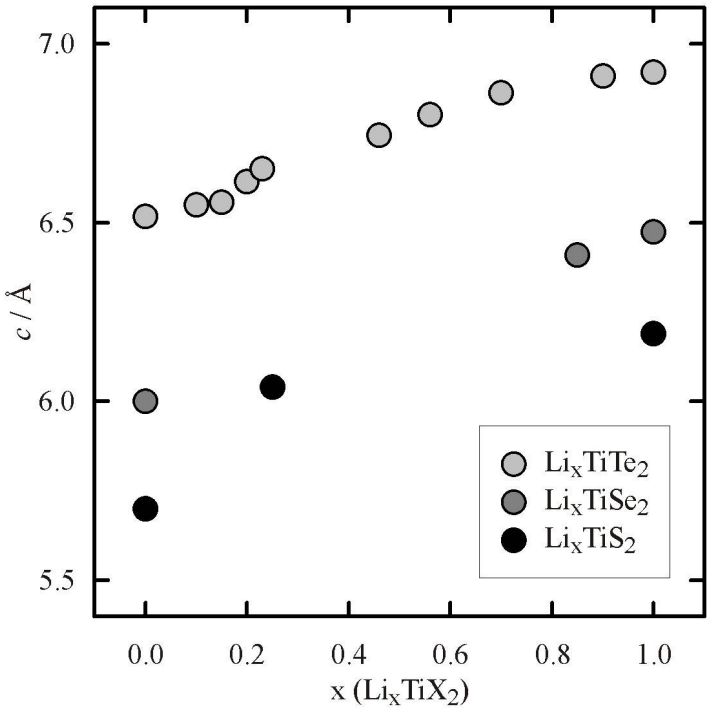


Fig. 5: The lattice parameter *c* in dependence of the intercalation degree of $Li_xTiS_2$ [value for $TiS_2$ from Chianelli et al. 1975 and values for $Li_{0.25}TiS_2$ and $LiTiS_2$ from Dahn et al. 1980], $Li_xTiSe_2$ [Patel and Balchin 1983] and $Li_xTiTe_2$ [Patel and Balchin 1985].

The expansion of the lattice is responsible for the formation of stage structures, i.e. intercalation of only a fraction of van der Waals layers and formation of alkali-rich regions within layers. Hibma [1980] observed stage structures in sodium intercalated $TiS_2$, but did not observe stages in lithium intercalated $TiS_2$. However, Dahn and Haering [1981] found indications for short-range stage structures for lithium intercalated $TiS_2$ at low Li concentrations (near $Li_{0.16}TiS_2$) in X-ray diffraction experiments. This was consistent with their Monte Carlo simulations [1982] which predicted short-range stage structures for $x = 0.16$. Stage structures can be explained by strain-mediated attractive interactions between intercalated ions within a van der Waals gap and repulsive interactions between ions in neighboring layers [McKinnon and Haering 1980].

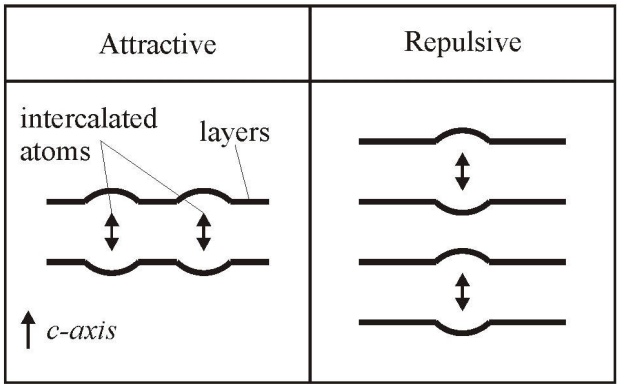


Fig. 6: Schematic illustration of strain-induced interactions in layered compounds according to McKinnon and Haering [1980].

While strain-mediated attractive interactions arise from less energy that is needed at sites that have already been expanded by lithium insertion, strain-mediated repulsive interactions arise from a deformation of neighbouring layers. It was observed that lithium is intercalated inhomogeneously into $TiS_2$

single crystals in intercalation experiments at ambient pressure [Schwarzburger et al. 2012], which was attributed to the described interactions. The energy that is needed for intercalation depends on the total expansion of the van der Waals gap on the one hand, as on the interlayer bonding energy on the other hand. These parameters vary for the different chalcogenides as does the energy gain from the electron transfer (A.2.2). Therefore strain-mediated interaction will influence the intercalation into the dichalcogenides differently.

The van der Waals interlayer binding strength is only 15.9 kJ · $mol^{-1}$ for $TiS_2$ at ambient pressure [Clerc et al. 1996]. A decrease of the binding strength with increasing interlayer distances can be expected upon intercalation, provided the bonding type does not change, i.e. at a low degree of intercalation. Hence, the bonds between the layers can be broken up easily. The stability of the $TiX_2$ sheets will strongly depend on the properties of the chalcogenides.

## A.3 Application of pressure onto titanium dichalcogenides and possible effects on the intercalation kinetics

The application of pressure can have several effects on the crystal structure as well as the electronic structure of dichalcogenides. Several authors observed pressure induced phase transitions for $TiS_2$. Aksoy et al. [2009] reported a phase transition at 20.7 GPa and Yu and Ross [2011] reported transitions at 15.1 GPa from $CdI_2$-type trigonal phase to the orthorhombic cotunnite-type phase and at 45.0 GPa to a tetragonal phase. Allan et al. [1998] did not find any evidence for a structural phase transition at pressures below 8 GPa but a semiconductor to semimetal phase transition between 4 and 6 GPa, which was also reported by Klipstein and Friend et al. [1982] at 4 GPa. Thus, the reported phase transitions were observed at much higher pressures compared to this work.

Liu et al. [2011] investigated the pressure effect on $TiS_2$ by in situ resistivity and Hall effect measurements. They found that the resistivity decreases and the electron density increases linearly with increasing pressure to 14.19 GPa. The increase of electron density (approx. 2.0 to 5.8 · $10^{20}$ $cm^{-3}$ from 0 to 14.19 GPa) was assigned to a pressure-induced ionization of impurity levels. The decrease of resistivity and the increase of the electron density might affect the intercalation kinetics.

When hydrostatic pressure below 1 GPa is applied on $TiS_2$ powder samples the compression of the crystal lattice is about nine times stronger parallel to the *c-axis* than perpendicular to the *c-axis* [Allan et al. 1998] because of the elastic anisotropy of the dichalcogenides. However, pressure dependent lattice parameters are only available for the compression of $TiS_2$. The data is given in the experimental section. The samples are compressed prior to the intercalation in the experiments presented in this work. This might affect the intercalation kinetics as more energy is needed to expand the lattice. Moreover, the stability of the samples could be enhanced as the applied pressure counteracts fanning of the $TiX_2$ sheets.

The effect of pressure on the diffusion coefficient can be estimated assuming the activation volume to be of the size of the migrating species:

$$\frac{D}{D_0} = e^{\left(-\frac{\Delta P \cdot V_a}{R \cdot T}\right)} \qquad (2)$$

where $D / D_0$ is the ratio of the diffusion coefficients when the pressure is increased by $\Delta P$ and $V_a$ is the activation volume. Fig. 7 shows the expected pressure effect that was calculated with Equation 1 for the range of applied pressures in this study.

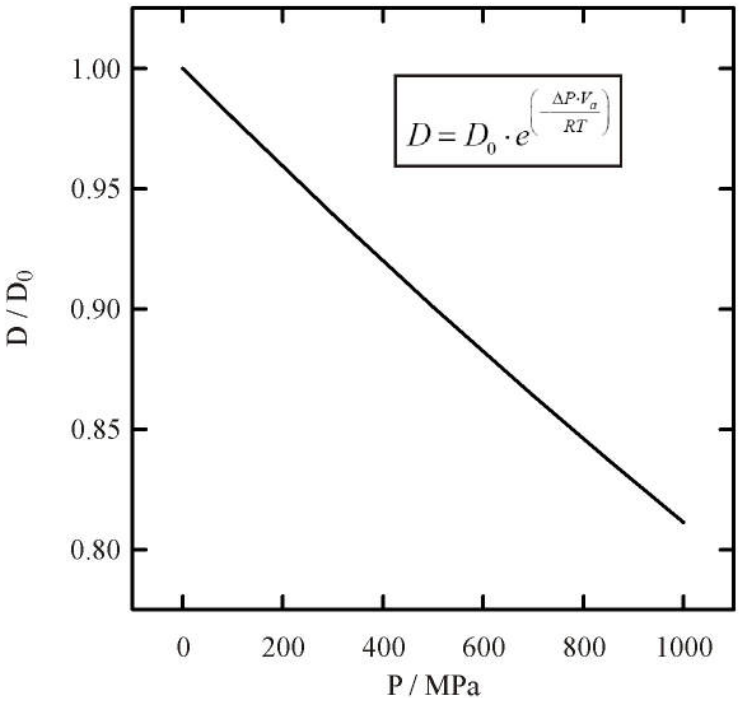


Fig. 7: Expected pressure effect in the range of this thesis. Calculation of the diffusivities is based on the activation volume of lithium, which was estimated from the ionic radius of $Li^+$ [Shannon 1976]. A temperature of 298 K was used in the calculation. The exponential trend of the curve is not visible in the displayed pressure range.

Hydrostatic pressure experiments that are presented in this thesis were limited to a pressure of 500 MPa and n-BuLi solution was also under pressure during experiments. The new high pressure cell allows conducting experiments at much higher and unidirectional pressures. The amount of pressure that can be applied onto the samples is basically limited by the stability of the samples.

# Part B - Characterisation of materials and measurement of profiles

## B.1 Titanium dichalcogenides single crystals

### B.1.1 Synthesis

$TiX_2$ was produced by iodine vapor transport by N. Schwarzburger. Details are given in [Schwarzburger 2013]. A mixture of titanium and chalcogen powders in the ratio 1:2.1 and a small amount of iodine (Li Sigma Aldrich, 99.9%; S, Sigma Aldrich, 99.99 %; Se, Sigma Aldrich, 99.98 %; Te, Sigma Aldrich, 99.98 %; Ti, ABCR, 99.95 %) were heated for 24 h at 720 K in a silica glass ampoule. Afterwards, the ampoule was transferred into a temperature-gradient furnace, and a temperature T difference from 1170 to 1070 K was adjusted along the 20 cm long ampoule.

Large crystals were formed within four ($TiS_2$) and two weeks ($TiSe_2$ and $TiTe_2$). $TiS_2$ crystals were gold-colored slabs, mostly between 20 and 300 µm thick. $TiSe_2$ crystals were thicker (100 to 700 µm) and violet. $TiTe_2$ crystals were grey slabs and ranged from about 100 to 500 µm in thickness.

### B.1.2 Characterisation

One or two crystals of each synthesis charge were ground and analyzed by N. Schwarzburger using powder X-ray diffraction (Stoe Stadi P). Diffractograms were consistent with literature data for the desired structures [Schwarzburger 2013].

The stoichiometry of several charges of $TiS_2$ crystals was tested by FTIR measurements in the mid-infrared (MIR), using a Bruker IFS 88 FTIR spectrometer coupled with an IR-Scope II microscope. 50 scans were recorded per spectra with a resolution of the 4 $cm^{-1}$ and intensities were divided by background intensities, which were recorded using an aluminium mirror, to calculate sample reflectivity. A rectangular slit with an edge length of approx. 100 µm was used in the beamline. The samples were placed in an acrylic sample chamber that was purged with nitrogen gas during the measurement. IR reflectance spectra of $TiS_2$ show a well-defined minimum in reflectivity (Fig. 8).

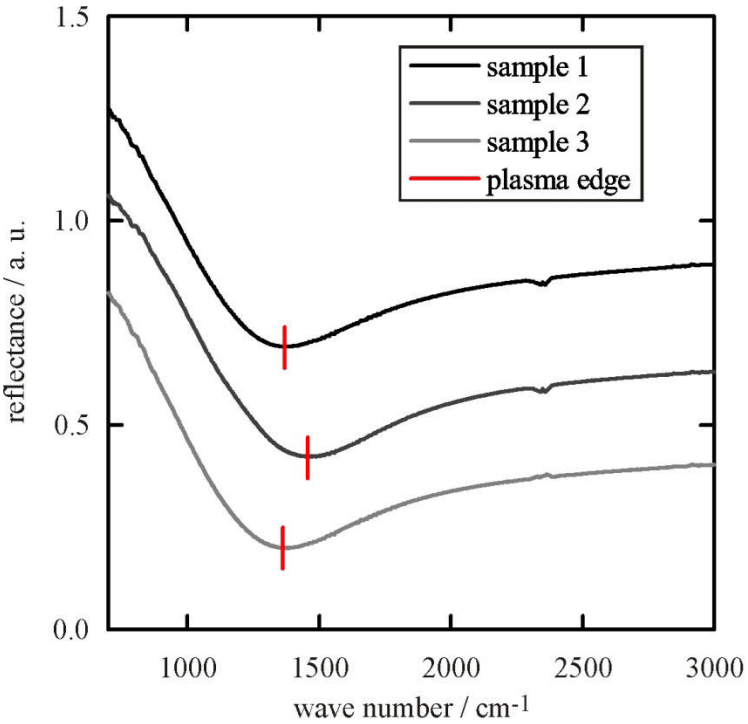


Fig. 8: Examples of infrared spectra for three titanium disulfide crystals before intercalation experiments. The compositions of the displayed samples ranges from $Ti_{1.0069}S_2$ with a plasma edge at 1362 $cm^{-1}$ (sample 3) to $Ti_{1.0079}S_2$ with a sample edge at 1457 $cm^{-1}$.

Similar spectra were obtained by several authors [Logothetis et al. 1979, Kukkonen 1981, Rüscher 1997] and interpreted in terms of plasma frequencies of free electrons (Drude model). According to this, the frequency of the plasma edge depends on the charge carrier concentration and can be used to calculate excess titanium in the titanium disulfide:

$$N = \frac{\omega_p^2 \cdot m_{opt} \cdot \varepsilon_0 \cdot \varepsilon_\infty}{e^2} \qquad (3)$$

with

$m_{opt} = m_e \cdot 1.3$ [Logothetis et al. 1979]

where N is the number of charge carriers per volume, $\omega_p$ the plasma frequency, $\varepsilon_0$ the dielectric constant, $\varepsilon_\infty$ the high frequency dielectric constant, e the elementary charge and $m_e$ the free electron mass. The value of 18 for $\varepsilon_\infty$ was taken from Kukkonen et al. [1981]. The optical mass $m_{opt}$ is the effective electron mass in the $TiS_2$ crystal. The plasma frequency is the angular frequency of the electron oscillation with respect to the ions of the lattice. It was calculated from the plasma edge according to Equation (4):

$$\omega_p = f \cdot 2\pi = \tilde{\upsilon} \cdot c \cdot 2\pi \qquad (4)$$

where *f* is the frequency of the plasma edge, ϋ is the wave number of the plasma edge and *c* is the speed of light.

The calculation of excess titanium is based on the assumption that each titanium atom contributes 4 electrons to the conduction band. Thus, N/4 was divided by the number of titanium atoms in the same volume in stoichiometric $TiS_2$, i.e. the concentration of titanium in the dichalcogenide (C(Ti)) or the reciprocal volume of a $TiS_2$ unit cell $V_{UC}$, respectively, to get y in $Ti_{1+y}S_2$, which is the nonstoichiometry of the crystals. The molar volume was calculated using the lattice parameters of Chianelli et al. [1975]:

$$y = \frac{N}{4 \cdot C(Ti)} = \frac{N}{4} \cdot V_{UC} = \frac{N}{4} \cdot a^2 \cdot c \cdot \sin(60°) \quad (5)$$

The composition of the $TiS_2$ crystals was between $Ti_{1.0063}S_2$ and $Ti_{1.0083}S_2$ which corresponds to an amount of excess titanium of less than 1% in the analyzed crystals.

Excess titanium residing in the van der Waals gaps was expected to reduce diffusivity of intercalant atoms by bonding of the layers and occupation of the octahedral sites in the lattice [Matsumoto and Nagai 1987]. Winn et al. [1976] measured the chemical diffusivity of sodium in $Ti_{1+y}S_2$ single crystals and found a decrease of diffusivity with increasing excess titanium. Yamamoto et al. [1985] measured chemical diffusivities of lithium in polycrystalline $Li_xTi_{1+y}S_2$ (y = 0, 0.03 and 0.13) using current-pulse relaxation technique. They found that diffusivity of lithium was not noticeably influenced by excess titanium for lithium contents of $x < 0.6$ but a reduction of lithium diffusivity at higher lithium contents due to the occupation of available sites for lithium by titanium.

The nonstoichiometry of the $TiS_2$ samples used in this work was less than 1%, meaning that maximum 1% of the octahedral sites in the van der Waals gap were occupied by titanium atoms. This low degree of occupation of octahedral sites is not likely to reduce diffusivity.

IR spectra were also recorded for $TiSe_2$ and $TiTe_2$ crystals (Fig. 9). In contrast to $TiS_2$, the other chalcogenides $TiSe_2$ and $TiTe_2$ exhibit band overlaps yielding free electrons in addition to electrons, which result from excess titanium atoms. Therefore, it is not possible to determine the nonstoichiometry of the samples.

The spectra of $TiSe_2$ show a good agreement with reflectivity spectra recorded by Wilson et al. [1978]. Wilson et al. determined charge carrier concentrations in $TiSe_2$ from the plasma frequency. As the plasma edge is not identifiable in the reflectivity spectra, they conducted a Kramers-Kronig analysis and plotted the imaginary part of $-\frac{1}{\varepsilon}$ versus the wave number, where the plasma frequency was identified as a maximum at 1100 $cm^{-1}$ at 300 K. This corresponds to a lower charge carrier concentration compared to the $TiS_2$ samples used in this work and thus, the $TiSe_2$ samples used by Wilson et al. possessed a lower amount of excess titanium. Wilson et al. also stated that it is considerably easier to bring the metal content of the diselenide down to the stoichiometric limit compared to the disulphide.

The shift of the plasma edge to higher wave numbers in the spectra of $TiTe_2$ reflects that the charge carrier concentration is higher compared to $TiS_2$ and $TiSe_2$, which is consistent with the reported metallic properties of the compound (see section A.1.3).

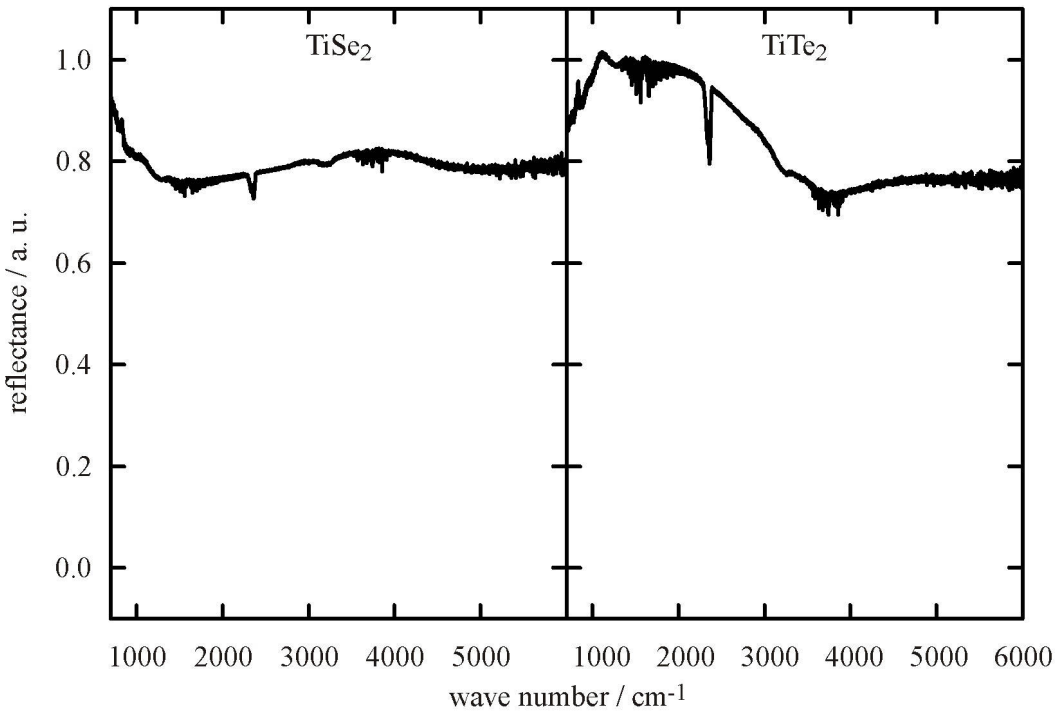


Fig. 9: Examples of infrared spectra for titanium diselenide and titanium ditelluride. Spectra were recorded before intercalation experiments.

## B.2 Sample preparation

Crystals with diameters of > 3 mm and well-developed surfaces, i.e. essentially free of visible steps and fissures, were selected for the intercalation experiments. The crystals were visually controlled using a Leica DC 610 microscope. Crystals were cut with a fs-LASER into squares with a typical edge length of 2.2 mm. Using this way of preparation, lithium can enter the crystal from all edges, and in the centre of the edges one-dimensional diffusion conditions should be warranted as long as the diffusion profile is shorter than the distance to the crystal corners.

In order to avoid penetration of lithium from the base planes two different encapsulation strategies were tested.

In the beginning of the studies glass plates of approx. 150 µm thickness were glued by a thin layer of epoxy on both sides of $TiS_2$ crystals (Fig. 10). By this preparation technique the crystals were stabilized mechanically.

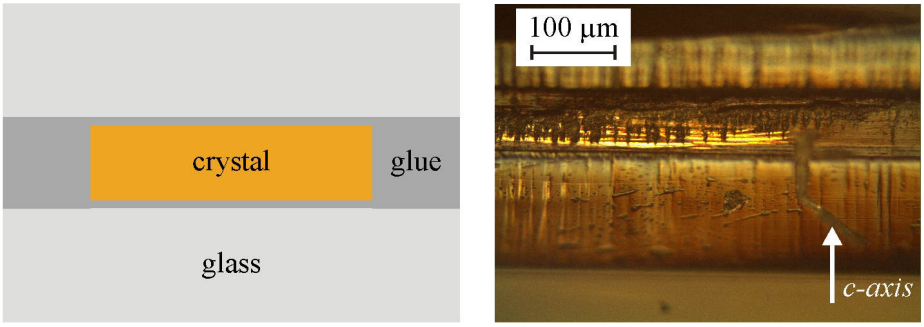


Fig. 10: Sample preparation using thin glass plates. A schematic drawing shows the assemblage on the left. A microscopical image of the sample edge is shown on the right.

Due to its low ablation rate the glass was polished to a thickness of approx. 20 µm with a very smooth surface. Subsequently, the sample was ablated along one path, which was passed back and forth, and the titanium intensity was measured using ICP-OES. This test measurement served as a control, whether the LASER spot reached the crystal in the same pass at all positions of the path, which was not the case. The measured titanium intensity during several passes is displayed in Fig. 11.

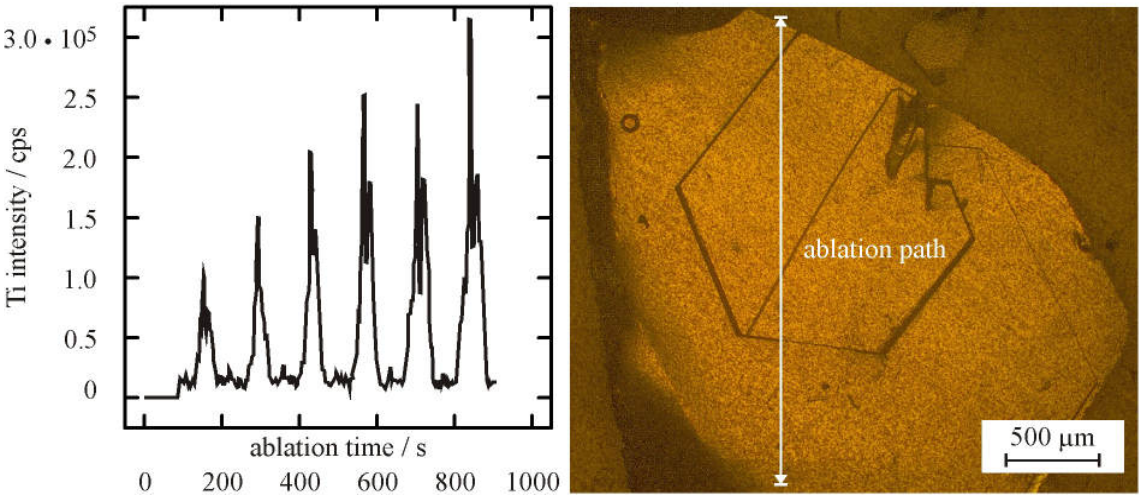


Fig. 11: LA-ICP-OES measurement (left) of a titanium emission signal on a glass-crystal-glass sandwich. The path shown on the sample (right) was ablated several times. The structures that are visible on the sample are steps on the crystal surface.

It can be seen that the LASER successively ablates more material from the crystal at a part of the path in each further pass, which becomes apparent from the increasing maximum titanium intensity. It should be noted that this section is not congruent with the structure that is visible on the sample. At other sections (low Ti intensities) the LASER did not ablate material from the crystal until the end of the measurement.

The described ablation behaviour eventually leads to deep craters in the crystal at parts of the pass where the crystal is reached, because the ablation rate of $TiX_2$ is high. On the other hand, the ablation rate of the glass is low. This means more LASER pulses are required to ablate a certain thickness of the glass. Thus, slight variations in the glass thickness have a strong impact on the time at which the crystal is reached.

This test revealed that encapsulation of the samples with glass plates was not suitable for subsequent measurement of lithium profiles using LASER ablation. Therefore the preparation technique was discarded.

In the second preparation strategy only epoxy (Araldit 2020®) was used (Fig. 12), which is readily ablated with a LASER. Thus, the drawbacks, which occurred at the previous strategy, could be avoided.

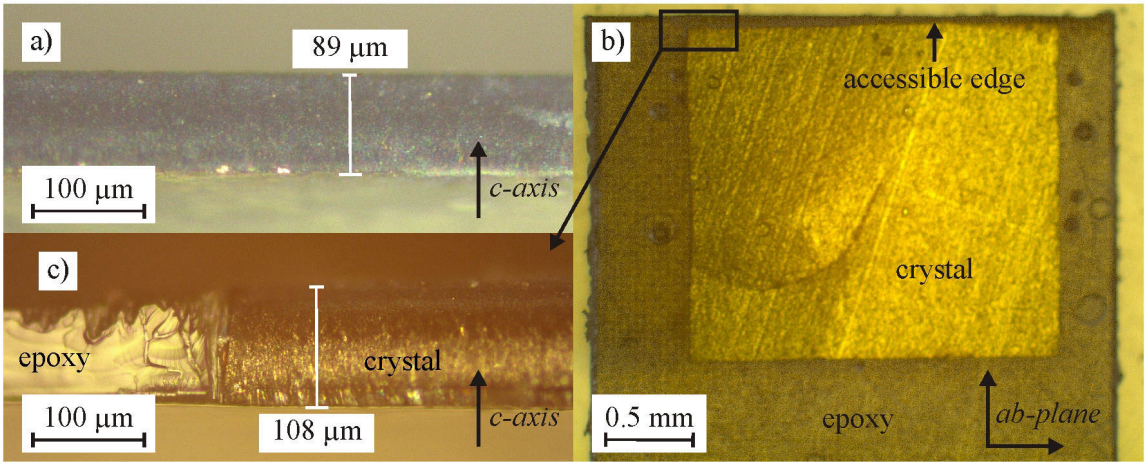


Fig. 12: Encapsulation of a $TiS_2$ crystal with epoxy. a) shows the crystal edge prior to encapsulation. b) shows the surface parallel to the sheets after encapsulation. The crystal edge on the upper picture is accessible to BuLi. c) shows marked area in b). The thin epoxy encapsulation is not visible above and below the crystal. However, comparison to a) reveals that the thickness increased by approx. 19 µm corresponding to epoxy layers of about 10 µm on each side.

The square-shaped samples were placed in a drop of the liquid epoxy between non-adhesive foils and loaded with weights. Thus, after hardening, coplanar thin layers (5-30 µm) encapsulated the crystals. A straight cut with the LASER was used to open one side of the crystal to the solution. The epoxy at the other edges was also cut to protrude only slightly over the crystal area.

This preparation technique counteracts forces on the crystal induced by widening when lithium is inserted and the crystal surface is protected from corrosion. In this way it can be ensured that the intercalation can only take place in the *ab-plane,* and defects such as cracks, fissures or steps in the base planes do not affect the intercalation experiments. Thus, one-dimensional boundary conditions for intercalation can be established.

Another advantage of this preparation technique specifically concerns the uniaxial pressure experiments. Pressure spikes due to sample roughness are absorbed, as the epoxy layer is plastically deformable. This is described in detail in the experimental section of the uniaxial pressure experiments (D.2).

A disadvantage of LASER cutting of the encapsulated samples is, however, that the cut edge is sometimes smeared by epoxy and deposited crystal material, which was not easy to remove before experiments without damaging the crystal. However, no residuals of epoxy were observed after interaction experiments, implying that such deposits are at most short term barriers for lithium insertion.

## B.3 Synthesis of the standards

Standards are required for calibration of the LASER-ablation OES measurements. The standards were produced and characterized by N. Schwarzburger. All elements (Li Sigma Aldrich, 99.9%; S, Sigma Aldrich, 99.99 %; Se, Sigma Aldrich, 99.98 %; Te, Sigma Aldrich, 99.98 %; Ti, ABCR, 99.95 %) were mixed under a dry argon atmosphere in stoichiometric quantities for $LiTiS_2$ [Kim 2009]. The elements were loaded in a corundum crucible and placed in a silica glass ampoule. Vacuum was applied and the ampoule was heated up slowly to 1020 K. After three days at 1020 K black crystals were formed. To improve homogeneity, the synthesis product was ground under an argon atmosphere and processed again as described above. The final powder was analyzed by ICP-OES (Varian VISTA AX CCD), CSD (Carbon Sulfur Determinator, Eltra, CS 2000), EDX (energy dispersive X-ray spectroscopy, FEI-Phillips XE 30) and XRD (X-ray diffraction, Stoe Stadi P). The compositions of the powders that were used as standards in this work are given in the appendix.

XRD (X-ray diffraction, Stoe Stadi P) measurements indicate that several phases were present in the standards [Schwarzburger 2013]. However, EDX measurements approved homogeneity of the standards on the micrometer scale. The powder was pressed to pellets prior to the insertion into the abla-

tion cell for LA-ICP-OES and -MS measurements. As the spot size of the LASER was much larger than the grain size of the powder, the standard can be regarded as homogenous. The standards were stored under dry argon atmosphere prior to analysis, but got in contact with air during analytical sessions and reacted with moisture and oxygen. No signs of degradation were observed during individual analytical sessions, i.e. standard measurements at the beginning and at the end of analytical sessions showed good agreement. However, each standard pellet was only used for a single analytical session.

## B.4 Analytical approach

The samples were analyzed using LA-ICP-OES and -MS, respectively. An overview of the entire system is given in Fig. 13. The individual components are described in the subchapters below.

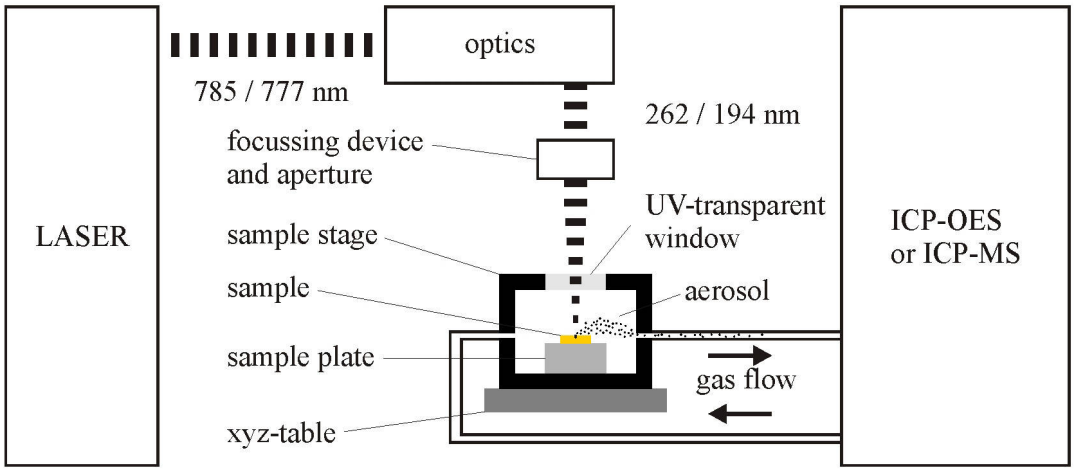


Fig. 13: Analytical setup for the measurement of lithium-content-distance profiles. Given wavelengths denote centre wavelengths.

### B.4.1 LASER Ablation system

Two different LASER systems were used for ICP-OES and ICP-MS measurements, respectively. These produced infrared light pulses with a pulse width of 100 fs. After frequency conversion in the in-house built optics using barium borate as nonlinear optical material, two beams in the ultraviolet range could be used for LASER ablation measurements. Table 1 gives an overview over parameters of the systems.

Table 1: Comparison of parameters used for LASER ablation for ICP-OES and ICP-MS measurements. Typical energy densities are calculated for beam diameters of 80 µm in ICP-OES and 20 µm in ICP-MS measurements.

| | LA-ICP-OES measurements | LA-ICP-MS measurements |
|---|---|---|
| System | Hurricane I, Spectra Physics | Solstice, Spectra Physics |
| Fundamental wavelength | 785 nm | 777 nm |
| Maximum energy of fundamental wavelength | 1 mJ / pulse | 3.3 mJ / pulse |
| Wavelength used for ablation | 262 nm | 194 nm |
| Frequency conversion | 3rd harmonics | 4th harmonics |
| Pulse energy at sample | 32 µJ | 8 µJ |
| Typical energy density | 0.6 J / $cm^2$ | 2.5 J / $cm^2$ |
| Range of LASER spot sizes used | 49 - 110 µm | 15 - 25 µm |
| Repetition rate | 10 Hz | 10 Hz |

At the beginning of this work, the ablation system was based on a Hurricane I (Spectra Physics) Ti-sapphire regenerative amplifier system operating at a fundamental wavelength of 785 nm [Horn and Blankenburg 2007]. As this system was used in combination with the ICP-OES, it was crucial to get a sufficiently high emission signal. Therefore, the high-energy third harmonic (262 nm) of the fundamental wavelength was used for ablation. This allowed using large beam diameters (49 to 110 µm) while maintaining an energy density high enough to ablate $TiX_2$ (1.6 J / $cm^2$ at 49 µm and 0.3 J / $cm^2$ at 110 µm).

During the course of this work, a new Ti-sapphire regenerative amplifier system (Solstice, Spectra Physics) became available, which operated at a fundamental wavelength of 777 nm. The system was used for LA-ICP-MS measurements. The sensitivity of the ICP-MS system is higher compared to the OES system, which allows to ablate less material while maintaining a sufficient signal. Therefore the fourth harmonic of the fundamental beam (194 nm) and smaller spot diameters were used for LASER ablation (approx. 15 to 25 µm corresponding to 4.4 J / $cm^2$ and 1.6 J / $cm^2$, respectively).

The beam profile of the Solstice system was determined with a DataRay WinCamD-UCD15 beam imaging camera (Fig. 14) at a wavelength of 262 nm. This was necessary, because the fourth harmonic was too weak to be up-converted into the IR for measurement with the camera. However, the beam profile is assumed to be similar at both wavelengths.

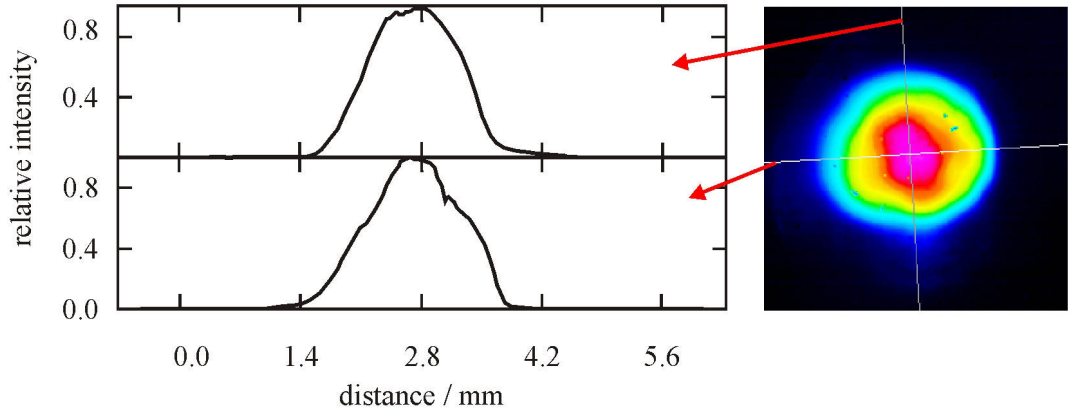


Fig. 14: Graphs of two orthogonal intensity profiles, which were measured at a wavelength of 260 nm. The positions of the profiles are marked on the right, which is an illustration of the LASER beam intensity distribution. The illustration represents average intensities from 10 individual measurements with an exposure time of 44 ms, each. The pulse energy of the beam was 0.22 mJ. The beam was measured before the focussing device.

The $TEM_{00}$ mode of the LASER has a Gaussian intensity profile (not shown here). The profile of the beam used, deviates slightly from Gauss shape because marginal regions of the beam are damped during wavelength conversion. This leads to steeper flanks of the profile compared to a Gauss shape. The profile exhibits an ellipticity of 0.91, which is basically a feature of the fundamental beam.

After the optics, the LASER beam passes a computer controlled iris that allows adjusting the spot size on the sample surface. Marginal areas of the LASER beam are cut off when it passes the aperture. Finally, the beam is steered into different objectives (5x OFR 266nm in the case of OES measurements and 8x 193 nm for MS measurements) and focused onto the sample. Due to the lens elements in the objectives, only a part of the energy reaches the sample surface.

Profilometric measurement of ablation craters was difficult on $TiX_2$ samples due to strong differences of the reflectivity in the crater and on the sample surface around the crater. Thus, PVC samples were used to get information about the crater that is generated by the LASER beam used. PVC has a low ablation threshold, which leads to a good representation of the beam intensity distribution in the resulting topography. Subsequent measurement of the crater topographies were perfomed by Hans-Christoph Schwarz at the Laboratory of Nano and Quantum Engineering (LNQE, LUH) using a Leica

DCM3D confocal microscope. Profiles of craters are shown exemplarily for different numbers of pulses in Fig. 15.

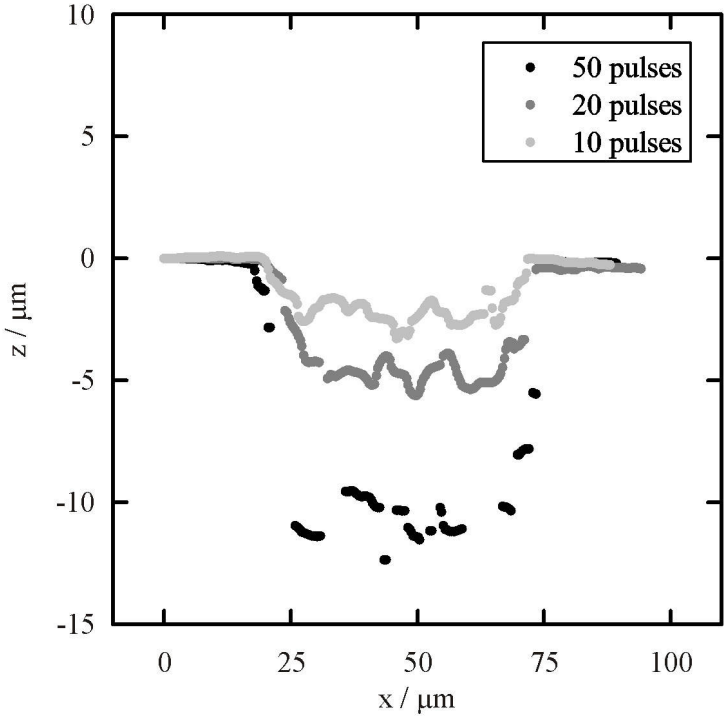


Fig. 15: Examples of profiles for LASER ablation craters on a PVC sample. Craters were ablated with the solstice system using the 194 nm beam. The iris was adjusted to provide a LASER spot with a diameter of approx. 50 µm on the sample surface. The craters were next to each other on the sample but are displayed as overlay for better comparability. The crater depths indicate a constant ablation rate of approx. 2.5 µm / pulse at an energy density of approx. 0.3 J / $cm^2$.

The craters show circular outlines and steep flanks. The variation of the depth that is apparent in the valleys for 10 and 20 pulses can be assigned to sample roughness. A distinct depth profile does not evolve in the valleys with an increasing number of pulses. Therefore, the ablation rate in the centre of the LASER spot can be considered homogeneous. This indicates that the initial Gaussian shape of the fundamental beam is changed towards a flat-top profile. This effect is probably stronger for the ablation of $TiX_2$ because a higher ablation threshold compared to PVC leads to less ablation at the beam flanks, which are lower in energy. Moreover, the slight ellipticity of the LASER beam was not observed, probably because of the circular iris.

### B.4.2 Sample stage

Samples were analyzed in a modified vacuum tight heating and cooling stage (Instec HCS621V) that was cooled down to 248 K during the analyses. Cooling of the samples minimizes diffusion of lithium during the time of measurement. The stage required modifications in order to be used as an ablation cell for fs-LASER ablation. To avoid condensation of ablated material on cold surfaces, the inner components were masked with Teflon foil. Transport of the ablated material was realized by a gas line that was connected to the vacuum inlet of the stage. Unfortunately, the two ports which were designed as vacuum or purge connections were placed next to each other. Therefore, the gas line was rooted through the cell to provide a continuous gas flow over the sample, allowing fast transport of the ablated material to the argon outlet (Fig. 16).

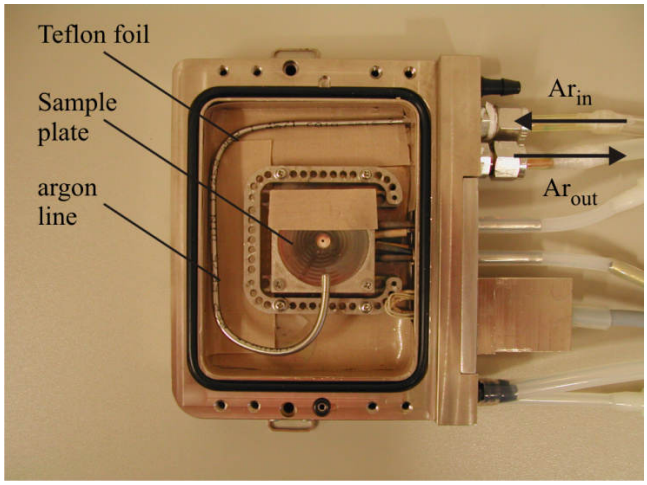


Fig. 16: Photo of the modified cooling stage used for LA-ICP-OES and -MS measurements. See text for further details.

Samples and standard were placed on the sample plate. The sample stage was mounted on a motorized *x*-*y*-*z*-stage that allows ablation along lines on the samples and thus measurement of intensity-distance profiles.

### B.4.3 Measurement of element contents

Initially the samples intercalated at hydrostatic pressures were analyzed with an ICP-OES (Varian VISTA pro, AX CCD). During this study a new ICP-MS system (Thermo Scientific Element XR), which possesses a higher sensitivity compared to the ICP-OES system, became available. Some of the samples intercalated under hydrostatic pressure were measured using the ICP-MS system. The used analytical technique is given in Table 3 for each sample in the experimental section. Furthermore some samples which had been measured before using the ICP-OES system were remeasured to compare the analytical techniques. All samples that were intercalated under uniaxial pressure were measured using the LA-ICP-MS system.

Typical parameters that were used in the measurements are given in Table 2. The analytical techniques are described in detail below.

Table 2: Typical parameters in the ICP-OES and ICP-MS measurements. Gas flows are given in L / min.

| Settings | ICP-OES | ICP-MS |
|---|---|---|
| Cool gas flow | 18 | 15 |
| Auxiliary gas flow | 2.25 | 0.8 |
| Sample gas | 1.3 | 1.3 |
| Additional gas | - | 0.8 |
| RF power / kW | 0.9 | 0.91 |

#### B.4.3.1 Inductively-Coupled-Plasma-Optical-Emission-Spectroscopy (ICP-OES)

The ablated material was transported by an argon gas flow to the ICP-OES. Background corrected count-rates (cps) of the emission lines at 610.365 nm for Li and at 334.188 nm for Ti were calculated by subtracting the gas blank which was measured before the profile aquisition and calibrated against the standard to determine atomic ratios Li/Ti on the sample. Assuming a composition $Li_xTiX_2$ , i.e. a constant ratio of Ti over X, the Li/Ti ratio can be converted into the stoichiometric factor x. Signal variations due to fluctuations of the plasma and the volume of ablated material are eliminated through this normalization.

#### B.4.3.2 Inductively-Coupled-Plasma-Mass Spectrometry (ICP-MS)

The ablated material was transported by a mixture of dry helium and argon gas to the ICP-MS, which is much more efficient [Horn and Günther 2003] and reduces the required ablated material further. Standard nickel sample and skimmer cones were used. The element menu was composed of the isotopes $^{47}$Ti, $^{7}$Li, $^{32}$S $^{77}$Se and $^{144}$Te. Measurements were conducted in medium resolution. Measurement time was approx. 1.4 s for one sweep between $^{7}$Li and the chalcogen isotope. Weight contents of the elements were calculated and subsequently converted into stoichiometric factors.

### B.4.4. Comparison of LA-ICP-OES and LA-ICP-MS measurements

Samples from hydrostatic experiments that were measured by LA-ICP-OES previously were remeasured by LA-ICP-MS after the system became available. The samples were stored between these measurements in liquid nitrogen. All of the remeasured samples showed a strong reduction of diffusion lengths and lithium surface contents compared to the primary measurements, indicating that the samples were deintercalated during storage.

When samples are unfreezed and measured using LASER ablation techniques repeatedly existing cracks and cleavages increase due to stress and absorbed moisture. This leads to leaching of lithium from the crystals. Therefore a direct comparison of LA-ICP-OES and LA-ICP-MS measurements was not possible.

However, $TiTe_2$ samples that were intercalated under the same experimental conditions yielded diffusion coefficients in the same range for both analytical techniques (see Table 3). Moreover, $TiS_2$ samples intercalated at hydrostatic pressures showed diffusivities determined with LA-ICP-OES that were in the same range as diffusivities from uniaxial pressure experiments that were determined with LA-ICP-MS (Fig. 40). Thus, it can reasonably be assumed that data from both analytical methods can be compared directly.

## B.5 Evaluation of content-distance profiles and error estimation

### B.5.1 Definition of the zero point

The zero point cannot be determined exactly using the optical microscope of the LASER ablation system, due to bad visibility of the LASER spot on the sample surface. Therefore the zero point is defined on the basis of the measured titanium signal (Fig. 17).

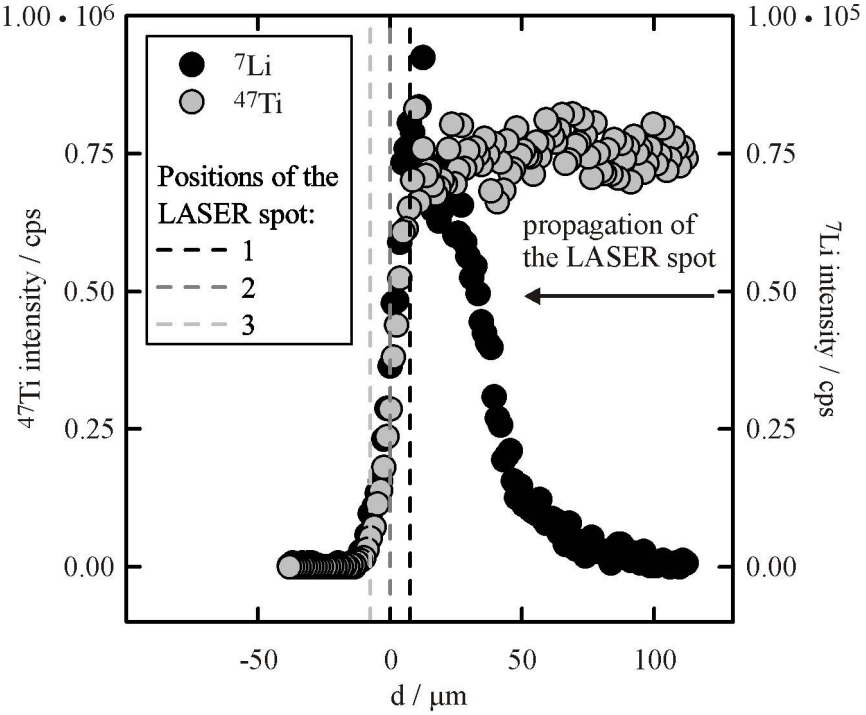


Fig. 17: Definition of the zero point of diffusion in an intensity distance profile of a LA-ICP-MS measurement (sample $TiS_2$-R30). The LASER spot diameter of this measurement was 15 µm. The lines in Fig. 17 mark the first exceeding of the LASER spot over the crystal edge (1), the position where the spot centre is on the crystal edge (2) and the position where the whole LASER spot left the crystal (3).

Profiling started in the interior of the crystal and exceeded over the crystal edge. When the LASER spot approached the crystal edge, sometimes the signal intensities of both Li and Ti increased, probably due to weakening of interlayer bonds and fanning in the intercalated region. The maximum intensity was observed when the LASER spot reached the crystal edge (not shown here). When the LASER spot started to cross the crystal edge less material was ablated and thus the titanium intensity decreased (marked by line 1 in Fig. 17). This condition was used to define the zero point of the profile, i.e. the position is half the spot diameter away from the edge. When the whole LASER spot crossed the edge no more material is ablated and the titanium and lithium intensities reached the background level.

Generally, when material is ablated only by a fraction of the LASER spot the uncertainty of the calculated lithium contents is high. Therefore only lithium contents that were measured as long as the whole LASER spot was still on the crystal were considered for the evaluation of the profiles. This procedure leads to an uncertainty of $x_{Li,S}$ values, especially for large LASER spot diameters and short and steep profiles. Because of initial roughness and corrosion of the edge during experiments, the zero point of diffusion was shifted towards the interior of the crystal. Therefore our method of defining the zero point leads to systematically higher values for $x_{Li,S}$ and D. This systematic error affects the lithium surface content generally stronger than the diffusion coefficient. However, the systematic error of the $x_{Li,S}$ value is very sensitive to the steepness of the profile.

Fig. 18 shows a profile where the zero point of diffusion was shifted into the interior of a $TiTe_2$ sample. For the profile, where the zero point was defined as described above, the fit to Eq. 5 (see following section) yields a diffusion coefficient of $D = 7.5 \cdot 10^{-16}$ $m^2/s$ and a lithium surface content of $x_{Li,S} = 1.87$. The value of $x_{Li,S} > 1$ indicates that the defined zero point is incorrect, as only one lithium per formular unit can be intercalated. The zero point of diffusion might be corrected when $x_{Li,S}$ is constrained to a constant value of 1, as the $x_{Li,S}$ values, determined from other diffusion profiles in intercalated $TiTe_2$, were close to 1.

In doing so, the zero point of this profile is shifted into the crystals interior by approx. 15 µm. The evaluation of the shifted profile yields values of $D = 5.1 \cdot 10^{-16}$ $m^2/s$ and $x_{Li,S} = 1$. Of course, a correction procedure like this introduces an error, as $x_{Li,S}$ was constrained to the maximum value. Thus, the

real $x_{Li,S}$ value and diffusion coefficient are probably lower. This correction was done for two profiles that were measured on $TiTe_2$ samples and is specified in the respective experimental section (chapter C.2.3).

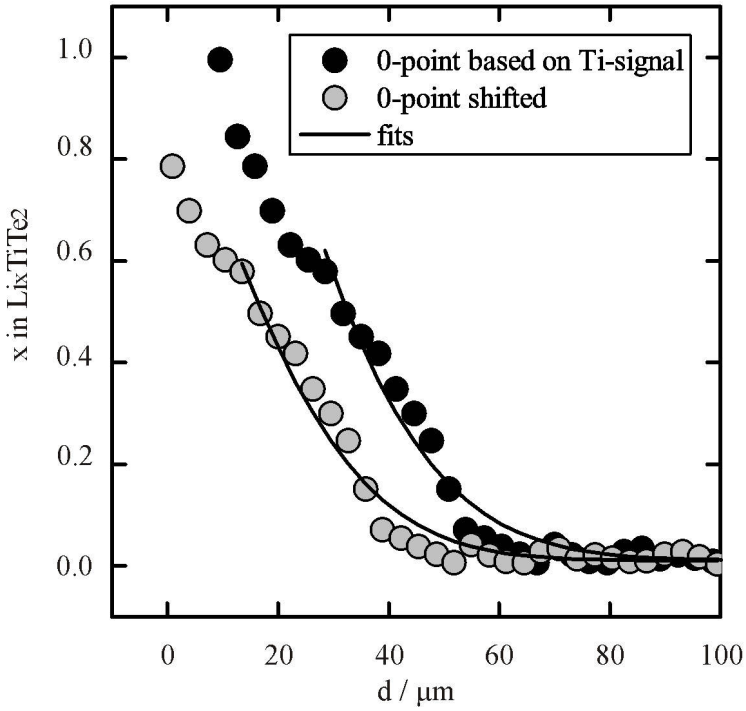


Fig. 18: Diffusion profile with the described definition of the zero point and the same profile with the zero point shifted into the crystal interior by 15 µm.

Another sign of a zero point shift can be the presence of a plateau of constant lithium content at the edge of the sample. In this case the zero point can be shifted on the basis of the profile shape. This was done for some of the samples that were intercalated under uniaxial pressure and is specified in the respective section (D.3.3). This procedure also introduces a systematic error as it includes the assumption that the zero point is shifted by a constant value into the crystal right at the beginning of the intercalation experiment. It is more realistic, that the zero point varies along the edge and that it is shifted into the crystal continuously during the experiment. Thus, the derived diffusivities and lithium surface constants are too low.

## B.5.2 Fitting of the profiles

Profiles were evaluated assuming a constant (or negligible) initial concentration $c_{Li,0}$ of lithium in the crystal, a constant surface concentration $c_{Li,S}$ of lithium in the crystal, and a concentration-independent diffusion coefficient $D_{Li}$. For the given boundary conditions, the solution of Fick's 2nd law for one-dimensional diffusion is [Crank 2002, Mehrer 2009]:

$$c_{Li} = c_{Li,0} + \left(c_{Li,S} - c_{Li,0}\right) \cdot \left(1 - erf\left(\frac{d}{\sqrt{4 \cdot D_{Li} \cdot t}}\right)\right) \qquad (6)$$

where $d$ is the distance from the surface, and $t$ is the run duration. For simplicity it was assumed that the molar volume is constant along the diffusion profile. With this assumption $x$ can be used as a concentration variable replacing $c_{Li}$. Using this terminology, the surface concentration becomes $x_{Li,S}$. In the case of full intercalation ($x = 1$ in $Li_xTiS_2$) the increase in molar volume is only approx. 12 % compared to $TiS_2$ (calculation based on the lattice parameters given in

Table 4) and, hence, the simplification does not introduce significant error in the determination of the diffusion coefficient.

### B.5.3 Artificial elongation of the profiles and correction

When content-distance profiles are measured using LASER ablation techniques, material is ablated over a certain distance of the profile, i.e. the diameter of the LASER spot. This automatically leads to discrepancies between the measured and the real content-distance profile. Specifically the measured diffusion profile is longer compared to the real diffusion profile. Thus, the effect is referred to as artificial elongation. The impact on the diffusion profile depends on the size of the LASER spot as well as the profile length.

Due to experimental constraints, profiles were often short compared to the beam diameter; the total range of measurable concentration changes rarely exceeded the size of the LASER spot by a factor of three. Therefore, the artificial elongation has to be considered. To correct the diffusion coefficient, model calculations were performed for different profile lengths and different diameters of the LASER ablation beam.

Basic assumptions are that (i) the beam has circular shape on the crystal and (ii) that ablation is uniform in the whole excited area. In other words: it is assumed that the ablated volume is disc shaped with a constant depth. The measurement of the LASER beam profile and the profilometric measurements of LASER ablation craters on PVC samples (chapter B.4.1) showed that these assumptions can be made without introducing a major error.

However, it has to be emphasized that following correction procedure of diffusion data is not applicable when (i) profiles deviate from the error function shape, i.e. the process is not only controlled by diffusion or the diffusion coefficient depends on composition and (ii) the surface concentration of lithium in the crystal changes with time.

#### B.5.3.1 Model calculations

A schematic illustration of the model calculations is shown in Fig. 19. In the first step, error function shaped profiles were calculated with defined values for $x_{Li,0}$, $x_{Li,S}$, t and D (Fig. 19a).

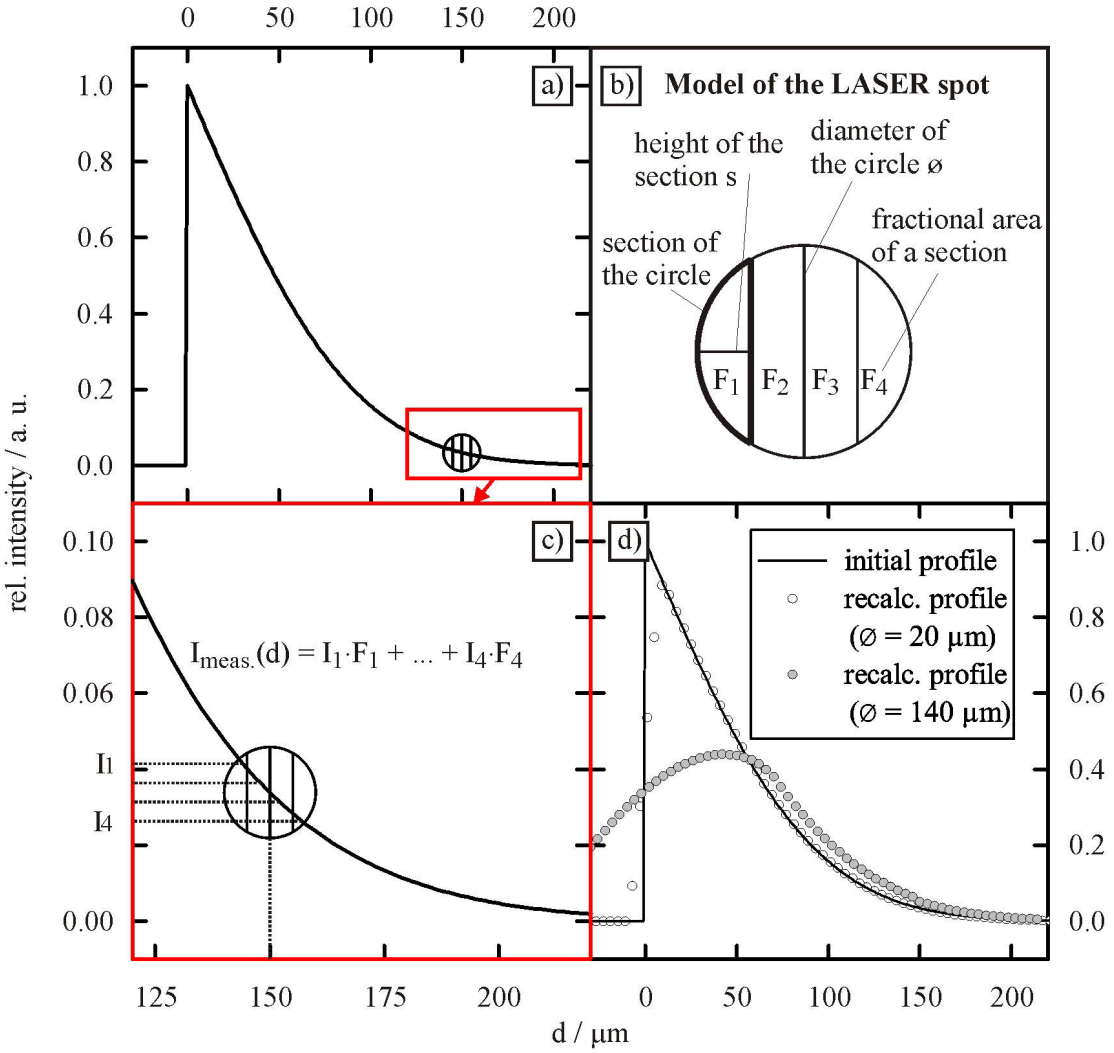


Fig. 19: Schematic illustration of the model calculations. a) shows an error function shaped profile with the model LASER spot at a certain position of the profile (150µm). b) illustrates the model of the LASER spot and the parameters included. c) illustrates the calculation of a "measured" intensity at one position of the profile (150 µm). d) shows the ideal profile and the profiles that result from recalculation with LASER spot diameters of 20 and 140 µm and a segment height of 1 µm.

These profiles served as ideal diffusion profiles that would be measured with an infinitely small LASER spot. The intensities of these profiles are known for every position of the profile.

A model of the LASER spot was developed, assuming a circular spot with a radius $r$ and a homogenous ablation over the spot (Fig. 19b). The spot was divided into sections by parallel chords. The height of the sections was constrained to a value of $s$ = 1 µm.

In the next step, the fractional areas of the sections were calculated. Therefore, it was necessary to calculate areas of circular segments $A_{Seg.}$, with a varying height $h$ beforehand. The circular segment is the area, which is circumscribed by the arc and a chord.

The segmental areas were calculated with Equation 7 for a semi circle, i.e. until $h = r$. Self-evidently, the areas of the other semi circle are simply mirrored and thus, don't need to be calculated.

$$A_{Seg.}(h) = r^2 \cdot \arccos\left(1 - \frac{h}{r}\right) - \sqrt{2 \cdot r \cdot h - h^2} \cdot (r - h) \qquad (7)$$

The two outermost sections are congruent with the outermost circular segments, provided that the heights are equal. The fractional areas of the outermost sections were calculated by dividing the segmental areas by the total area of the circle.

The areas of the inner sections were calculated by increasing the segment height in Equation 7 in steps of 1 µm and subtracting the preceding segmental areas. These areas were also divided by the circle area to get fractional areas $F_2$ to $F_r$.

$$F_2 = \frac{A_{Seg.}(h = 2\mu m) - A_{Seg.}(h = 1\mu m)}{A_{circle}}, F_3 = \frac{A_{Seg.}(h = 3\mu m) - A_{Seg.}(h = 2\mu m)}{A_{circle}} \ldots \quad (8)$$

In the next step the intensities of the ideal diffusion profile were recalculated (Fig. 19c). This was done by calculating "measured" intensities for every position of the LASER spot on the ideal profile individually.

The measured intensity at a certain position of the profile ($I_{meas}(d)$) is the sum of the ideal intensities multiplied by the fractional area of the section at the corresponding position. This is shown exemplarily for a LASER spot that was divided into 4 sections at one position of the profile in Fig. 19c.

The LASER spot was shifted over the ideal profile in 1 µm steps and values for $I_{meas}(d)$ were calculated successively. When the spot crosses the zero point of the initial profile, i.e. half of the spot diameter away from the zero point, the calculated intensity starts to decrease. This corresponds to the situation when the LASER spot in a LASER ablation measurement starts to leave the crystal edge. Thereafter material is only ablated by a fraction of the LASER spot which decreases until the LASER spot left the crystal and the intensity drops to the background level.

The procedure yielded measured diffusion profiles for the used ideal diffusion profile and LASER spot (Fig. 19d).

The validity of the model calculations was tested by measuring profiles with two different beam diameters across the interface between two dichalcogenides crystals, $TiSe_2$ and $TiTe_2$ (Fig. 20). These crystals were chosen because a stepwise transition could be established. Good agreement was found between the measured intensity of the Se signal and the model calculation. Small deviations in shape for the profile with the larger beam are attributed to non-ideality (e.g. surface roughness) of the edge.

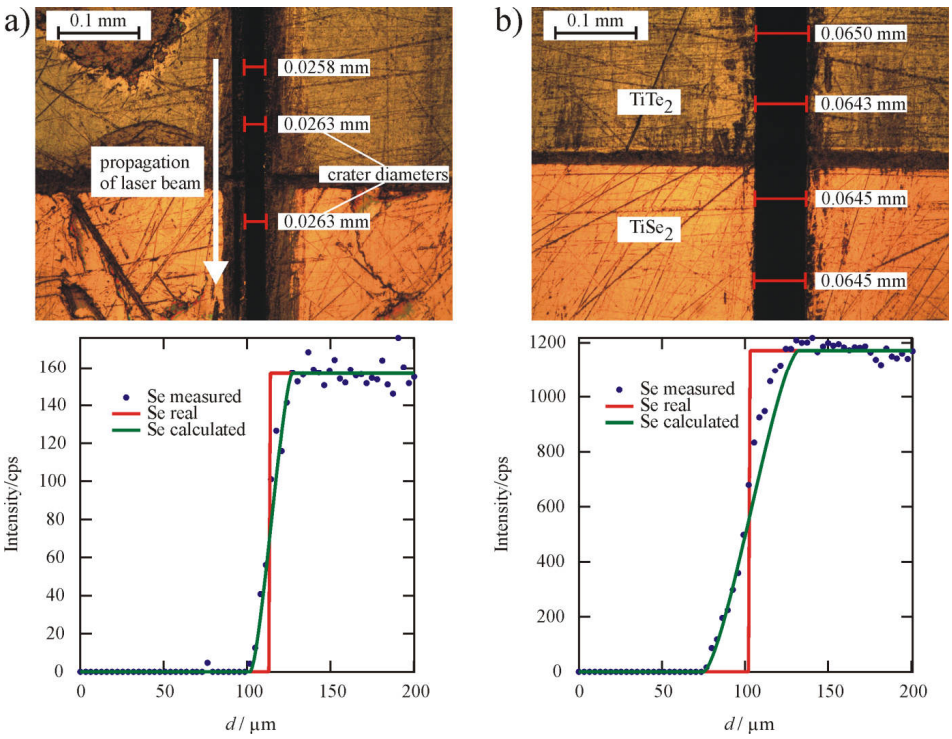


Fig. 20: Intensity - distance profiles for Se across the interface between $TiTe_2$ and $TiSe_2$ crystals. The red curve labeled "Se real" represents the Se intensity for an infinite small LASER spot. The green curve labeled "Se expected" is calculated for the respective spot diameters of 26 µm (**a**) and 65 µm (**b**) as described in the text. Origin of the *x-axis* represents the starting point of profiling.

The calculation of measured profiles was performed for different profile lengths of the initial profiles and varying LASER spot diameters Ø. The part of the modified profiles, which was calculated before the spot starts to cross the zero point, was fitted to Equation 6 to determine $D_{meas}$ and $x_{S,meas}$.

Fig. 21 shows the ratios of the initial values of $D$ and $x_S$, given by the initial profile, over the measured values $D_{meas}$ and $x_{S,meas}$, both as a function of $z = \varnothing / \sqrt{4 D_{meas} t}$. It can be seen, that the value of $x_S$ is only slightly affected even at high values of z.

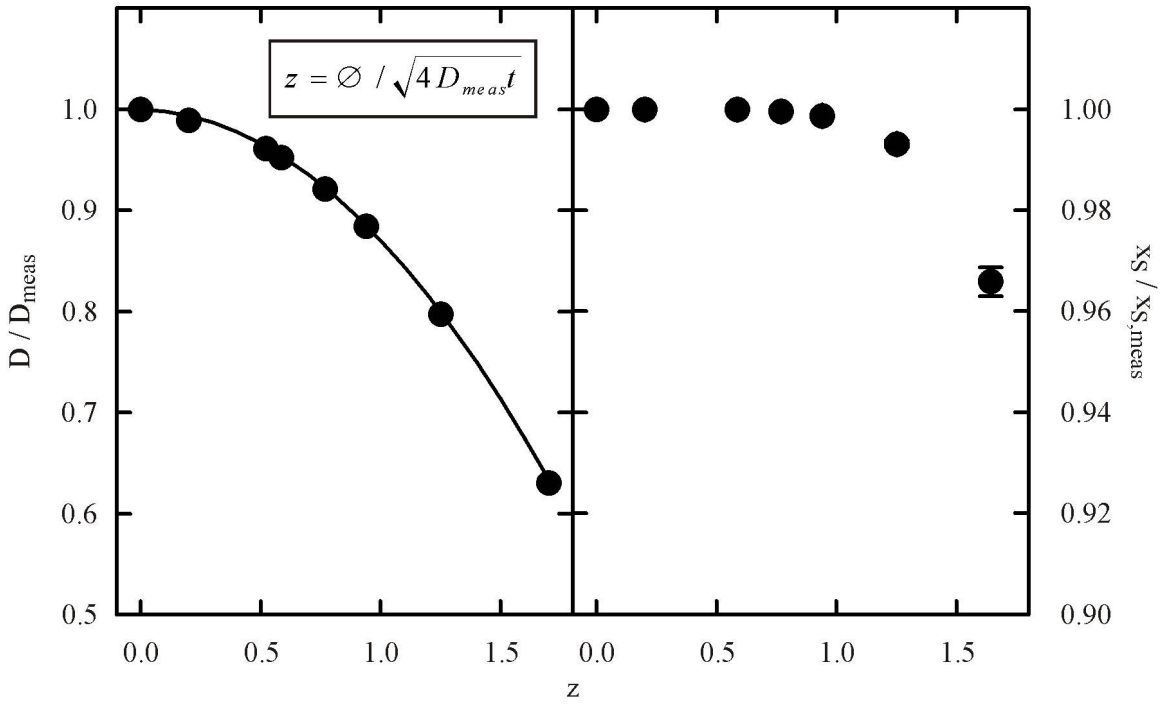


Fig. 21: Ratio of real over measured values for D (left) and $x_S$ (right) versus z. The value of z represents the ratio of the beam diameter over the profile length of the initial profile. The line represents Equation 9 obtained by fitting the data points. It should be noted that the scales of $D/D_{meas}$ and $x_S/x_{S,meas}$ differ. In contrast to $D/D_{meas}$, the ratio of $x_S/x_{S,meas}$ is close to 1 at all values of z that are shown.

On the other hand, the ratio of $D/D_{meas}$ decreases considerably with increasing z. Based on Fig. 21, a simple quadratic equation can be defined for the correction of measured diffusion coefficients:

$$\frac{D}{D_{meas}} = 1 - 0.007784 \cdot z - 0.11685 \cdot z^2 \qquad (9)$$

Profiles that were considered in this work showed error function shape and were corrected using Equation 9. As the lithium surface content is not sensitive to the value of z the values of $x_{S,meas}$ were used without correction.

Because some of the profiles are short, a rigorous error calculation is required to evaluate the quality of the diffusion data. In this calculation the following maximum errors of the controlling parameters were used: uncertainty of temperature, $\Delta T$ = 2 K; uncertainty of duration, $\Delta t$ = 10 min.; uncertainty of the position of the origin of the $x$-axis, $\Delta d$ = 10 µm; variation in effective beam diameter, $\Delta \varnothing$ = 5 µm. The errors for the individual experiments are given in the appendix of the respective experimental section.

The resulting error of the measured diffusion coefficient is calculated by error propagation as:

$$\frac{\Delta D_{meas}}{D_{meas}} = \sqrt{\left(\frac{E_a \cdot \Delta T}{R \cdot T^2}\right)^2 + \left(\frac{\Delta t}{t}\right)^2 + \left(\frac{2 \cdot \Delta d}{\sqrt{4 D_{meas} t}}\right)^2 + \left(\frac{\Delta D_{fit}}{D_{meas}}\right)^2} \qquad (10)$$

where $E_a$ is the activation energy for lithium diffusion in the $TiS_2$ crystal, $R$ is the universal gas constant and $\Delta D_{fit}$ is the fitting error of the diffusion coefficient. The error of corrected diffusion coefficient $D$ can be defined by error propagation including Equation 9:

$$\frac{\Delta D}{D} = \sqrt{\left(\frac{\Delta D_{meas.}}{D_{meas}}\right)^2 + \left(\frac{(-0.007784 - 0.11685 \cdot z) \cdot \Delta z}{1 - 0.007784 \cdot z - 0.3640 \cdot z^2}\right)^2} \tag{11}$$

with

$$\Delta z = z \cdot \sqrt{\left(\frac{\Delta \varnothing}{\varnothing}\right)^2 + \left(\frac{0.5 \cdot \Delta t}{t}\right)^2 + \left(\frac{0.5 \cdot \Delta D_{meas}}{D_{meas}}\right)^2} \tag{12}$$

# Part C - Kinetics of Lithium Intercalation in $TiX_2$ Single Crystals (X = S, Se, Te) under hydrostatic pressure

The intercalation of lithium into titanium dichalcogenides is accompanied by a considerable expansion of the crystal lattice. When hydrostatic pressure is applied onto the structure, it is compressed mainly in the direction of the *c-axis*, due to the higher compressibility. Thus, the applied pressure counteracts the expansion of the crystals during intercalation. This could influence the intercalation kinetics as more energy is needed to expand the crystal lattice during intercalation. However, the effect of applied pressure on the lithium insertion should vary for the different titanium dichalcogenides used in this work due to their varying properties (e.g. initial lattice parameters, compressibility).

In this section experiments are presented, in which titanium dichalcogenides single crystals $TiX_2$ (X = S, Se, Te) were intercalated at hydrostatic pressures between 10 and 500 MPa. These are compared to experiments at ambient pressure [Schwarzburger 2013]. A study like this yields information about the role of the lattice expansion for the intercalation kinetics in dependence of the chalcogen in the host lattice.

## C.1 Intercalation experiments

Two samples, one surrounded by epoxy and another without epoxy, were inserted into a gold capsule closed at one side by arc-welding. Next, approx. 50 µl of 1.6 $mol \cdot L^{-1}$ n-butyl lithium solution in n-hexane (Sigma Aldrich) was injected into the capsules under protective argon atmosphere, and the open side of the capsule was sealed. The welding plant used (PUK 3 Professional Plus) works with a low energy transfer. Thus, heating of the capsules could be avoided. The volume of solution was large enough to warrant nearly constant BuLi concentration even after complete intercalation.

The capsules were inserted into a Tuttle type autoclave that was connected to an argon gas pressure unit. Subsequently pressure was built up and the autoclave was inserted into a tube furnace. The reaction temperature ranged from 296 to 363 K. In the experiments at room temperature the tube furnace was not switched on and only served as thermal isolation against temperature fluctuations. At elevated temperatures the furnace equipped with a RKC SA 100 controller was used to adjust the temperature. The experimental temperature was controlled by a type-K thermocouple in a bore hole in the outer face of the autoclave, a few millimetres away from the position of the samples. The measured temperature was calibrated against the temperature at the sample position. Temperature was continuously recorded during experiments. Fluctuation of T was typically $< \pm 2$ K at room temperature originating from day to night oscillations. At elevated temperatures the T fluctuations were $< \pm 1$ K. The duration of the intercalation ranged from 5 to 20 d.

After the experiments the capsules were opened and the crystals were taken out and cleaned with ethanol to remove residuals of the BuLi solution from the surfaces. The remaining BuLi solution in the capsule was poured on a tissue to approve its reactivity. The samples were quickly transferred into a liquid nitrogen container where they were stored until measurements to prevent further diffusion. The time between finishing the experiment and placing the sample in liquid nitrogen was less than five minutes, much shorter than the experimental duration, and no significant change in the interior of the crystals is expected due to slow Li diffusion.

## C.2 Results

### C.2.1 Alteration of samples

Photographs of the sample surfaces parallel and perpendicular to the *ab-plane* were taken with a Leica DC 610 microscope to document changes of samples during experiment. The surface parallel to the *ab-plane* of a $TiS_2$ sample that was not encapsulated before an intercalation experiment is shown in Fig. 22a. The surface shows shallow scratches and steps. After the experiment the surface shows uns-

ystematically distributed cracks, typically in 60° and 120° angles (Fig. 22b). The shallow cracks are predominantly close to the sample edges.

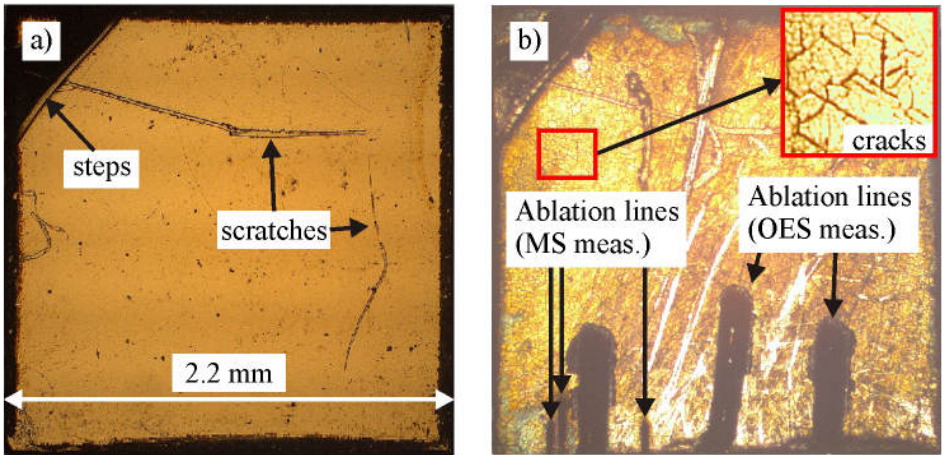


Fig. 22: Microscopical photographs of a crystal (sample TiS2-N23) before (a) and after (b) an intercalation experiment. The photographs show the planes parallel to the *ab-plane*. The different colours of the samples result from different exposure settings of the microscope.

In addition, photographs of the sample edges were taken (perpendicular to the *ab-plane*). In the worst cases, samples were split into multiple sheets after intercalation experiments (Fig. 23a). In the ideal cases, samples didn't show any visible degradation (Fig. 23b).

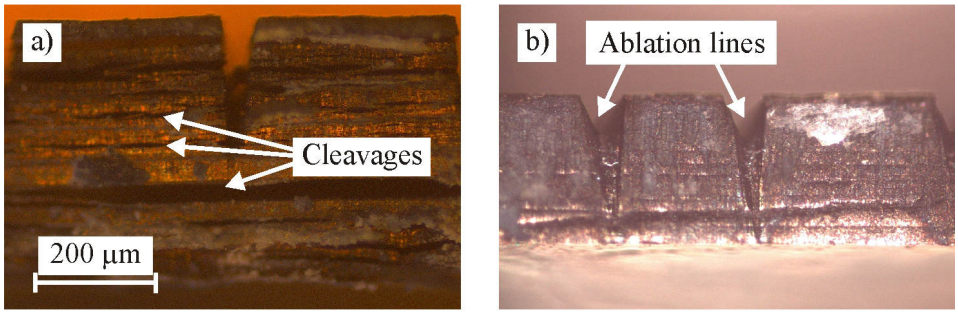


Fig. 23: Microscopical photographs of crystal edges perpendicular to the *ab-plane* after experiments at high temperatures and low pressures (a, sample $TiS_2$-N71, 362 K, 10 MPa, 5 d) and at high pressures and low temperatures (b, sample $TiS_2$-N76, 296 K, 500 MPa, 5 d), respectively.

All of the samples that were intercalated at elevated temperatures show formation of cleavages parallel to the sheets. Cleavages were particularly pronounced at low pressure experiments. It can be noted that intercalated $TiTe_2$ samples showed the lowest fraction of degraded samples compared to the other dichalcogenides.

## C.2.2 Selection of profiles

It was not possible to measure diffusion profiles targeted at sample positions that did not show cracks and cleavages. Therefore the measured profiles were assessed on the basis of microscopical images after the measurements. However, cracks and cleavages are not necessarily visible in the microscopical images and it was also necessary to assess the measured intensity-distance profiles carefully. A rigorous selection was made to ensure that solid state diffusion was the predominant transport process in the intensity-distance profiles that were used for further evaluation.

Cracks in the sheets enable a rapid penetration of BuLi in the direction of the crystallographic *c-axis*. These cracks can develop in the basal plane (Fig. 22b), but also in the planes that are accessible to the

solution when cleavages are formed parallel to the sheets (Fig. 23a). It is worth noting that the dichalcogenides have an excellent wettability. Thus, BuLi can be spread in all crystallographic directions in a strongly degraded crystal. From the closure of the cracks and cleavages lithium then diffuses further into the crystal during the experiment. In other words, cracks and cleavages act as ports to the inner layers so that these are rapidly filled with lithium. When the degradation is limited to the formation of cracks in the basal planes this can be visible as a slightly increased lithium background in the LA-ICP-OES and -MS measurements. When cleavages are formed parallel to the layers this affects the profiles much more serious because cleavages extend deeply into the crystals due to the weak interlayer bonding.

Cleavages develop from the crystal edges into the interior with increasing experimental duration. This means that the zero point of diffusion is shifted into the interior of the crystals in the regions that become accessible to the solution. A strong formation of cleavages in the ablated volume resulted in elevated Li contents in the centre of the crystal as well as high Li contents at the crystal edges (Fig. 24, left).

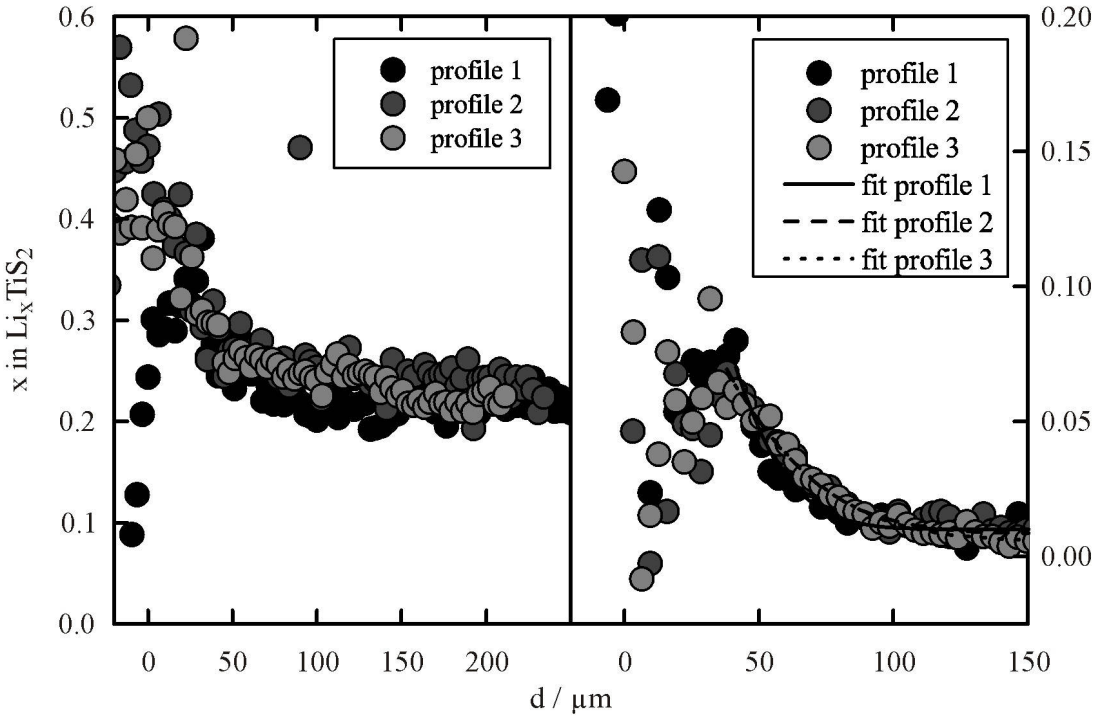


Fig. 24: Profiles measured on the samples that are shown in Fig. 23. (left: sample $TiS_2$-N71, 362 K, 10 MPa, 5 d, 57 µm LASER spot diameter. right: sample $TiS_2$-N76, 296 K, 500 MPa, 5 d, 80 µm LASER spot diameter).

Moreover, LiOH can precipitate inside of cracks and cleavages when the experiments are terminated and the samples get in contact with air. Part of these deposits can be removed at least from shallow cracks in the basal plane by cleaning the samples with ethanol. In some cases measured Li intensities corresponded to x values > 1 in $Li_xTiS_2$. This can be a sign of LiOH precipitation between the sheets or corrosion of the sheets as only one lithium atom per formula unit can be intercalated in $TiX_2$.

Profiles that did show signs of contribution of BuLi penetration to the intercalation process were excluded from further evaluation. When no cleavage was visible in the region of the ablation line, almost all profiles yielded error-function shaped Li profiles which drop to zero in the crystal interior (Fig. 24, right). These measurements were selected for further evaluation.

## C.2.3 Lithium diffusion in titanium dichalcogenides

A total of 101 samples were intercalated under hydrostatic pressure. As described in the preceding chapters the intercalated samples often did not yield lithium content-distance profiles that represent solid state diffusion exclusively but also result from migration of the solution into cracks and cleav-

ages. The rigorous exclusion of these experiments led to a strong reduction of profiles that were evaluated to determine values for $D_{Li}$ and $x_{Li,S}$. A number of 15 experiments that were considered corresponds to an exclusion of 85 % of the conducted experiments, most of which at elevated temperatures and / or low pressures. Table 3 gives an overview of the data.

Table 3: Overview of the experiments that were considered to determine values for $x_{Li,S}$ and $D_{Li}$. The given values for the diffusivities are corrected using Equation 9. Measured values are given in the appendix. An "e" in the sample name marks encapsulation of the sample. Suffixed digits denote different profiles that were measured on the same sample. The value of z is the ratio of beam diameter over profile length as explicated in chapter B.5.3.

| X in $TiX_2$ | sample | T / K | P / MPa | t / d | Analytical method | Spot diameter / µm | z | $x_{Li,0}$ | $x_{Li,S}$ | $D_{Li}$ / $m^2 \cdot s^{-1}$ | $\Delta D_{Li}$ / $m^2 \cdot s^{-1}$ |
|---|---|---|---|---|---|---|---|---|---|---|---|
| S | N22 | 297.3 | 500 | 5.0 | ICP-OES | 98 | 1.78 | 0.01 | 0.27 | $1.34 \cdot 10^{-15}$ | $0.67 \cdot 10^{-15}$ |
| S | N23 | 297.3 | 500 | 5.0 | ICP-OES | 110 | 1.87 | 0.00 | 0.36 | $1.74 \cdot 10^{-15}$ | $0.81 \cdot 10^{-15}$ |
| S | N76.e.1. | 296.1 | 500 | 5.1 | ICP-OES | 80 | 1.21 | 0.01 | 0.16 | $2.04 \cdot 10^{-15}$ | $0.75 \cdot 10^{-15}$ |
| S | N76.e.2 | 296.1 | 500 | 5.1 | ICP-OES | 80 | 1.13 | 0.01 | 0.15 | $2.41 \cdot 10^{-15}$ | $0.82 \cdot 10^{-15}$ |
| S | R1.e | 297.6 | 500 | 19.9 | ICP-OES | 73 | 0.56 | 0.01 | 0.26 | $2.39 \cdot 10^{-15}$ | $0.38 \cdot 10^{-15}$ |
| S | R10.1 | 297.6 | 500 | 19.9 | ICP-OES | 70 | 0.78 | 0.01 | 0.26 | $1.07 \cdot 10^{-15}$ | $0.26 \cdot 10^{-15}$ |
| S | R10.2 | 297.6 | 500 | 19.9 | ICP-OES | 63 | 0.70 | 0.01 | 0.25 | $1.09 \cdot 10^{-15}$ | $0.26 \cdot 10^{-15}$ |
| S | R10.3 | 297.6 | 500 | 19.9 | ICP-OES | 67 | 0.66 | 0.01 | 0.20 | $1.42 \cdot 10^{-15}$ | $0.29 \cdot 10^{-15}$ |
| Se | R5.e.1 | 296.3 | 10 | 5.1 | ICP-OES | 80 | 1.43 | 0.00 | 0.42 | $1.33 \cdot 10^{-15}$ | $0.54 \cdot 10^{-15}$ |
| Se | R5.e.2 | 296.3 | 10 | 5.1 | ICP-OES | 80 | 1.38 | 0.00 | 0.57 | $1.47 \cdot 10^{-15}$ | $0.41 \cdot 10^{-15}$ |
| Se | N15.1 | 297.9 | 300 | 5.0 | ICP-OES | 85 | 1.41 | 0.02 | 0.23 | $1.59 \cdot 10^{-15}$ | $0.63 \cdot 10^{-15}$ |
| Se | N15.2 | 297.9 | 300 | 5.0 | ICP-OES | 85 | 1.35 | 0.02 | 0.45 | $1.79 \cdot 10^{-15}$ | $0.66 \cdot 10^{-15}$ |
| Se | R1.e.1 | 296.1 | 500 | 5.1 | ICP-OES | 58 | 0.97 | 0.00 | 0.71 | $1.80 \cdot 10^{-15}$ | $0.68 \cdot 10^{-15}$ |
| Se | R1.e.2 | 296.1 | 500 | 5.1 | ICP-OES | 58 | 0.94 | 0.00 | 0.66 | $1.93 \cdot 10^{-15}$ | $0.58 \cdot 10^{-15}$ |
| Se | R15.e.1 | 296.4 | 500 | 20.0 | ICP-OES | 90 | 0.78 | 0.03 | 0.71 | $1.79 \cdot 10^{-15}$ | $0.40 \cdot 10^{-15}$ |
| Se | R15.e.2 | 296.4 | 500 | 20.0 | ICP-OES | 74 | 0.61 | 0.05 | 0.67 | $2.06 \cdot 10^{-15}$ | $0.41 \cdot 10^{-15}$ |
| Te | R5.e.1 | 296.3 | 10 | 5.1 | ICP-OES | 55 | 1.55 | 0.01 | 1.00 | $5.1 \cdot 10^{-16}$ | $2.3 \cdot 10^{-16}$ |
| Te | R5.e.2 | 296.3 | 10 | 5.1 | ICP-OES | 59 | 1.72 | 0.00 | 0.97 | $4.3 \cdot 10^{-16}$ | $1.0 \cdot 10^{-16}$ |
| Te | R5.e.3 | 296.3 | 10 | 5.1 | ICP-OES | 49 | 1.47 | 0.00 | 0.93 | $4.6 \cdot 10^{-16}$ | $2.0 \cdot 10^{-16}$ |
| Te | N15 | 296.9 | 300 | 5.0 | ICP-OES | 65 | 1.83 | 0.03 | 0.82 | $3.0 \cdot 10^{-16}$ | $1.1 \cdot 10^{-16}$ |
| Te | N16.1 | 296.1 | 300 | 5.0 | ICP-OES | 63 | 1.81 | 0.04 | 0.74 | $3.8 \cdot 10^{-16}$ | $1.3 \cdot 10^{-16}$ |
| Te | N16.2 | 296.1 | 300 | 5.0 | ICP-OES | 61 | 1.81 | 0.03 | 0.76 | $2.3 \cdot 10^{-16}$ | $1.0 \cdot 10^{-16}$ |
| Te | R4.e.1 | 297.4 | 500 | 5.1 | ICP-OES | 44 | 2.18 | 0.04 | 1.00 | $1.0 \cdot 10^{-16}$ | $0.6 \cdot 10^{-16}$ |
| Te | R4.e.2 | 297.4 | 500 | 5.1 | ICP-OES | 42 | 2.11 | 0.03 | 1.00 | $5.6 \cdot 10^{-17}$ | $3.9 \cdot 10^{-17}$ |
| Te | R12.e.1 | 297.2 | 500 | 19.9 | ICP-MS | 23 | 0.86 | 0.00 | 0.82 | $9.4 \cdot 10^{-17}$ | $3.0 \cdot 10^{-17}$ |
| Te | R12.e.2 | 297.2 | 500 | 19.9 | ICP-MS | 23 | 1.29 | 0.00 | 1.00 | $3.7 \cdot 10^{-17}$ | $2.6 \cdot 10^{-17}$ |
| Te | R12.e.3 | 297.2 | 500 | 19.9 | ICP-MS | 23 | 0.85 | 0.05 | 0.87 | $9.8 \cdot 10^{-17}$ | $3.0 \cdot 10^{-17}$ |
| Te | R14 | 297.2 | 500 | 19.9 | ICP-MS | 15 | 0.41 | 0.00 | 0.59 | $1.9 \cdot 10^{-16}$ | $0.6 \cdot 10^{-16}$ |

### C.2.3.1 Variations of $D_{Li}$ within a sample

All dichalcogenides samples, which were rated intact based on microscopic images, yielded reproducible intensity-distance profiles. The diffusions coefficient on one sample varied at most by a factor of 1.2 and 1.1 for $TiS_2$, $TiSe_2$, respectively. Titanium ditelluride samples showed a higher variation of diffusion coefficients (factor of 2.6 at most), which is due to the shorter profile lengths. Diffusion profiles that were measured on the same intercalated $TiS_2$ sample is shown in Fig. 25. The distance be-

tween the profiles was approx. 300 µm, the derived diffusion coefficients are $(1.07 \pm 0.26) \cdot 10^{-15}$ $m^2 \cdot s^{-1}$, $(1.09 \pm 0.26) \cdot 10^{-15}$ $m^2 \cdot s^{-1}$, and $1.42 \pm 0.29 \cdot 10^{-15}$ $m^2 \cdot s^{-1}$, respectively.

However, for most of the samples only one or two of the measured intensity-distance profiles could be used to determine diffusion coefficients because a part of the profiles deviated from error function shape which indicates that cracks and cleavages might have been present in these samples to a minor extent but were not visible in the microscopic images.

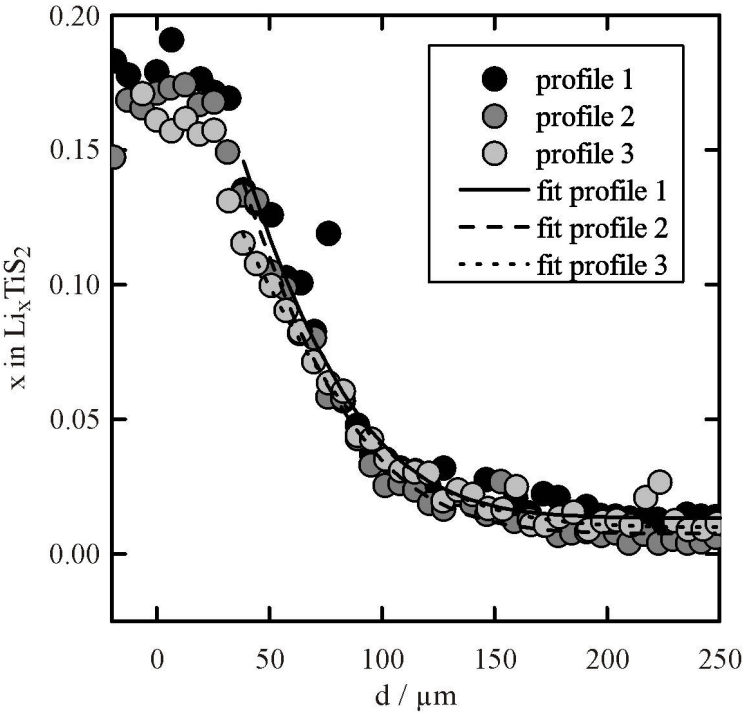


Fig. 25: Diffusion profiles measured on one sample (sample $TiS_2$-R10, 298 K, 500 MPa, 20 d, 67 µm LASER spot diameter). Lines represent the part of the profiles that was used for fitting.

## C.2.3.2 Time dependence

The time dependence of $x_{Li,S}$ (Fig. 26) and $D_{Li}$ (Fig. 27) was systematically studied near room temperature (296 – 298 K) at high pressure (500 MPa). For intercalated $TiS_2$ the variation of Li surface contents is high for short run durations compared to longer run durations which can be explained by the uncertainty of the zero point of diffusion. This can also be seen from $x_{Li,S}$ values in intercalated titanium ditelluride, where diffusion profiles were particularly short and many profiles had to be excluded from evaluation. Two profiles from samples intercalated at 500 MPa and room temperature for 5 days were evaluated with a correction of the zero point of diffusion (section B.5.1) using a constant value of $x_{Li,S} = 1$ as a constraint. However, lithium surface contents that were determined from samples intercalated for 20 days are much more significant in the case of $TiTe_2$.

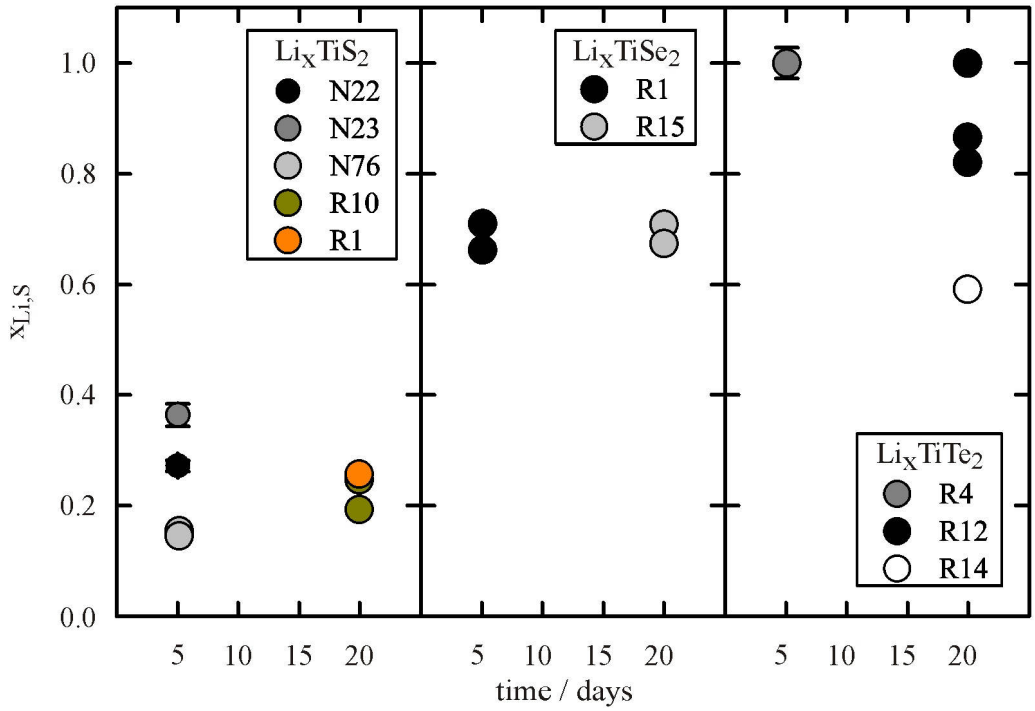


Fig. 26: Time dependence of $x_{Li,S}$ at 500 MPa.

In general, the length of diffusion profiles increases with run duration and remains roughly constant when scaling with the square root of time (not shown here), which is consistent with a diffusion controlled process.

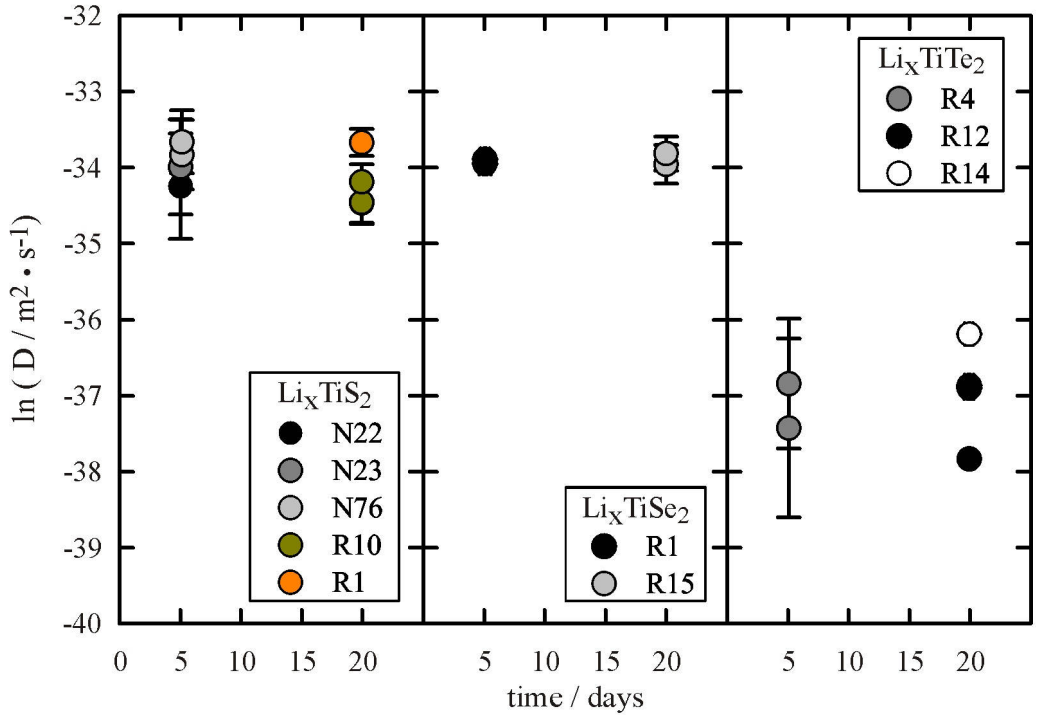


Fig. 27: Time dependence of Li diffusivity at 500 MPa.

### C.2.3.3 Pressure dependence

The pressure dependence of $D_{Li}$ and $x_{Li,S}$ was systematically studied near room temperature (296 - 298 K). All dichalcogenides were intercalated at 10, 300 and 500 MPa. As mentioned in section C.2.1 samples that had been intercalated at lower pressures were predominantly excluded because of degra-

dation. For $TiS_2$ only samples intercalated at 500 MPa could be evaluated. For $TiSe_2$ and $TiTe_2$ a variety of high pressure conditions (10, 300 and 500 MPa) yielded samples, for which lithium intercalation was controlled by solid state diffusion. Diffusivities and surface contents are compared to data from intercalation experiments at ambient pressures and room temperature [Schwarzburger 2013].

Lithium surface contents in intercalated titanium disulfide crystals are in the same range at ambient and high pressures (Fig. 28). For titanium diselenide and titanium ditelluride $x_{Li,S}$ values are in the same range at high pressure experiments. The data from ambient pressure experiments show a larger variation compared to high pressure experiments. Moreover titanium ditelluride $x_{Li,S}$ values are elevated compared to ambient pressure experiments.

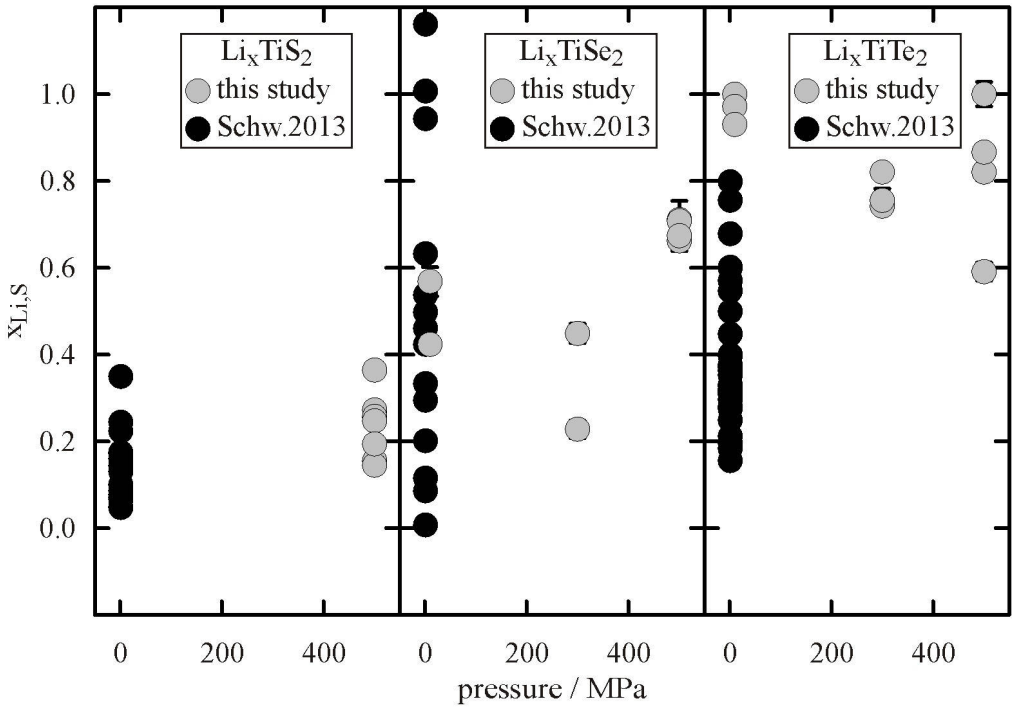


Fig. 28: Pressure dependence of $x_{Li,S}$ at room temperature.

Diffusivities of samples intercalated at high pressures are in the range of the lowest diffusivities from ambient pressure experiments (Fig. 29).

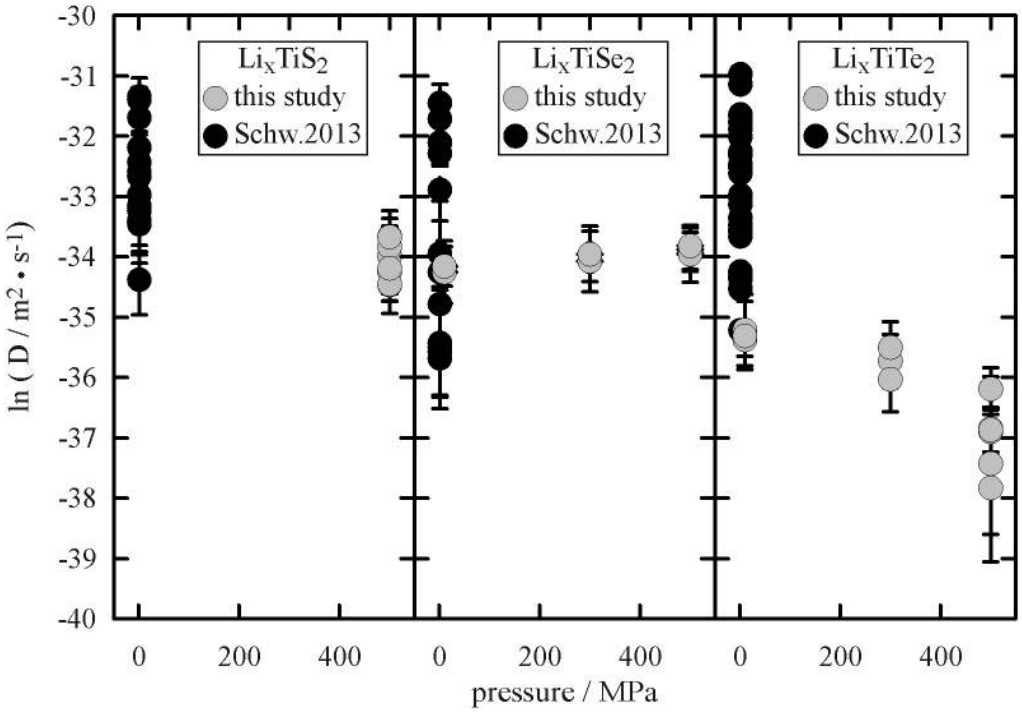


Fig. 29: Pressure dependence of Li diffusivity at room temperature.

For titanium diselenide, samples intercalated at 10, 300 and 500 MPa diffusivities are in the same range. For titanium ditelluride, diffusivities systematically decrease with increasing pressure. Moreover it can be noted that the variation of diffusivities is much higher at ambient pressure experiments.

#### C.2.3.4 Dependence of $D_{Li}$ on the type of Anion

All $x_{Li,S}$ values and diffusion coefficients of the dichalcogenides for experiments conducted at 500 MPa and room temperature are displayed in Fig. 26 and Fig. 27. Lithium surface contents are lower for intercalated $TiS_2$ than for $TiSe_2$ and $TiTe_2$ (Fig. 26). The values of $x_{Li,S}$ are between 0.15 to 0.36 for $TiS_2$, 0.66 to 0.71 for $TiSe_2$ and 0.59 and 0.99 for $TiTe_2$. The diffusivities of Li are in the same range for $TiS_2$ ((1.07 to 2.41) $\cdot 10^{-15}$ $m^2 \cdot s^{-1}$) and $TiSe_2$ ((1.48 to 2.10) $\cdot 10^{-15}$ $m^2 \cdot s^{-1}$) while diffusion coefficients are significantly lower for $TiTe_2$, particularly at high pressures ((0.07 to 0.55) $\cdot 10^{-15}$ $m^2 \cdot s^{-1}$).

## C.3 Discussion

### C.3.1 Kinetics of Li-intercalation into titanium dichalcogenides

Li intercalation into layered dichalcogenides is accompanied by various changes of structural, elastic and electronic properties while the trigonal symmetry of the dichalcogenides is preserved [Bensch et al. 2009, Patel and Balchin 1985]. The kinetics of the first step of the intercalation process, i.e. the transport of Li in the solution to the surface of the crystals is the same for the different dichalcogenides. Subsequent steps depend on several factors.

#### C.3.1.1 Transport of lithium to the crystal surface

To show that a sufficient supply of Li can be provided for the current experimental conditions and for all dichalcogenides a worst case scenario is considered (see section A.2.1).

Due to the higher viscosity of the solution (0.297 mPa · s at 0.1 MPa and 298 K, 2.646 mPa · s at 500 MPa and 298 K) the diffusivity of BuLi decreases with increasing pressure. Compared to ambient pressure experiments [Schwarzburger 2012] BuLi diffusion was slower by factors of 1.2, 5.8 and 8.9 at 10, 300 and 500 MPa, respectively.

At 500 MPa the diffusivity is approx. $1.0 \cdot 10^{-13}$ $m^2 \cdot s^{-1}$. For a BuLi concentration of 1.6 mol $\cdot$ $L^{-1}$, the product of D $\cdot$ C is $1.6 \cdot 10^{-10}$ mol $\cdot$ $m^{-1}$ $\cdot$ $s^{-1}$ at these conditions. The highest concentration of Li in the intercalated samples are $1.1 \cdot 10^4$ mol $\cdot$ $m^3$ for $TiS_2$, $2.23 \cdot 10^4$ mol $\cdot$ $m^3$ for $TiSe_2$ and $1.9 \cdot 10^4$ mol $\cdot$ $m^3$ for $TiTe_2$ corresponding to x values of 0.4, 1 and 1. The maximum diffusion coefficients at room temperature are at least 2.4, 2.1 and $1.3 \cdot 10^{-15}$ $m^2 \cdot s^{-1}$ for the sulfides, selenides and tellurides, respectively. At room temperature the products of D $\cdot$ C in the crystals are 3.3, 6.1 and 6.6 times higher than in the solution. Therefore, the diffusive transport of Li in the solution can be considered fast enough to provide a sufficient supply of Li in all experiments. In addition, convection in the low viscosity liquids probably enhances the transport of BuLi to the crystal surface.

### C.3.1.2 Electronic properties of the chalcogenides and charge transfer from Li to the host lattice

Kim et al. investigated the interlayer bonding which was found not to be only van der Waals type. Bond overlap populations calculated for X-X bonds yielded 0.025, 0.029 and 0.05 $eV^{-1} \cdot atom^{-1}$ for S, Se and Te, respectively [1998]. The higher bond overlap population possibly accounts for the less degradation we observed for the intercalation of $TiTe_2$ as the bonding between the layers is stronger.

Some studies [Hibma 1980, Fang et al. 1997, Kim et al. 1998, Umrigar et al. 1982] reported a decreasing ionicity and increasing covalence from S to Se and Te, which is consistent with a decreasing difference of the electronegativity between titanium and the chalcogen. Due to the differences in electronegativies between the chalcogens, we assume that the ionicity of the Ti-X intralayer bonding increases from S to Se and Te also for the intercalated compounds.

Lithium transfers one electron to the host lattice while the charge of the chalcogen layers varies. Hence, the stabilization of lithium at the transition state of the diffusion path is different, i.e. more negatively charged chalcogen layers should provide a better stabilization and thus a lower barrier for diffusion. Therefore the lower lithium diffusivity titanium ditelluride can be a result of less ionic Ti-Te intralayer bonding compared to Ti-S and Ti-Se bonding.

In fact, activation energies of lithium diffusion determined by Schwarzburger [2013] from intercalation of $TiX_2$ single crystals using 1.6 M BuLi solution at ambient pressure were higher for $TiTe_2$ (66.8 $\pm$ 8.8 kJ $\cdot$ $mol^{-1}$) compared to $TiS_2$ (59.6 kJ $\cdot$ $mol^{-1}$) and $TiSe_2$ (53.6 kJ $\cdot$ $mol^{-1}$).

### C.3.1.3 Incorporation of lithium ions in $TiX_2$ and expansion of the lattice

The interlayer distance prior to intercalation increases with the atomic number of the chalcogen from 2.846 Å ($TiS_2$) to 2.943 Å ($TiSe_2$) and 3.083 Å ($TiTe_2$). The interlayer distance depending on the intercalation degree (

Table 4) can be calculated from the lattice parameter *c* and the atomic *z* coordinate of the chalcogen in the unit cell:

$$d_{vdW} = (1 - 2z) \cdot c \tag{13}$$

As the van der Waals gap is initially bigger for $TiSe_2$ and $TiTe_2$, the expansion of the lattice during intercalation is smaller.

Table 4: Structural properties for pure and intercalated dichalcogenides as well as strain induced by intercalation

| Compound | a [Å] | c [Å] | z | c-2zc [Å] | ε |
|---|---|---|---|---|---|
| $TiS_2$ | 3.4073 (2)[a] | 5.6953 (2)[a] | 0.2501[a] | 2.846 | 0.00 |
| $Li_{0.25}TiS_2$ | 3.415[b] | 6.04[b] | | | 0.06 |
| $LiTiS_2$ | 3.4590 (3)[b] | 6.1879 (6)[b] | 0.238 (1)[b] | 3.243 | 0.09 |
| $TiSe_2$ | 3.540 (1)[c] | 6.008 (3)[c] | 0.25504 (3)[c] | 2.943 | |
| $TiSe_2$ | 3.541 (2)[d] | 6.001 (5)[d] | | | 0.00 |
| $LiTiSe_2$ | 3.633 (3)[d] | 6.474 (7)[d] | | | 0.08 |
| $TiTe_2$ | 3.777 (3)[e] | 6.498 (6)[e] | 0.2628 (1)[e] | 3.083 | |
| $TiTe_2$ | 3.768 (3)[f] | 6.524 (6)[f] | 0.255[f] | 3.197 | 0.00 |
| $LiTiTe_2$ | 3.820 (6)[f] | 6.925 (11)[f] | 0.25[f] | 3.463 | 0.06 |

Note: [a] from ref [Chianelli et al. 1975],[b] from ref [Dahn et al. 1980], [c] from ref [Reikel1976], [d] from ref [Patel and Balchin 1983], [e] from ref [Arnaud1981], [f] from ref [Patel and Balchin 1985]

This could explain the higher $x_{Li,S}$ values for $TiSe_2$ and $TiTe_2$. When Li is intercalated into $TiS_2$, sites are favoured that are already expanded because of the energy needed to expand the gap. When Li is intercalated into $TiSe_2$ and $TiTe_2$ less energy is required for the expansion of the gap. Therefore empty sites adjacent to intercalated regions in a sheet have no preference compared to non-intercalated regions. This leads to $x_{Li,S}$ values close to 1 meaning that nearly every unit cell at the crystal edge incorporated Li. Moreover, it can be seen that the strain at fully intercalated dichalcogenides is the lowest for $TiTe_2$. This is in good agreement with our observation that degradation of $TiTe_2$ during intercalation was less severe than for $TiSe_2$. Due to the lower intercalation degree in $LixTiS_2$ the resulting strain is comparable to fully intercalated $LiTiTe_2$, but the bonding between the sheets is stronger in $TiTe_2$ than in $TiS_2$.

## C.3.2 Pressure effects

The effect of pressure on lithium diffusivity was estimated in section A.3, using the ionic volume of lithium as activation volume. On this basis, an expected reduction of the diffusivity was calculated. For a temperature of 298 K the calculation yields a decrease of approx. 10 % at a pressure of 500 MPa relative to ambient pressure. However, the estimation does not account for differences between the dichalcogenides or possible changes of the matrix (e.g. transformations of the crystal structure or the electronic structure) due to pressure application, which might affect the intercalation kinetics. Lithium diffusivities determined under application of hydrostatic pressure were in the range of the lowest diffusivities that were determined at ambient pressure [Schwarzburger 2013]. Furthermore, lithium diffusivities in $TiTe_2$ decreased systematically with increasing pressure. These variations exceed the estimated reduction of the diffusivity considerably. Therefore, possible pressure effects are discussed in the following in relation to the presented results.

Liu et al. [2011] found that the resistivity of $TiS_2$ decreases and the electron density increases linearly with pressure (see chapter A.3). Linear regression of their data yields an increase of electron density of approx. 0.1 at 10 MPa and 6.7% at 500 MPa compared to atmospheric pressure.

The increase of electron density in the van der Waals gap might affect the chemical potential of the electron transfer reaction of Li to the host lattice as well as the interlayer bonding but this is out of the scope of the present study and is not expected to play a crucial role for our results.

For $TiS_2$ the hydrostatic pressures applied in this work lead to a compression of the van der Waals gap by approx. 0.02% at 0.01 GPa and 0.88% at 0.5 GPa (Table 5).

Table 5: Compression of $TiS_2$. Values for c, z and the layer thickness c-(2cz) are calculated after Clerc et al. [1996].

| Pressure [GPa] | c [A] | z | c-(2cz) [Å] |
|---|---|---|---|
| 0 | 5.6653 | 0.2501 | 2.8315 |
| 0.01 | 5.6647 | 0.2501 | 2.8310 |
| 0.5 | 5.6343 | 0.2509 | 2.8067 |

A strong pressure effect on the diffusivity of Li in the crystal due to the reduction of the van der Waals gap is not expected for $TiS_2$. Nevertheless, the ability of the chalcogen atoms to rearrange when lithium is inserted into the structure is reduced when the structure is compressed.

In fact, the diffusivities at hydrostatic pressures were in the range of the lowest diffusivities determined at ambient pressures by Schwarzburger et al [2012]. However, the higher variation of ambient pressure data indicates that a part of the evaluated profiles is affected by BuLi migration. Especially high diffusivities probably result from experiments where BuLi migration into cleavages contributed to the lithium transport. Thus, in the case of $TiS_2$, the reason for the diffusivities at hydrostatic pressures being in the lower range of diffusivities at ambient pressure is probably the more rigorous exclusion of content-distance profiles affected by BuLi migration in the current study. Furthermore, fanning of the sheets could have been suppressed by the application of pressure.

No data for the compression of $TiSe_2$ and $TiTe_2$ is available to us. However, the stiffness in the direction of the *c-axis* is lower for $TiSe_2$ (39 GPa) [Stirling, Dorner, Chuke and Revelli1976] compared to $TiS_2$ (55 GPa) [Schärli and Levi 1986]. This is probably due to less electrostatic repulsion in $TiSe_2$ because of the lower ionicity of the Ti-Se intralayer bonding. Therefore the pressure effect on the mobility should be higher compared to $TiS_2$ due to a higher compression. However, the lithium diffusivities in $TiSe_2$ are in the same range at ambient pressure compared to high pressure data. Moreover, diffusivities that were determined from experiments at hydrostatic pressures of 10, 300 and 500 MPa showed a low variation. This indicates that the application of pressure did not affect the lithium mobility in $TiSe_2$ strong enough considering the variation of our data.

Lithium diffusion coefficients decreased significantly with increasing pressure for $TiTe_2$. Following the same argumentation like for $TiSe_2$, the compressibility is probably the highest for $TiTe_2$ compared to $TiS_2$ and $TiSe_2$ because the repulsion between the chalcogen layers is the lowest. When the tellurium layers approach the barrier for lithium jumps increases because the transition state is less stabilized compared the other chalcogenides.

The observation that Li surface contents are not lower at hydrostatic pressures compared to ambient pressures could indicate that the strain energy that is needed to expand the gaps is not significantly higher in the pressure range in this study. On the other hand, the activity of butyl lithium is higher when pressure is applied, which might support the insertion of lithium. Thus, the effect of the lattice compression could be compensated by the compression of the solution.

## C.3.3 Comparison to literature

Jump rates of lithium in $TiS_2$ powder samples have been determined by several authors using Nuclear Magnetic Resonance Spectroscopy. These jump rates represent Li self diffusion in a homogenous medium. A comparison between these data and chemical diffusion coefficients in single crystals revealed that the strain energy for widening of the crystals makes a significant contribution to the activation energy for chemical diffusion [Schwarzburger et al. 2012].

Bensch et al. [2009] determined jump rates for $TiS_2$ and $TiSe_2$. They found higher jump rates for Li in $TiS_2$ ($2 \cdot 10^6$ $s^{-1}$) than for TiSe2 ($1.8 \cdot 10^5$ $s^{-1}$) at 322 K. Diffusion coefficients can be calculated via the Einstein-Smoluchowski Equation:

$$\tau_i^{-1} = \frac{g \cdot D}{\alpha^2} \qquad (14)$$

where $g$ is the geometrical factor (4 for two dimensional systems), $\tau_i$ is the average resident time of ion $i$ on a site and $\alpha$ is the jump distance assumed to be given by the distance between octahedral sites within a layer ($\alpha$ = 3.408 Å) [Levy79, Clerc et al. 1997]. In detail the jump mechanism is more complex and may involve passing a transitional tetrahedral site during jump from one octahedral to an adjacent one [Wilkening and Heitjans 2008], depending on the intercalation degree. However, this is not relevant for the comparison.

The calculation yields diffusion coefficients of $5.8 \cdot 10^{-14}$ $m^2 \cdot s^{-1}$ for $TiS_2$ and $0.52 \cdot 10^{-14}$ $m^2 \cdot s^{-1}$ $TiSe_2$, respectively. Schwarzburger determined similar diffusivities at 322 K [Schwarzburger 2013] using 1.6 M n-BuLi solution ($9.7 \cdot 10^{-15}$ to $4.4 \cdot 10^{-14}$ $m^2 \cdot s^{-1}$ for $TiS_2$ and $6.3 \cdot 10^{-15}$ to $5.3 \cdot 10^{-14}$ $m^2 \cdot s^{-1}$ for $TiSe_2$) though lithium diffusivities are slightly lower in $TiS_2$ compared to the values of Bensch et al., which could be assigned to the strain energy that is needed to expand the van der Waals gap. A difference of the lithium diffusivities in $TiS_2$ and $TiSe_2$ could not be resolved from the diffusivities determined by Schwarzburger.

The diffusion coefficients presented in this work are lower ($1.7 \cdot 10^{-15}$ $m^2 \cdot s^{-1}$ and $1.5 \cdot 10^{-15}$ $m^2 \cdot s^{-1}$) which can be assigned to the lower temperature. Moreover no difference in diffusivities of lithium in $TiS_2$ and $TiSe_2$ was observed. If lithium diffusion is slower in homogeneous powder samples of $TiSe_2$ compared to $TiS_2$ while diffusion coefficients are similar for chemical diffusion in single crystals, the strain energy that is needed to expand the van der Waals gaps should be higher in $TiS_2$. This is consistent with initially larger size of the gaps in $TiSe_2$.

Eguchi et al. [1981] measured the temperature variation of the $^7$Li NMR lineshape in $Li_{0.9}TiS_2$ powders at pressures from 0.1 to 500 MPa. They calculated correlation times for Li at atmospheric pressure and at 500 MPa at room temperature. The diffusion coefficients that are calculated from the correlation times are 1.3 and $0.65 \cdot 10^{-12}$ $m^2/s$ for 0.1 and 500 MPa, respectively. The diffusivities reported by Eguchi et al. cannot be related directly to our results because of the strain energy that is required to expand the lattice in single crystals. However, the results of Eguchi et al. appear to be too high to be ascertained solely to this effect.

## C.4 Conclusions

Li-intercalation kinetics in titanium dichalcogenide single crystals is controlled by self diffusion of lithium in the host lattice as well as interlayer forces and strain induced by Li insertion which depends on the crystal structure of the dichalcogenides. As a consequence, lithium distribution at the edges, diffusivities in the lattices and stability of the crystals vary for the different dichalcogenides in this work. Moreover, the pressure dependence of lithium intercalation depends on the properties of the dichalcogenide. Due to the variation of the data it was only possible to resolve the pressure dependence of lithium diffusivity in $TiTe_2$.

The application of hydrostatic pressure during intercalation experiments yielded diffusivities in the lower range of experiments at ambient pressures. The main reason for this observation is probably the rigorous selection of profiles that represent solid state diffusion in this work and are not affected by migration of the solution into the crystals. The application of pressure also could have counteracted fanning of the $TiX_2$ sheets, which is indicated by the observation that samples intercalated at higher pressures in this work showed less formation of cleavages.

# Part D - A new type of uniaxial high pressure cell for chemical intercalation experiments of titanium dichalcogenide single crystals

In the previous section titanium dichalcogenide crystals were intercalated under hydrostatic pressures, which yielded new findings about the role of the lattice expansion for the intercalation process depending on chalcogen in $TiX_2$ (X = S, Se, Te).

However, the applicable pressure range was limited to 500 MPa. A systematic decrease of diffusion coefficients could only be observed for $TiTe_2$, while a pressure dependence of lithium diffusivities in $TiS_2$ and $TiSe_2$ could not be observed. In other words: the pressure effect on lithium intercalation is too low to be resolved, considering the variation of the data. Thus, it is necessary to conduct intercalation experiments at higher pressures and / or reduce variation of the data.

These demands led to the development of a new cell that allows conducting intercalation experiments under uniaxial pressure. The range of the applicable pressure is practically limited by the stability of the titanium dichalcogenide crystals. It was possible to intercalate $TiS_2$ crystals at 885 MPa, which is considerably higher, compared to hydrostatic pressure experiments. The estimated reduction of diffusivity at 885 MPa and 304 K is approx. 17 %. Moreover, the BuLi solution is under ambient pressure in the intercalation experiments using the new cell. This could reduce sample degradation compared to hydrostatic experiments, in which the solution was also under high pressure, and thus, reduce variation of the data.

In this section, the focus lies on the development of the new uniaxial compression cell. This comprises designing a cell, in which intercalation experiments could be conducted under protective atmosphere while applying pressure from outside of the cell (ambient atmosphere) onto pistons, which are led to the sample position. Moreover, the movement of the pistons should be measured during the intercalation experiments to get information about the change in sample thickness. These changes are small. Therefore, measurements had to be very close to the sample position to minimize contributions of other cell components (e.g. thermal expansion of the pistons). Additionally, a constant cell temperature has to be maintained during the whole experiment. The requirements described, result in a compact construction of the cell. At the same time an easy handling of the cell has to be maintained, in spite of the limited space.

The development of the cell also comprises the selection of appropriate materials for each component of the cell. In particular, it was crucial to use materials that were not damaged by the application of pressure or due to reaction with BuLi.

This section includes a description of the cell set-up and results of various tests of the cell as well as first results from intercalation experiments of $TiS_2$ at varying pressures and a temperature of approx. 304 K.

## D.1 The Cell

The cell consists of an externally heated chromium nickel steel (X5CrNi18-10) cylinder and an inner sample chamber. The sample is intercalated and pressurized between two pistons. The cell assemblage is shown schematically in Fig. 30.

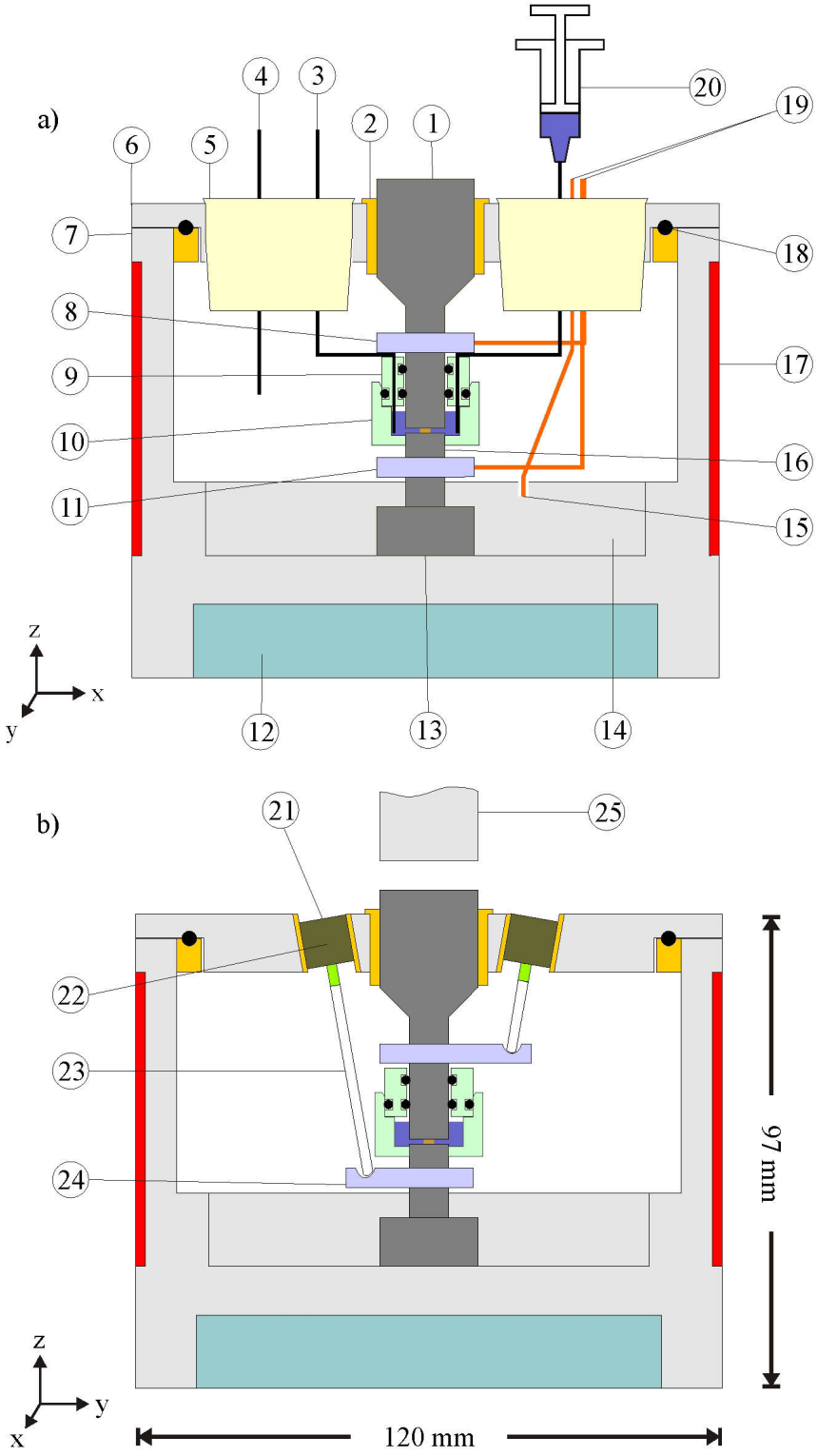


Fig. 30: Schematic drawings of the cell. a and b are orthogonal sections and show BuLi injection (a) and displacement measurement of the pistons (b). a: 1 = upper piston, 2 = brass feed through, 3 = cannula for pressure balance, 4 = cannula for purging of the cell, 5 = rubber stopper, 6 = cell lid, 7 = cell body, 8 = upper support plate, 9 = sample chamber lid, 10 = sample chamber beaker, 11 = lower support plate, 12 = load cell, 13 = tungsten carbide disc, 14 = base plate, 15 = temperature meausurement in the base plate, 16 = lower piston, 17 = silicon heating element, 18 = o-ring gasket, 19 = thermocouples, 20 = BuLi injection. b: 21 = LVDT sensor, 22 = core of the LVDT sensor, 23 = fused silica rod, 24 = dimple in the support plate for positioning of the fused silica rod, 25 = steel rod

The outer hollow cylinder is open on one side (top of the cell). A lid (**6**) can be screwed to the opening with an o-ring (**18**) between the parts for sealing. The lid contains two brass feed throughs for LVDT (Linear variable differential transformer) position sensors and one for the upper piston, as well as two recesses for rubber stoppers (**5**), through which cannulas and thermocouples are fed through.

A pocket in the bottom of the cylinder serves as a fitting for a load cell (HBM U3, **12**). The load cell has a nominal force of 100 kN and a nominal sensitivity of 2 mV / V. The relative deviation at compressive force is < ± 0.2 % and the effect of temperature on the sensitivity is < 0.1 % / 10 K.

The intercalation cell is heated with a hotset C448 compact control cabinet and a silicon heating element (hotset hotform®, **17**). A recess on the circumference, which is 54 mm in height and 2 mm in depth (the diameter of the cylinder is 116 mm at the recess) serves as a fitting for the heating element. The dimensions of the silicon foil were ordered custom-fit to the cell dimension. The length of the foil is 345 mm, which is slightly shorter compared to the circumference of the cylinder at the recess (approx. 364.5 mm). This was necessary to provide space for power supply and thermocouple connections. The foil is equipped with a Fe-CuNi thermocouple (j-type), which allows controlling its temperature directly. The power density of the heating element is 2 W / $cm^2$ at 230 V, corresponding to a surface temperature of 370 °C. However, the temperature resistance of the foil for long term heating is 200 °C. The silicon heating element is fastened on the circumference of the cylinder using a tension band, which was also fitted to the cell dimensions.

A base plate (**14**) in the cylinder contains pockets for the lower piston (8 mm in diameter and 15 mm in height, **16**) and a disc underneath (20 mm in diameter and 10 mm in height, **13**), which is used to spread the applied pressure to a larger area. These components as well as the upper piston (**1**) are exposed to high pressures, when samples are compressed. It was crucial to choose a material for these components, which is not deformed at the pressures, which were targeted. The chromium nickel steel that was used for the cylinder was not suitable, because would start to deform plastically at pressures above the proof stress $R_{P0.2}$ (0.2 % irreversible deformation after decompression), which is 190 MPa. Therefore, steel was excluded as material for the pistons, even though some steel grades exhibit a higher proof stress (e.g. quenched and tempered steels) compared to the chromium nickel steel. Instead, tungsten carbide was chosen, as it offers a very high yield stress of 6.8 GPa (beginning of plastic deformation).

The top of the lower piston is glued into a borehole in the beaker (11 mm in diameter and 13 mm in height, **10**) of the sample chamber using epoxy (Araldit 2020®). The sample chamber could not be made of PTFE, as butyl lithium is a strong reducing agent. Thus, PVC was used, which offers good chemical resistance against the solution.

The connection of beaker and lid (9 mm in diameter and 10 mm in height, **9**) is sealed gas tight with an o-ring in a groove on the circumference of the lid. The upper piston, which is 20 mm in diameter at the top and is reduced to a diameter of 8 mm, is fed through a bore hole in the lid. The connection is sealed with two o-rings that are positioned in grooves in the wall of the borehole. Two further boreholes are used to feed cannulas (**3** and **20**) through the lid into the sample chamber. The connection between cannulas and boreholes is sealed with epoxy.

Support plates (**8** and **11**) that are fastened with screws at the upper and the lower piston enable displacement measurements of the pistons. Fused silica rods (**23**) carry PVC adapters for the cores of the LVDT sensors at the top. The adapters consist of a hollow cylinder on one side and a thread for the core of the LVDT on the other. The rod is plugged into the hollow cylinder and the parts are glued together. The core is screwed onto the thread of the adapter. The bottom of the rods can be positioned in dimples in the support plates. The measurement range of the LVDT sensors (Schaevitz™ 050MHR, **21**) is ± 1.27 mm with a non-linearity of ± 0.25 % at the full measurement range. However, position measurements were close to the central position of the core in the sensor and thus, non-linearity was negligible. The signal of the sensor was amplified using a Single channel LVDT/RVDT-Amplifier (MC-KP-24E-B10, Althen) with an analogue output of ± 10 V for the measurement range. The output signal corresponds to a sensitivity of approx. 8 mV / µm. A data logger (Graphtec GL220-EU) was used for A/D conversion and data recording. The resolution of the position measurement is limited by electronic noise. The core displacement in the LVDT sensor was measured with a resolution of 1 µm.

The experimental temperature is measured in boreholes in the support plates a few millimetres away from the position of the sample using Cu-CuNi thermocouples (t-type, **19**). Pressure is applied with an

electrical piston pump that is connected to an oil hydraulic cylinder. Pressures up to 20 MPa can be build up in the oil hydraulic cylinder onto the pump rod with a diameter of 80 mm. The pressure is transferred to the upper tungsten carbide piston with a steel rod (20 mm in diameter, **25**) as connecting piece. The pressure that is generated in the oil hydraulic cylinder is increased by a factor of 100 at the lower face of the upper tungsten carbide piston.

# D.2 Experimental

## D.2.1 Samples

Generally, crystals with well developed surfaces were chosen for the intercalation experiments in this work. For the intercalation experiments under uniaxial pressure, it was even more important that the crystals were free of steps on the surface, which could lead to an uneven pressure transfer and thus, cause stress and damage the crystal. For the same reason it was important to chose crystals that showed small deviation from coplanarity. Therefore, thickness of the square-shaped crystals was measured optically at the 4 edges using the Leica DC 610 microscope, which was calibrated with a certified scale. The thickness varied by 1 to 10 µm depending on the total thickness of the sample. The stoichiometry of most samples was calculated using the position of the plasma edge in the reflectivity spectra. Values for y in $Ti_{1+y}S_2$ are given in Table 6 (section D.3.5).

All crystals were encapsulated by a thin layer of epoxy. The procedure of encapsulation as well as advantages and drawbacks are described in general in chapter B.2. The advantage of this strategy for uniaxial pressure experiments is that small deviation from coplanarity of the sample is evened out and pressure spikes due to sample roughness are absorbed as the applied pressure is spread laterally at prominent structures on the crystal surfaces.

## D.2.2 Intercalation experiments and in situ measurements of sample thickness change

The sample was placed on the face of the lower piston prior to cell assemblage. The sample chamber was then closed with the lid and the upper piston was pressed manually onto the sample. Subsequently thermocouples and silica rods were installed. The core can be positioned centrally in the LVDT sensor by adjusting the position of the support plates and by adjusting the position of the LVDT sensor with a screw in the feed trough.

The silica rods are led to the support plates at an angle of 10 °. The displacement of the support plate (equals the displacement of the piston) can be calculated with Equation 16:

$$\Delta L_{piston} = \sin 10° \cdot \Delta L_{core} \qquad (16)$$

where $\Delta L_{piston}$ is the displacement of the piston and $\Delta L_{core}$ is the displacement of the core in the LVDT sensor. The measurement at the lower piston serves as a reference measurement that allows correcting the displacement of the upper piston due to possible thermal expansion or contraction of cell parts. For the same reason temperatures were measured at both pistons as well as the base plate.

After the installation of LVDT sensors and thermocouples, the cell was closed and placed on the force transducer centrally below the oil hydraulic cylinder. For thermal isolation, cell and force transducer were surrounded by mullite wool that was fixed in an aluminium pot.

In case of experiments under uniaxial pressure the steel rod was led to the face of the upper tungsten carbide piston and pressure was built up successively by hand control of the electrical pump. Additionaly, intercalation experiments were conducted without applying uniaxial pressure. This was done in order to determine diffusivities and lithium contents at the crystal edges at ambient pressure. These data are directly comparable to experiments by Schwarzburger et al. [2012]. In these experiments the tungsten carbide piston was pressed manually onto the sample prior to the intercalation experiments.

The compressive force was measured with the load cell during the experiments. When the desired compressive force (between 0 to 3.9 kN) was reached, the valve to the oil hydraulic cylinder was closed to provide a constant oil pressure during the experiment. The pressure on the sample was calculated by division of the measured force by the crystal area yielding values between 0 and 885 MPa.

Due to fluctuations of the room temperature, which were < ± 2 K, the poles, on which the oil hydraulic cylinder was mounted, expanded and contracted during the experiments. This led to increasing pressure on the sample when the room temperature decreased, and vice versa decreasing pressure when the room temperature increased. The fluctuation was < ± 10 % of the applied pressure.

Simultaneously to the pressure buildup, the sample chamber was purged with argon gas through the cannulas and the cell was heated, by setting the temperature of the silicon foil to 311 K in all experiments. The measured temperature was between 304 and 307 K at the support plates and fluctuation of T was typically < ± 0.5 K originating from temperature oscillations in the room.

When pressure and temperature were constant approx. 0.5 mL of 1.6 M n-Buli in n-hexane was injected via one of the cannulas. The other cannula served as a pressure balance with an argon filled balloon connected over a syringe to the Luer taper of the cannula.

After the n-BuLi injection, purging of the cell was started, in order to provide a protective atmosphere inside the cylinder during the experiments. For this purpose, a third cannula was fed through one of the rubber stoppers in the lid of the cell. As the outer cylinder is not gas tight, the cell was purged with a constant gas flow during the experiment. The required flow rate was determined prior to the first intercalation experiment using a Hamilton VISIFERM DO ARC oxygen sensor, which was fed through a bore hole in a rubber stopper in the lid of the cell. The oxygen saturation in the cell was measured during purging of the cell at different argon gas flows. At a gas flow of approx. 0.3 mL / min, which was used in the intercalation experiments, the oxygen saturation in the cell reaches a constant value of approx. 1 % after approx. 7 minutes of purge time (Fig. 31).

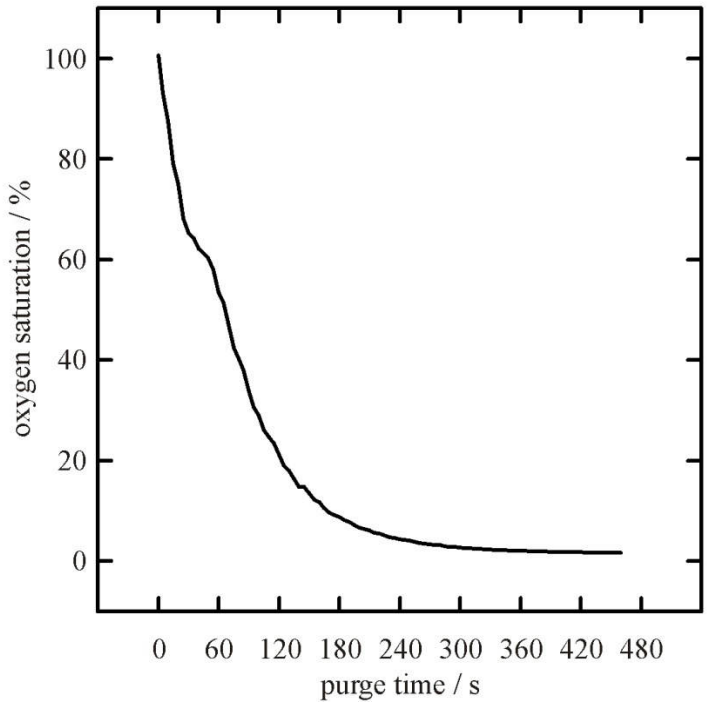


Fig. 31: Decrease of oxygen saturation ($pO_2$ relative to Air) during purging of the cell with an argon gas flow of 0.3 mL / min.

This procedure prevented reduction of n-BuLi reactivity due to reactivity with moisture and oxygen in case of possible leakages in the sample chamber. However, the solution was exchanged for fresh solution daily. This was done to ensure a constant volume of the solution in the sample chamber, which might have been reduced due to evaporation in case of leakages of the sample chamber. The solution that was drawn from the sample chamber was poured on a tissue to approve its reactivity. Reaction time was approx. 4 days.

At the termination of the experiments the sample chamber was flushed with n-hexane using the cannulas and the solution was drawn from the sample chamber. As the cannulas did not quite reach the base of the sample beaker, small amount of the solution remained in the sample chamber. However, the

n-BuLi concentration was very low, due to the preceding flushing. Then, the pressure was released, in case of experiments under uniaxial pressure. Subsequently, the cell was disassembled and the samples were cleaned with ethanol and transferred quickly into a liquid nitrogen container where they were stored until measurements to prevent further diffusion.

### D.2.3 Test measurement and determination of epoxy viscosity

Prior to the first intercalation experiment the cell was tested by compressing epoxy cylinders at the experimental temperature (approx. 304 K). This was done, in order to determine the flexibility of the epoxy during compression and study the flow behaviour.

Temperatures, displacement of the pistons and applied force were measured during the experiments. Fig. 32 shows the temperature profile of the test measurement. The temperature in the cell varies only slightly by 0.1 °C for this short period of time. In the intercalation experiments the temperature variation was slightly higher due to higher variations of the room temperature. Temperatures in the base plate and the upper piston differ by approx. 0.3 °C.

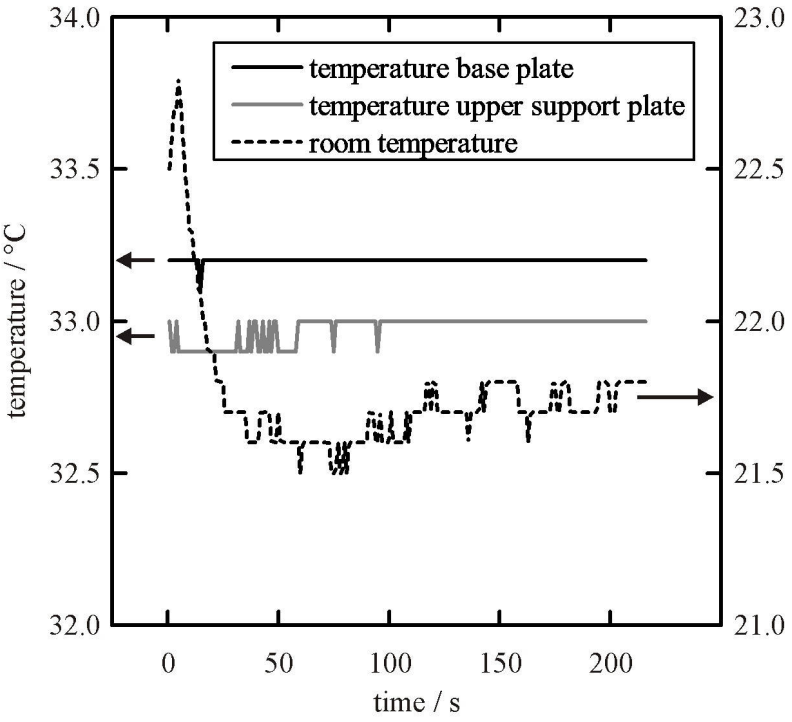


Fig. 32: Temperature profile of the test measurement. The time segment that is displayed is identical with the period displayed in Fig. 33.

The viscosity of the epoxy was determined from these experiments by the parallel plate technique [e.g. Barnes 1989]. Fig. 33 shows the documentation of the applied force onto a epoxy cylinder, the thickness change and the viscosity during the experiment.

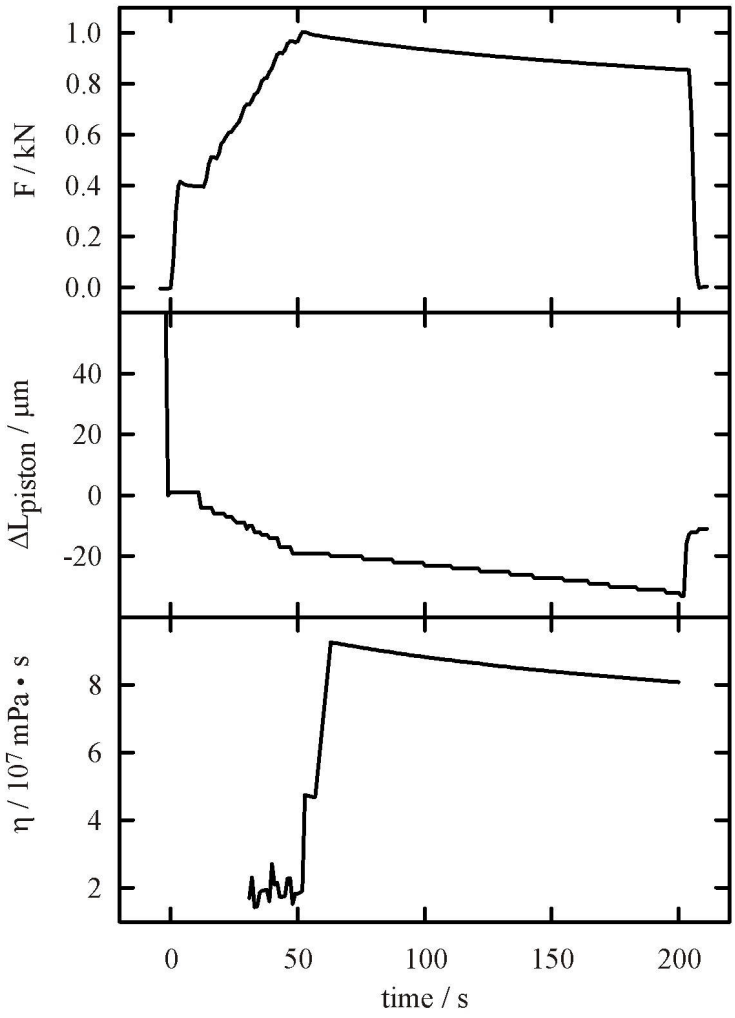


Fig. 33: Compression of an epoxy cylinder. The temperature at the sample position was approx. 33.2 °C. Initial sample thickness was $L_0$ = 330 µm and time of compression was $\Delta t$ = 207 s. The fast lowering at the beginning of the compression reflects settling of the cell components. Likewise the rebound, which is visible at the decompression, does not reflect a change in thickness of the epoxy. The development of the viscosity at the bottom of the figure was calculated in time increments of 10 s, based on the change in sample thickness measured in situ with the LVDT sensors. It should be noted that these measurements include elastic deformation of the sample (for details see text) at the beginning of the compression.

The pressure of the oil hydraulic cylinder was build up within approx. 50 seconds until the maximum force of approx. 1.0 kN was reached. This corresponds to a pressure of 85 MPa on the sample with initial face area of approx. 11.8 $mm^2$.

Subsequently the force decreased due to compression of the epoxy. For the calculation of the viscosity the arithmetic mean of the force was calculated from the beginning of the pressure build up to the pressure release, i.e. the time of pressurization $\Delta t$.

The measurement of the compression with the LVDT position sensors yielded a value of $\Delta L_0$ = 33 µm for the experiment shown in Fig. 33. The sample thickness was also measured before and after the pressurization with the Leica DC 610 microscope yielding a compression of $\Delta L_0$ = 20 µm. The difference can be explained by a contribution of elastic deformation that is measured with the LVDT sensors. Moreover, measurement of the cylinder diameter before and after the experiments using the microscope showed that the volume of the cylinder stayed constant.

The viscosity can be calculated with Equation 15:

$$\eta = \frac{F \cdot (L_0 - \Delta L_0)}{S_0 \cdot L_0 \cdot 3 \cdot \frac{\Delta \ln L}{\Delta t}} \qquad (15)$$

where η is the viscosity, $L_0$ is the initial thickness of the cylinder, $\Delta L_0$ is the change in thickness during compression, $S_0$ is the initial end face area, $\Delta \ln L$ is the difference of the natural logarithms of sample thicknesses before and after compression and $\Delta t$ is the time of sample compression.

The viscosity was determined in two individual experiments yielding values of $1.4 \cdot 10^7$ and $7.5 \cdot 10^7$ mPa · s (experiment displayed in Fig. 33), based on the changes in sample thickness, which were determined microscopically. The variation of the viscosities is probably due to different mixing ratios of base component and hardener of the epoxy, which vary by a factor of approx. ± 10 %.

The time-dependent viscosities (Fig. 33) that are calculated from in situ displacement measurements are lower (approx. $1 \cdot 10^7$ mPa · s) when the pressure is build up. At the time at which the maximum force is reached the calculated viscosity is approx. $9.3 \cdot 10^7$ mPa · s and decreases slowly to approx. $8.0 \cdot 10^7$ mPa · s at the time of decompression, i.e. a slightly thixotropic behaviour.

In either case, the viscosity of the epoxy is below the glass transition at $10^{15}$ mPa · s [e.g. Scholze 1988]. With respect to the intercalation experiments, it can be concluded that the epoxy encapsulation is deformed plastically upon pressure application. Thus, pressure spikes due to slight sample roughness and deviation from coplanarity should be evened out at the beginning of compression.

### D.2.4 Measurement of profiles using LA-ICP-MS and FTIR-spectroscopy

Content-distance profiles were measured using LA-ICP-MS to determine lithium diffusivities and lithium contents at the crystal edges. The measurement procedure is described in section B.4.

Some of the samples that were intercalated using the new cell were measured additionally using FTIR-spectroscopy after the experiments. The electrons that are transferred from lithium to the host structure lead to a shift of the plasma edge, just as free electrons that result from excess titanium lead to a shift of the plasma edge. This was observed by Rüscher [1997] for different values of x in $Ag_xTiS_2$.

The measurement of IR spectra parallel to LA-ICP-MS profiles should yield plasma frequencies that reflect a charge carrier concentration corresponding to the measured lithium content in addition to the electrons contributed by excess titanium of the sample. As the intercalated samples were encapsulated and the spectra should be recorded along profiles the procedure deviates from the FTIR measurements for the determination of excess titanium. The procedure is described in the following.

Before the FTIR measurements, samples were split parallel to the sheets by sticking adhesive tape on both basal planes and pulling it apart. Subsequently, recording of IR-spectra was possible on both fresh surfaces. A brass plate with bore holes was used as a sample holder by sticking the adhesive tape on the bottom side of the plate, so that the beam path could be directed through a hole onto the sample surface. The slit aperture of the microscope was adjusted to provide a narrow beam in the direction of the diffusion profile. The Bruker IFS 88 FTIR spectrometer is equipped with a motorized *x*-*y*-stage that allows setting the sample position on the micrometer scale and an IR-Scope II microscope. Profiles were measured parallel to the ablation lines of preceding fs-LA-ICP-MS measurements. Profiling started at the edge of the crystal. Single spectra were recorded with increasing distance to the crystal edges. Spectra were recorded consecutively and the corresponding sample positions were noted. Typical distances between individual spectra were usually between 5 and 50 µm. However, spectra were recorded more frequently close to the edge.

## D.3 Results and discussion

### D.3.1 Alteration of samples

Photographs of the sample surfaces parallel and perpendicular to the *ab-plane* were taken with a Leica DC 610 microscope to document changes of samples during experiment. The surface parallel to the *ab-plane* of a $TiS_2$ sample before an intercalation experiment is shown in Fig. 34a. It can be seen that

cracks developed during the experiment (Fig. 34b) due to mechanical stress. The edge of the crystal that was accessible to the solution was not damaged. Some of the intercalation experiments that were conducted at elevated pressures could not be evaluated because cracks developed on the whole area of the sample.

The mechanical stability depended on several factors, which varied for all samples. These are the coplanarity of the samples, the thickness of the encapsulation and the pressure applied onto the sample. Therefore, a clear statement concerning the stability of the samples in dependence of the applied pressure is difficult. It was possible to conduct intercalation experiments without total destruction of the sample at pressures below 885 MPa provided the thickness of the epoxy exceeded the deviation from coplanarity. Though, at least minor crack formation was observed at all samples intercalated under uniaxial pressure.

Compared to hydrostatic pressure experiments, the surfaces parallel to the *ab-plane* appeared to be less degraded by reaction with the solution. These surfaces are not in contact with the solution when pressure is applied onto the sample. But also at the experiments, in which no pressure was applied the degradation of the surfaces appeared to be significantly lower compared to hydrostatic experiments, indicating that the solution is less aggressive.

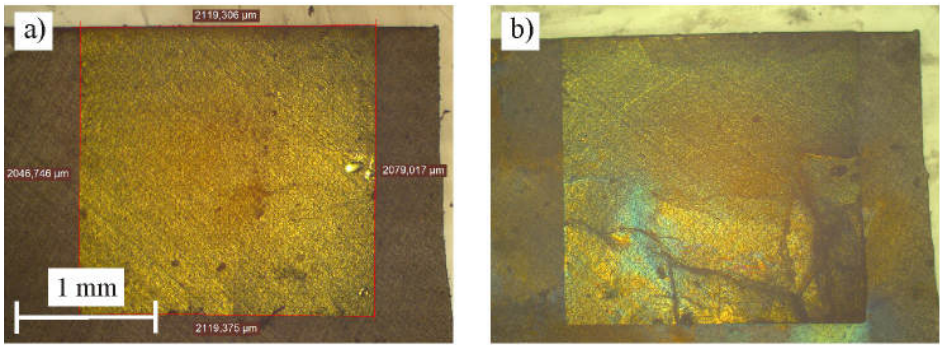


Fig. 34: Microscopical photographs of a crystal (sample $TiS_2$-R32) before (a) and after an intercalation experiment (b, P = 885 MPa, T = 305.0 K, t = 3.94 days). The photographs show the surfaces parallel to the *ab-plane*.

In addition photographs of the sample edges were taken (perpendicular to the *ab-plane*). All of the samples show split-ups along the $TiS_2$ sheets. This can occur during the termination of the experiments when the upper piston is lifted and the epoxy adhesive sticks to both pistons. In this case the splitting is parallel and often ranges over the entire width of the crystal edge. Moreover, cleavages can develop as a result of strain caused by inhomogenous insertion of lithium at the crystal edge. These cleavages are unsystematically distributed and vary in length from several micrometers to several hundreds of micrometers. However, it is difficult to distinguish between the different origins of the splitting on the basis of the microscopical images.

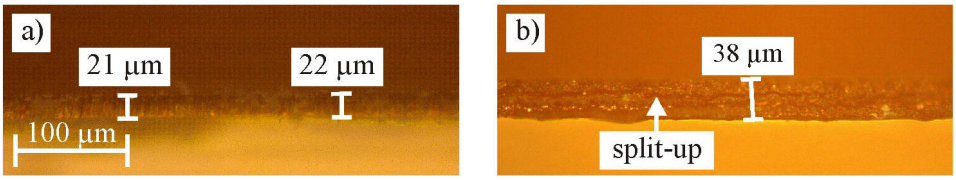


Fig. 35: Microscopical photographs (sample $TiS_2$-R32) before (a) and after an intercalation experiment (b, P = 885 MPa, T = 305.0 K, t = 3.94 days). The photographs show edges perpendicular to the *ab-plane*.

## D.3.2 Change in sample thickness

Changes in thickness of the samples were recorded during the experiments simultaneously with the applied force as well as room temperature and temperature measurements in the cell. Fig. 36 shows a time segment of room temperature, compressive force and displacement measurements during an in-

tercalation experiment. The upper piston moved downwards successively during all experiments. The movement occurred when the solution was drawn from the sample chamber and was in the range of 5 to 10 µm in total. A reason for the lowering of the upper piston can be thinning out of the epoxy adhesive. However, this should mainly occur at the beginning of the experiments and it is not clear how the movement of the piston is linked to drawing of the solution.

Microscopical images before and after the intercalation experiments mostly revealed a strong increase in sample thickness. Expansion of the titaniumdisulphide lattice due to intercalation is approx. 9 % at full intercalation while the observed increase in sample thickness was up to 100 %. This can be explained by the formation of cleavages between the sheets. As mentioned in the previous section, it is difficult to distinguish between cleavages resulting from intercalation induced strain and cleavages resulting from pulling the pistons apart at the termination of experiments. However, as long as pressure is applied, delamination of the sheets is suppressed. On the other hand formation of cleavages due to intercaltion induced strain is not counteracted in experiments at atmospheric pressure and large pathways for BuLi migration can develop during the experiment.

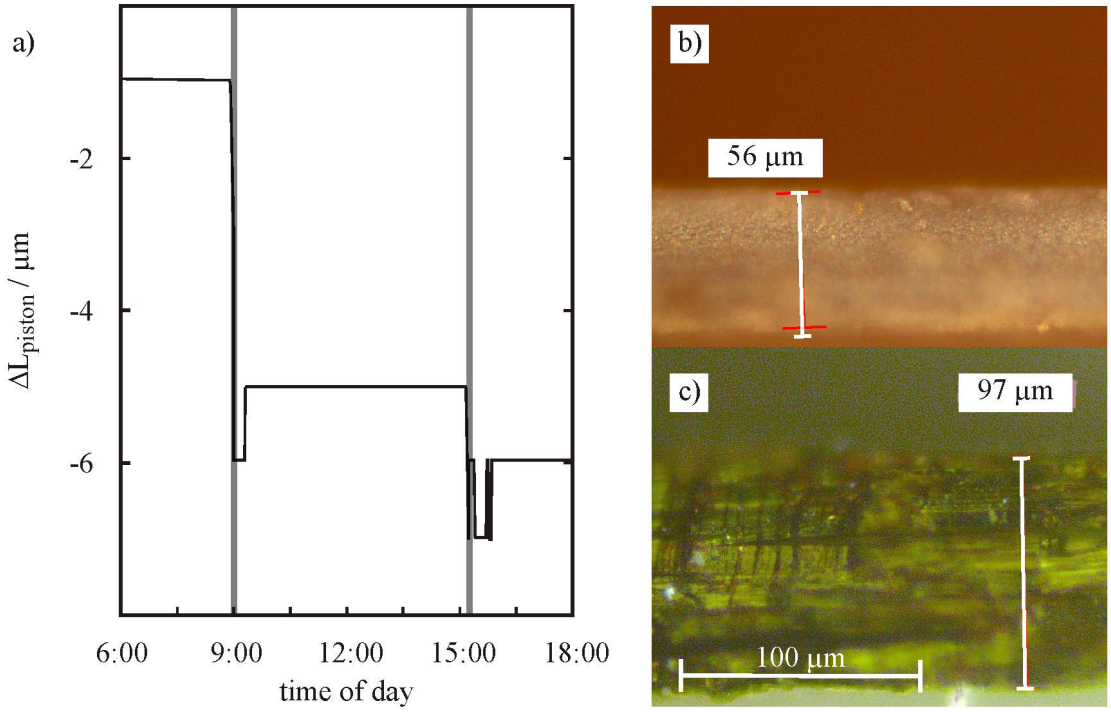


Fig. 36: Documentation of the change in thickness. a: Displacement of the upper piston during the intercalation experiment of sample R28 (T = 302.5 K, P = 410 MPa, t = 4.1 d). Grey lines mark the time of BuLi exchange. Fig. 6b and c: Microscopical images of the sample before (b) and after (c) the intercalation experiment.

### D.3.3 Selection of profiles

Typical examples of lithium content-distance profiles are displayed in Fig. 37. Fig. 37a shows profiles measured on a sample that was damaged mechanically during the experiment. Deviation from coplanarity led to strain and strong crack formation during the experiment. Samples that were damaged during the intercalation experiment were excluded from further evaluation. Fig. 37b shows profiles that could be fitted well with an error function and were used for further evaluation of diffusivities and lithium surface contents.

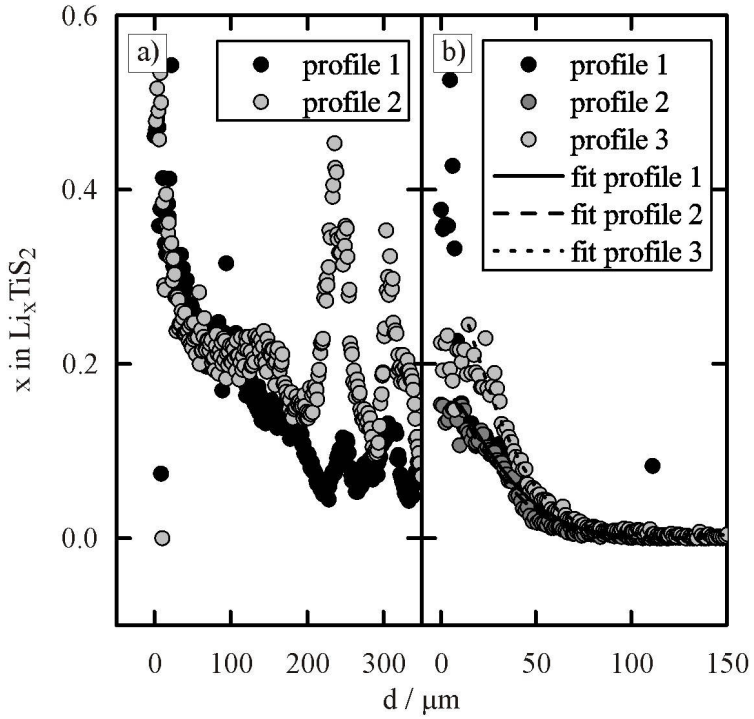


Fig. 37: Lithium Content-distance profiles on two different samples. a: sample R36, T = 303.8 K, P = 280 MPa, t = 3.9 d, 20 µm LASER spot diameter; b: sample R30, T = 304.6 K, P = 225 MPa, t = 4.4 d, 15 µm LASER spot diameter.

Profiles of a sample that was intercalated without application of uniaxial pressure are displayed in Fig. 38. The sample showed formation of cleavages parallel to the $TiS_2$ sheets. Cleavages are a pathway for rapid migration of BuLi solution between the $TiS_2$ sheets. This means that the zero point of diffusion is shifted into the crystals interior. In the measured profiles this results in a plateau with nearly constant lithium content at the edge of the crystal, which is followed by a decrease in lithium content with increasing depth that can be fitted well with an error function.

The part of the profile that exhibits error function shape was used in the further evaluation as it results from lithium diffusion being the predominant transport process. However, this procedure includes the assumption that there is a distinct zero point of diffusion, which is shifted into the crystals interior at the beginning of the intercalation experiment, which most likely is not the case. It is more probable that the boundary moves into the crystals interior with increasing experimental duration and that the position of the zero point varies locally depending on the corrosion. A mathematical description of this process is difficult. Modelling of the boundary progression could help to solve this problem. However, this is out of the scope of this work. The described procedure of evaluation introduces a systematic error, i.e. the derived diffusivities and lithium surface contents are too low.

The plateaus in content-distance profiles were observed at all samples, which had been intercalated at atmospheric pressure but also some samples that were intercalated under uniaxial pressure showed short plateaus.

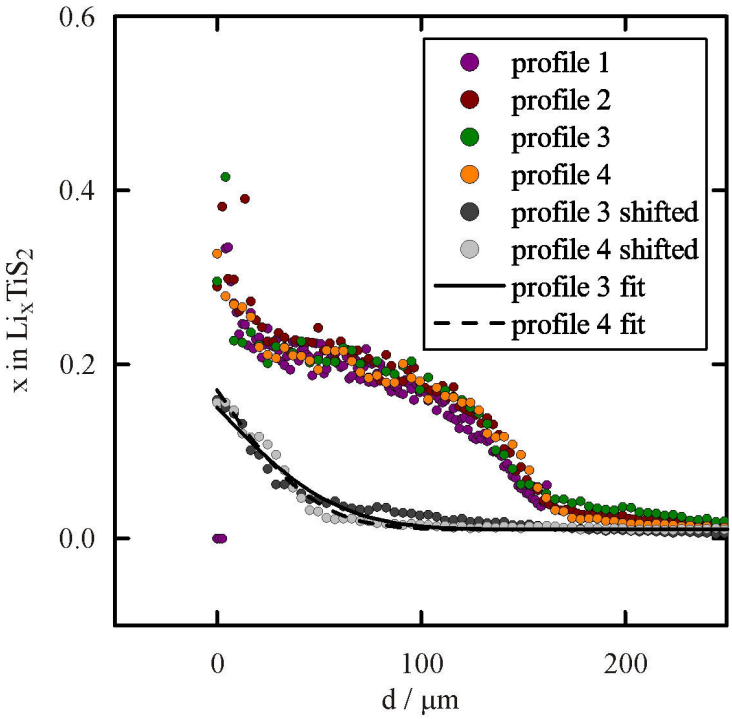


Fig. 38: Profiles measured on sample R37, T = 306.4 K, P = 1 atm, d = 4.0 d, 18 µm LASER spot diameter.

### D.3.4 Comparison of LA-ICP-MS and IR measurements

Fig. 39 shows content-distance profiles measured on a sample using LA-ICP-MS and IR-spectra that were recorded parallel to the LASER ablation lines. The sample was intercalated at atmospheric pressure and showed formation of cleavages after the experiment, but no cracks in the basal plane.

It can be seen that some of the profiles do not show an error function shape indicating that BuLi migration into the cleavages contributed to lithium transport into the sample. However, until a distance of d = 160 µm from the sample edge, the lithium content drops close to zero in all profiles (between x = 0.001 and 0.015). Thus, the profiles are only affected by BuLi migration at the edge of the crystal.

The IR-spectra that were measured parallel to the LA-ICP-MS profiles show a constant evolution towards the spectra of the sample before intercalation, i.e. the plasma edge is shifted towards lower wave numbers when going from the edge of the sample to the interior. It can also be seen that the spectra evolve strongly between 78 µm and 19 µm distance from the crystal edge, i.e. the region of the crystal that exhibits a high lithium concentration gradient. These observations could reflect a varying charge carrier concentration in dependence of the lithium concentration.

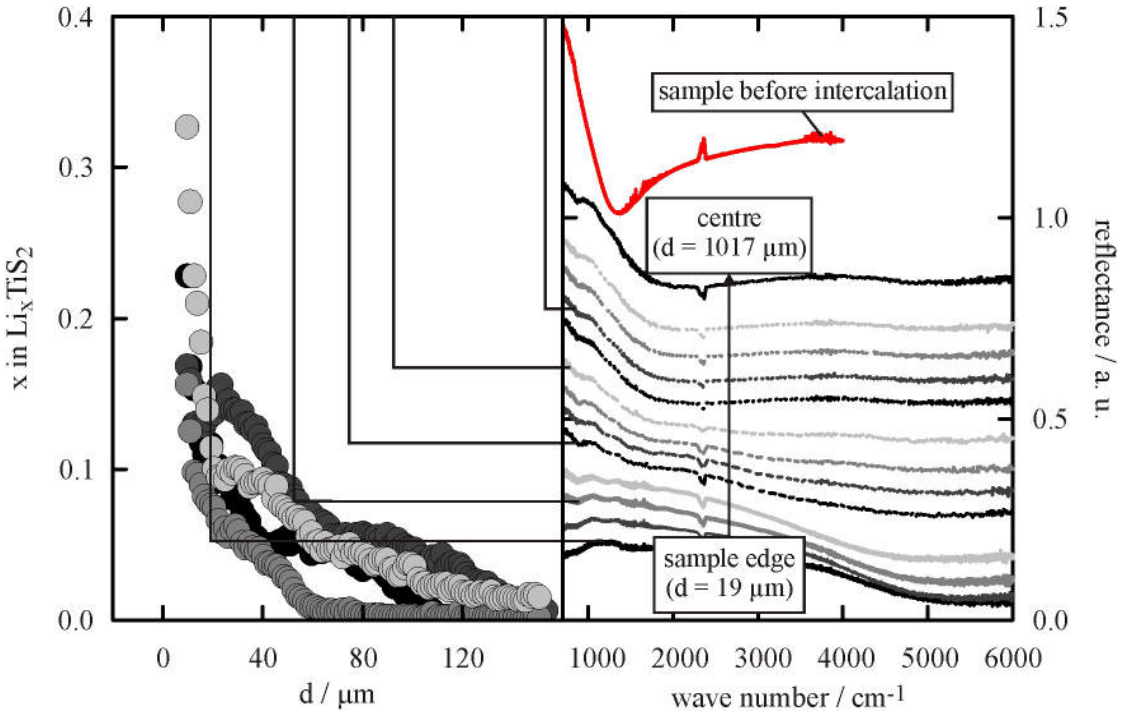


Fig. 39: Content-distance profiles and IR-spectra measured on sample R26 (T = 306.5 K, P = 1 atm, t = 3.9 d, 20 µm LASER spot diameter). All profiles were measured at the same edge of the sample. IR spectra were measured next to LA-ICP-MS profiles in a distance of approx. 300 µm.

Though, the IR-spectrum in the centre of the sample deviates strongly from the spectrum before intercalation, i.e. the plasma edge is shifted to a wave number of approx. 2000 $cm^{-1}$. It has to be kept in mind that the intercalated sample was cleaved prior to the IR measurement. Therefore, the reason for this observation could be that the amount of excess titanium was initially higher in the inner layers compared to the surface layers. The observed shift would correspond to a composition of $Ti_{1.013}S_2$.

Another reason for this observation could be that lithium is present in the centre of the intercalated sample. Assuming that each lithium atom contributes one free electron and the amount of excess titanium is identical to the amount that was determined at the surface prior to the intercalation, a content of x = 0.015 (the highest $x_{Li,0}$ value) would shift the plasma edge from 1332 $cm^{-1}$ to a wave number of $\nu$ = 1670 $cm^{-1}$. A lithium content of x = 0.015 in the centre of the sample seems improbable but cannot be ruled out as the spectra were recorded using a wide aperture which means that any crack or cleavage over a large volume that was analysed could have reached deep into the crystal.

Another explanation could be that charge carriers are not strictly located at the intercalated lithium ions at the sample edges but are distributed in the host lattice.

However, further conclusions require additional investigations and are out of the scope of this work.

### D.3.5 Effect of uniaxial pressure on lithium intercalation

A total of 12 samples were intercalated using the new intercalation cell, of which 6 experiments yielded lithium content-distance profiles that were of sufficiently high quality to be considered for the evalutation of $D_{Li}$ and $x_{Li,S}$. Of these experiments 3 were conducted under uniaxial pressure and 3 experiments were conducted at ambient pressure, i.e. the piston was pressed manually onto the sample prior to the start of the experiment (see section D.2.2). Table 6 gives an overview of the data that were finally considered.

Table 6: Overview of the data that were considered to determine values for $x_{Li,S}$ and $D_{Li}$. Suffixed digits denote different profiles that were measured on the same sample. The value of z is the ratio of beam diameter over profile length as explicated in chapter B.5.3. The non-stoichiometry of sample R30 was not determined (n. d.).

| sample | y in $Ti_{1+y}S_2$ | T / K | P / MPa | t / d | Analytical method | Spot diameter / µm | z | $x_{Li,0}$ | $x_{Li,S}$ | $D_{Li}$ / $m^2 \cdot s^{-1}$ | $\Delta D_{Li}$ / $m^2 \cdot s^{-1}$ |
|---|---|---|---|---|---|---|---|---|---|---|---|
| R26 | 0.0070 | 306.5 | 0.1 | 4.0 | LA-ICP-MS | 17 | 0.34 | 0.00 | 0.14 | $1.78 \cdot 10^{-15}$ | $0.25 \cdot 10^{-15}$ |
| R37.1 | 0.0070 | 306.4 | 0.1 | 4.0 | LA-ICP-MS | 18 | 0.28 | 0.01 | 0.15 | $3.03 \cdot 10^{-15}$ | $0.49 \cdot 10^{-15}$ |
| R37.2 | 0.0070 | 306.4 | 0.1 | 4.0 | LA-ICP-MS | 18 | 0.34 | 0.01 | 0.17 | $2.06 \cdot 10^{-15}$ | $0.30 \cdot 10^{-15}$ |
| R39 | 0.0069 | 306.3 | 0.1 | 4.0 | LA-ICP-MS | 15 | 0.28 | 0.00 | 0.16 | $2.00 \cdot 10^{-15}$ | $0.28 \cdot 10^{-15}$ |
| R30.1 | n. d. | 304.6 | 225.5 | 4.4 | LA-ICP-MS | 15 | 0.27 | 0.00 | 0.19 | $1.97 \cdot 10^{-15}$ | $0.33 \cdot 10^{-15}$ |
| R30.2 | n. d. | 304.6 | 225.5 | 4.4 | LA-ICP-MS | 15 | 0.29 | 0.00 | 0.19 | $1.68 \cdot 10^{-15}$ | $0.25 \cdot 10^{-15}$ |
| R32 | 0.0083 | 305.0 | 885.3 | 3.9 | LA-ICP-MS | 15 | 0.30 | 0.00 | 0.16 | $1.79 \cdot 10^{-15}$ | $0.25 \cdot 10^{-15}$ |
| R34.1 | 0.0080 | 305.5 | 595.6 | 4.0 | LA-ICP-MS | 14 | 0.35 | 0.01 | 0.12 | $1.13 \cdot 10^{-15}$ | $0.16 \cdot 10^{-15}$ |
| R34.2 | 0.0080 | 305.5 | 595.6 | 4.0 | LA-ICP-MS | 14 | 0.28 | 0.00 | 0.13 | $1.74 \cdot 10^{-15}$ | $0.25 \cdot 10^{-15}$ |

Diffusivities from uniaxial pressure experiments are in the range of 1.2 to $4.7 \cdot 10^{-15}$ $m^2 \cdot s^{-1}$ and $x_{Li,S}$ values are in the range of 0.12 to 0.22. A pressure of 885 MPa, which was the highest pressure that was applied in this study, is expected to reduce the diffusivity of Li in the crystal by a factor approx. 1.2 based on the ionic volume of lithium. This cannot be resolved due to the variation of the data, but is consistent with the determined diffusivities. It is worth repeating, that diffusivities that were determined using the pressure cell without application of pressure result from profiles, which were corrected by a shift of the zero point. This procedure includes the assumption that the boundary is shifted at the beginning of the experiment to a distinct plane parallel to the crystal edge, which is not realistic. The good agreement of the determined diffusivities and lithium surface contents could indicate that the assumptions are not far from actual progress of corrosion, i.e. the corrosion occurs mainly at the beginning of the experiment and the depth of corrosion is relative constant. However, to answer further investigations are required to draw conclusion about this progress (e.g. mathematic modelling).

Diffusivities and $x_{Li,S}$ values that were determined from hydrostatic and uniaxial pressure experiments are compared to data from Schwarzburger et al. [2012] in Fig. 40. Uniaxial pressure experiments were conducted at slightly elevated temperatures (around 305 K). The data from hydrostatic pressure experiments displayed in Fig. 40 were obtained from samples intercalated at 500 MPa for 5 and 20 days (no dependence of diffusivities or $x_{Li,S}$ values on time was observed).

Diffusivities of uniaxial pressure experiments are in the range of diffusivities determined at hydrostatic pressure experiments, while diffusivities from Schwarzburger et al. are elevated. Values of $x_{Li,S}$ determined from uniaxial pressure experiments are in the lower range of values determined from hydrostatic pressure experiments ($x_{Li,S}$ = 0.15 to 0.36). Lithium surface contents determined at ambient pressure by Schwarzburger et al. range from $x_{Li,S}$ = 0.05 to 0.35.

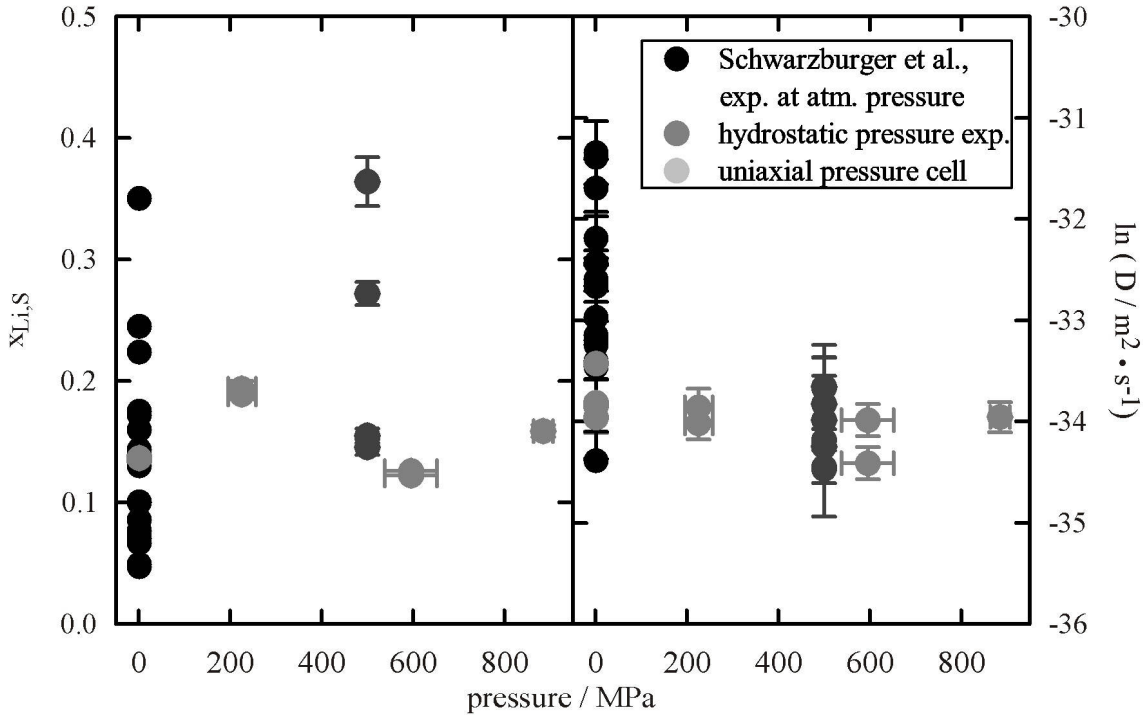


Fig. 40: Pressure dependence of lithium diffusivity and $x_{Li,S}$ in $TiS_2$.

Degradation was considerably weaker in the uniaxial pressure experiments compared to hydrostatic pressure experiments.

An explanation for the observations stated above could be that pressure applied on the solution leads to a higher BuLi activity and, as a consequence, a stronger degradation of the crystals at the edge and higher $x_{Li,S}$ values by trend. On the other hand $TiX_2$ sheets are stabilized with increasing pressure onto the crystal.

Similar observations were made in PART C of this thesis. In the hydrostatic pressure experiments samples that were intercalated at 10 MPa showed a stronger formation of cleavages compared to 500 MPa. In this study the formation of cleavages was also pronounced when no uniaxial pressure was applied. Moreover, $TiSe_2$ and $TiTe_2$ samples intercalated at hydrostatic pressure yielding higher $x_{Li,S}$ values compared to atmospheric pressure experiments by Schwarzburger [2013].

## D.4 Conclusion

The newly developed cell allows conducting intercalation experiments at high uniaxial pressures. The applicable pressure is practically limited by the stability of the samples. Generally, the mechanical stability depends on the quality of the crystals, the thickness of the epoxy encapsulation and the applied pressure. All samples used in this work showed deviation from coplanarity, which led to stress and, in most of the experiments, to a certain extent of crack formation. The highest pressure that was applied without destruction of the sample was 890 MPa. It can be expected that higher pressures are achievable given a high quality and coplanarity of the crystals.

Sample degradation due to reaction with the solution was reduced, compared to hydrostatic pressure experiments, which was assigned to the solution being under ambient pressure in the cell during the experiments.

Diffusion coefficients derived from the experiments under uniaxial pressure are in the range of hydrostatic pressure experiments. However, the variation of the data is slightly lower, which could be assigned to less degradation of the samples. Though, it was not possible to resolve a pressure dependence of lithium diffusivity in $TiS_2$ in the range of pressures applied.

# Summary

An experimental study of the intercalation kinetics of lithium into titanium dichalcogenide single crystals of composition $TiX_2$ (X = S, Se, Te) under pressure was conducted.

It was shown that the anion in the crystal structure has a strong influence on the stability of the structure during intercalation. $TiTe_2$ crystals were much more stable compared to the other dichalcogenides which was assigned to stronger interlayer bonding.

Differences in the structure of the chalcogenides also led to varying diffusivities and lithium contents at the crystal edges. Lower diffusivities in $TiTe_2$ were assigned to a higher barrier on the migration path because tellurium layers are closer to neutrality compared to the other dichalcogenides and thus, the transition state is less stable. Lithium distribution at the crystal edge was explained as a result of strain energy that is needed to expand the van der Waals gap. The highest strain is induced in $TiS_2$ during intercalation, leading to inhomogeneous insertion of lithium only at a fraction of available sites, i.e. already expanded sites are favored.

The application of pressure counteracted the fanning of the sheets which is indicated by a pressure dependent fraction of samples that exhibited solid state diffusion, i.e. formation of cleavages was stronger at low hydrostatic pressures.

A newly developed cell allowed conducting experiments at high uniaxial pressures without the solution being under pressure. The intercalated $TiS_2$ samples showed less degradation compared to hydrostatic pressure experiments and diffusivities and lithium surface contents showed lower variation.

A pressure effect on the diffusivities could only be resolved for the intercalation of $TiTe_2$ at hydrostatic pressures which is probably due to the higher compressibility of the structure.

# References

Aksoy R., Selvi E., Knudson R., Ma Y., J. Phys.: Condens. Matter, 21 (2009) 025403.

Allan D. R., Kelsey A. A., Clark S. J., Angel R. J., Ackland G. J., Phys. Rev. B, 57, 9 (1998) 5106.

Barnes H. A., Hutton J. F., Walters K., Rheology Series 3. An Introduction to Rheology. Elsevier, Amsterdam, 1989.

Bensch W. A., Bredow T., Ebert H. D., Heitjans P. B., Indris S. B., Mankovsky S.D., Wilkening M. B., Prog. Solid State Chem., 37, 2-3 (2009) 206.

Chianelli R. R., Scanlon J. C., Thompson A. H., Materials Research Bulletin, 10 (1975) 1379.

Chianelli R. R., Journal of Crystal Growth, 34 (1976) 239.

Clerc D. G., Poshusta R. D., Hess A. C., J. Phys. Chem., 100 (1996) 15735.

Clerc D. G., Poshusta R. D., Hess A. C., J. Phys. Chem. A, 101 (1997) 8926.

Crank J., The Mathematics of Diffusion, Oxford Univ. Press, Oxford, 2002.

Dahn J. R., McKinnon W. R., Haering R. R., Buyers W. J. L., Powell B. M., Canadian Journal of Physics, 58 (1980) 207.

Dahn J. R., Haering R.R., Solid State Communications, 40 (1981) 245.

Dahn J. R., Haering R. R., Solid State Communications, 42 (1982) 179.

Doublet M.-L., Gallego-Planas N., Philipsen P. H. T., Brec R., Jobic S., J. Chem. Phys., 108, 2 (1998) 649.

Eguchi T., Marinos C., Jonas J., Solid State Communications, 38 (1981) 919.

Fang C. M., de Groot R. A., Haas C., Phys. Rev. B, 56 (1997) 4455.

Folinsbee J. T., Simpson A. M., Jericho M. H., Mat. Res. Bull. 21 (1986) 961.

Friend R. H., Jérome D., Yoffe A. D., J. Phys. C: Solid State Phys., 15 (1982) 2183.

Hibma T., Physica, 99B (1980) 136.

Horn I., Günther D., Applied Surface Science, 207 (2003) 144.

Horn I., von Blankenburg F., Spectrochim. Acta, Part B, 62 (2007) 410.

Jaegermann W., Pettenkofer C., Schellenberger A., Papageorgopoulos C. A., Kamaratos M., Vlachos D., Tomm Y., Chem. Phys. Let., 221 (1994) 441.

Kim Y. S., Mizuno M., Tanaka I., Adachi H., Jpn. J. Appl. Phys., 37 (1998) 4878.

Kim Y., Park K., Song S., Han J. Goodenough J. B., J. Electrochem. Soc. 156 (2009) A703.

Kleinberg R. L., Silbernagel B.G., Sol. Stat. Comm. 36 (1980) 345

Klipstein P. C., Bagnall A. G., Liang W. Y., Marseglia E. A., Friend R. H., J. Phys. C: Solid State Phys., 14 (1981) 4067.

Klipstein P. C., Friend R. H., J. Phys. C: Solid State Phys., 17 (1984) 2713.

Klipstein P. C., Pereira C. M., Friend R. H., Phil Mag. B, 56 (1987) 531.

Kottke T., Stalke D., Angew. Chem. Int. Ed. Eng. 32 (1993) 580.

Lemmon E. W., McLinden M. O., Friend D. G., "Thermophysical Properties of Fluid Systems" in NIST Chemistry WebBook, NIST Standard Reference Database Number 69, Eds. P.J. Linstrom and W.G. Mallard, National Institute of Standards and Technology, Gaithersburg MD, 20899, http://webbook.nist.gov, (retrieved February 3, 2012).

Levy F., Subba Rao G. V., Shafer M. W., Intercalated Layered Materials, D. Reidel Publishing Company, Dor-drecht, Boston, London, 1979.

Liu B., Yang J., Han Y., Hu T., Ren W., Liu C., Ma Y., Gao C., J. Appl. Phys., 109 (2011) 053717.

Logothetis E. M., Kaiser W. J., Kukkonen C. A., Faile S. P., Colella R., Gambold J., J. Phys. C: Solid State Phys., 12 (1979) L521.

Matsumoto K., Nagai R., Solid State Ionics, 25 (1987) 233.

McKinnon W. R., Haering R. R., Solid State Ionics, 1 (1980) 111.

Mehrer H., Diffusion in Solids, Springer, Berlin, 2009.

Nagelberg A. S., Worrell W. L., J. Solid State Chem., 38 (1981) 321.

Patel S. N., Balchin A. A., Z. Kristallogr., 164 (1983) 273.

Patel S. N., Balchin A. A., J. Mat. Sci. Let., 4 (1985) 382.

Reshak A. H., Auluck S., Phys. Rev. B, 68 (2003) 245113.

Rimmington H. P. B., Balchin A. A., J. Cryst. Growth, 21 (1974) 171.

Rüscher C. H., Habilitation, University of Hannover, 1997.

Schärli M., Lévy F., Phys. Rev. B, 6 (1986) 4317.

Scholze H., Glas - Natur, Struktur und Eigenschaften, Springer, Berlin, 1988.

Schwarzburger N. I., Ph. D. thesis, University of Hannover, 2013.

Schwarzburger N. I., Knobel R., Behrens H., Binnewies M., Horn I., Pelster A., Arlinghaus H. F., Dörrer L., Schmidt H., Z. Phys. Chem. 226 (2012) 461.

Silbernagel B. G., Solid State Commun. 17 (1975) 361.

Stirling W. G. , Dorner M., Cheeke J. D. N., Revelli J., Solid State Commun., 18 (1976) 931.

Umrigar C., Ellis D. E., Wang D., Krakauer H., Posternak M., Phys. Rev. B, 26 (1982) 4935.

Whittingham M. S., Science, 192 (1976) 1126.

Whittingham M. S., Chemical Reviews, 104 (2004) 4271.

Wiegers G. A., Physica, 99 B (1980) 151.

Wilkening M., Ph. D. thesis, University of Hannover, 2005.

Wilkening M., Küchler W., Heitjans P., Phys. Rev. Letters, 97 (2006) 065901.

Wilkening M., Heitjans P., Phys. Rev. B, 77 (2008) 024311.

Wilson J. A., Barker A. S. Jr., Di Salvo F. J. Jr., Ditzenberger J.A. Phys. Rev. B, 18 (1978) 2866.

Winn D. A., Shemilt J. M., Steele B. C. H., Materials Research Bulletin, 11 (1976) 559.

Yamamoto T., Kikkawa S., Koizumi M., Solid State Ionics, 17 (1985) 63.

Yu Y. G., Ross N. L., J. Phys.: Condens. Matter, 23 (2011) 055401.

# Appendix

## PART B - Standard Compositions

### Hydrostatic pressure

Compositions of the standard that were produced for the measurement of intensity-distance profiles of samples intercalated at hydrostatic pressure after Schwarzburger [2013]. Based on the CS measurements for sulphur and ICP-OES for the other elements given the bulk compositions are $Li_{0.57}TiS_{1.87}$, $Li_{0.95}TiSe_2$ and $Li_{0.95}TiTe_{2.25}$. Errors are in the order of the third decimal place of the compositions.

| Chalcogenide | Analysemethode | Li / wt% | X / wt% | Ti / wt% |
|---|---|---|---|---|
| S | ICP-OES | 3.47 ± 0.01 | 55.43 ± 8.23 | 41.39 ± 0.19 |
| | CS-Analyse | ---- | 53.69 ± 0.27 | ---- |
| | EDX | ---- | 56.88 ± 0.23 | 42.42 ± 1.25 |
| Se | ICP-OES | 3.10 | 74.35 | 22.54 |
| | EDX | ---- | 75.02 ± 4.85 | 24.82 ± 5.06 |
| Te | ICP-OES | 1.93 ± 0.01 | 84.05 ± 1.7 | 14.02 ± 0.28 |
| | EDX | ---- | 83.27 ± 1.0 | 16.74 ± 1.0 |

### Uniaxial pressure

Compositions of the standard that were produced for the measurement of intensity-distance profiles of samples intercalated at uniaxial pressure after Schwarzburger [2013]. Based on the CS measurements for sulphur and ICP-OES for the other elements given the bulk composition of the standard is $Li_{0.91}TiS_{2.22}$. Errors are in the order of the third decimal place of the compositions.

| Chalcogenide | Analysemethode | Li / wt% | X / wt% | Ti / wt% |
|---|---|---|---|---|
| S | ICP-OES | 5.04 ± 0.03 | 56.77 ± 4.76 | 38.19 ± 0.03 |
| | CS-Analyse | ---- | 54.33 ± 0.38 | ---- |
| | EDX | ---- | 61.00 ± 0.87 | 38.92 ± 0.73 |

# PART C - Data of intercalation experiments at hydrostatic pressure

## $TiS_2$

Detailed overview of the data from intercalation experiments of $TiS_2$ at hydrostatic pressure. All samples were intercalated using 1.6 M BuLi. Intensity-distance profiles were measured using LA-ICP-OES. Errors for ΔP and Δt were constrained to be 5 MPa and 1800 s, respectively.

| sample | T / K | ΔT / K | P / MPa | t / s | z | Δz | $x_{Li,0}$ | $\Delta x_{Li,0}$ | $x_{Li,S}$ | $\Delta x_{Li,S}$ | $D_{meas}$ / $m^2/s$ | $\Delta D_{meas}$ / $m^2/s$ | $D_{Li}$ / $m^2/s$ | $\Delta D_{Li}$ / $m^2/s$ |
|---|---|---|---|---|---|---|---|---|---|---|---|---|---|---|
| N22 | 297.30 | 1.67 | 500 | 435900 | 1.78 | 0.39 | 0.01 | 0.00 | 0.27 | 0.01 | $2.18 \cdot 10^{-15}$ | $9.23 \cdot 10^{-16}$ | $1.34 \cdot 10^{-15}$ | $0.67 \cdot 10^{-15}$ |
| N23 | 297.30 | 1.67 | 500 | 435900 | 1.87 | 0.36 | 0.00 | 0.01 | 0.36 | 0.02 | $3.00 \cdot 10^{-15}$ | $1.13 \cdot 10^{-15}$ | $1.74 \cdot 10^{-15}$ | $0.81 \cdot 10^{-15}$ |
| N76.e.1. | 296.10 | 2.42 | 500 | 441000 | 1.21 | 0.23 | 0.01 | 0.00 | 0.16 | 0.01 | $2.48 \cdot 10^{-15}$ | $8.90 \cdot 10^{-16}$ | $2.04 \cdot 10^{-15}$ | $0.75 \cdot 10^{-15}$ |
| N76.e.2 | 296.10 | 2.42 | 500 | 441000 | 1.13 | 0.20 | 0.01 | 0.00 | 0.15 | 0.01 | $2.86 \cdot 10^{-15}$ | $9.58 \cdot 10^{-16}$ | $2.41 \cdot 10^{-15}$ | $0.82 \cdot 10^{-15}$ |
| R1.e | 297.60 | 1.85 | 500 | 1722960 | 0.56 | 0.06 | 0.01 | 0.00 | 0.26 | 0.00 | $2.49 \cdot 10^{-15}$ | $3.98 \cdot 10^{-16}$ | $2.39 \cdot 10^{-15}$ | $0.38 \cdot 10^{-15}$ |
| R10.1 | 297.60 | 1.54 | 500 | 1721940 | 0.78 | 0.11 | 0.01 | 0.00 | 0.26 | 0.01 | $1.16 \cdot 10^{-15}$ | $2.78 \cdot 10^{-16}$ | $1.07 \cdot 10^{-15}$ | $0.26 \cdot 10^{-15}$ |
| R10.2 | 297.60 | 1.54 | 500 | 1721940 | 0.7 | 0.10 | 0.01 | 0.00 | 0.25 | 0.01 | $1.16 \cdot 10^{-15}$ | $2.80 \cdot 10^{-16}$ | $1.09 \cdot 10^{-15}$ | $0.26 \cdot 10^{-15}$ |
| R10.3 | 297.60 | 1.54 | 500 | 1721940 | 0.66 | 0.08 | 0.01 | 0.00 | 0.2 | 0.00 | $1.51 \cdot 10^{-15}$ | $3.11 \cdot 10^{-16}$ | $1.42 \cdot 10^{-15}$ | $0.29 \cdot 10^{-15}$ |

Detailed overview of the data from intercalation experiments of $TiSe_2$ at hydrostatic pressure. All samples were intercalated using 1.6 M BuLi. Intensity-distance profiles were measured using LA-ICP-OES. Errors for ΔP and Δt were constrained to be 5 MPa and 1800 s, respectively.

| sample | T / K | ΔT / K | P / MPa | t / s | z | Δz | $x_{Li,0}$ | $\Delta x_{Li,0}$ | $x_{Li,S}$ | $\Delta x_{Li,S}$ | $D_{meas}$ / $m^2/s$ | $\Delta D_{meas}$ / $m^2/s$ | $D_{Li}$ / $m^2/s$ | $\Delta D_{Li}$ / $m^2/s$ |
|---|---|---|---|---|---|---|---|---|---|---|---|---|---|---|
| R5.e.1 | 296.30 | 2.42 | 10 | 442080 | 1.43 | 0.29 | 0.00 | 0.00 | 0.42 | 0.00 | $1.77 \cdot 10^{-15}$ | $6.76 \cdot 10^{-16}$ | $1.33 \cdot 10^{-15}$ | $0.54 \cdot 10^{-15}$ |
| R5.e.2 | 296.30 | 2.42 | 10 | 442080 | 1.38 | 0.27 | 0.00 | 0.00 | 0.57 | 0.03 | $1.91 \cdot 10^{-15}$ | $7.15 \cdot 10^{-16}$ | $1.47 \cdot 10^{-15}$ | $0.41 \cdot 10^{-15}$ |
| N15.1 | 297.90 | 3.05 | 300 | 432180 | 1.41 | 0.28 | 0.02 | 0.01 | 0.23 | 0.02 | $2.10 \cdot 10^{-15}$ | $7.90 \cdot 10^{-16}$ | $1.59 \cdot 10^{-15}$ | $0.63 \cdot 10^{-15}$ |
| N15.2 | 297.90 | 3.05 | 300 | 432180 | 1.35 | 0.25 | 0.02 | 0.00 | 0.45 | 0.02 | $2.31 \cdot 10^{-15}$ | $8.17 \cdot 10^{-16}$ | $1.79 \cdot 10^{-15}$ | $0.66 \cdot 10^{-15}$ |
| R1.e.1 | 296.10 | 2.42 | 500 | 439320 | 0.97 | 0.20 | 0.00 | 0.00 | 0.71 | 0.04 | $2.04 \cdot 10^{-15}$ | $7.62 \cdot 10^{-16}$ | $1.80 \cdot 10^{-15}$ | $0.68 \cdot 10^{-15}$ |
| R1.e.2 | 296.10 | 2.42 | 500 | 439320 | 0.94 | 0.18 | 0.00 | 0.00 | 0.66 | 0.02 | $2.16 \cdot 10^{-15}$ | $7.57 \cdot 10^{-16}$ | $1.93 \cdot 10^{-15}$ | $0.58 \cdot 10^{-15}$ |
| R15.e.1 | 296.40 | 2.00 | 500 | 1726560 | 0.78 | 0.09 | 0.03 | 0.01 | 0.71 | 0.01 | $1.94 \cdot 10^{-15}$ | $3.98 \cdot 10^{-16}$ | $1.79 \cdot 10^{-15}$ | $0.40 \cdot 10^{-15}$ |
| R15.e.2 | 296.40 | 2.00 | 500 | 1726560 | 0.61 | 0.07 | 0.05 | 0.01 | 0.67 | 0.01 | $2.16 \cdot 10^{-15}$ | $4.34 \cdot 10^{-16}$ | $2.06 \cdot 10^{-15}$ | $0.41 \cdot 10^{-15}$ |

Detailed overview of the data from intercalation experiments of $TiTe_2$ at hydrostatic pressure. All samples were intercalated using 1.6 M BuLi. The analytical method used for measurement of intensity-distance profiles is denoted in the table. Errors for ΔP and Δt were constrained to be 5 MPa and 1800 s, respectively.

| sample | T / K | ΔT / K | P / MPa | t / s | Analytical method | z | Δz | $x_{Li,0}$ | $\Delta x_{Li,0}$ | $x_{Li,S}$ | $\Delta x_{Li,S}$ | $D_{meas}$ / $m^2/s$ | $\Delta D_{meas}$ / $m^2/s$ | $D_{Li}$ / $m^2/s$ | $\Delta D_{Li}$ / $m^2/s$ |
|---|---|---|---|---|---|---|---|---|---|---|---|---|---|---|---|
| R5.e.1 | 296.30 | 2.20 | 10 | 438840 | OES | 1.55 | 0.12 | 0.01 | 0.00 | 1.00 | 0.06 | $7.18 \cdot 10^{-16}$ | $2.21 \cdot 10^{-16}$ | $5.1 \cdot 10^{-16}$ | $2.3 \cdot 10^{-16}$ |
| R5.e.2 | 296.30 | 2.20 | 10 | 438840 | OES | 1.72 | 0.15 | 0 | 0.00 | 0.97 | 0.04 | $6.72 \cdot 10^{-16}$ | $2.37 \cdot 10^{-16}$ | $4.3 \cdot 10^{-16}$ | $1.0 \cdot 10^{-16}$ |
| R5.e.3 | 296.30 | 2.20 | 10 | 438840 | OES | 1.47 | 0.16 | 0 | 0.00 | 0.93 | 0.12 | $6.30 \cdot 10^{-16}$ | $2.65 \cdot 10^{-16}$ | $4.6 \cdot 10^{-16}$ | $2.0 \cdot 10^{-16}$ |
| N15 | 296.90 | 3.00 | 300 | 433620 | OES | 1.83 | 0.14 | 0.03 | 0.00 | 0.82 | 0.01 | $7.26 \cdot 10^{-16}$ | $2.23 \cdot 10^{-16}$ | $3.0 \cdot 10^{-16}$ | $1.1 \cdot 10^{-16}$ |
| N16.1 | 296.10 | 3.00 | 300 | 433260 | OES | 1.81 | 0.15 | 0.04 | 0.00 | 0.74 | 0.02 | $6.96 \cdot 10^{-16}$ | $2.22 \cdot 10^{-16}$ | $3.8 \cdot 10^{-16}$ | $1.3 \cdot 10^{-16}$ |
| N16.2 | 296.10 | 3.00 | 300 | 433260 | OES | 1.81 | 0.16 | 0.03 | 0.00 | 0.76 | 0.03 | $6.58 \cdot 10^{-16}$ | $2.16 \cdot 10^{-16}$ | $2.3 \cdot 10^{-16}$ | $1.0 \cdot 10^{-16}$ |
| R4.e.1 | 297.40 | 2.42 | 500 | 438300 | OES | 2.18 | 0.31 | 0.04 | 0.00 | 1.00 | 0.15 | $2.33 \cdot 10^{-16}$ | $1.03 \cdot 10^{-16}$ | $1.0 \cdot 10^{-16}$ | $0.6 \cdot 10^{-16}$ |
| R4.e.2 | 297.40 | 2.42 | 500 | 438300 | OES | 2.11 | 0.26 | 0.03 | 0.00 | 1.00 | 0.03 | $2.27 \cdot 10^{-16}$ | $6.93 \cdot 10^{-17}$ | $5.6 \cdot 10^{-17}$ | $3.9 \cdot 10^{-17}$ |
| R12.e.1 | 297.20 | 2.20 | 500 | 1719780 | MS | 0.86 | 0.19 | 0 | 0.00 | 0.82 | 0.02 | $1.04 \cdot 10^{-16}$ | $3.06 \cdot 10^{-17}$ | $9.4 \cdot 10^{-17}$ | $3.0 \cdot 10^{-17}$ |
| R12.e.2 | 297.20 | 2.20 | 500 | 1719780 | MS | 1.29 | 0.28 | 0 | 0.00 | 1.00 | 0.12 | $4.65 \cdot 10^{-17}$ | $1.37 \cdot 10^{-17}$ | $3.7 \cdot 10^{-17}$ | $2.6 \cdot 10^{-17}$ |
| R12.e.3 | 297.20 | 2.20 | 500 | 1719780 | MS | 0.85 | 0.19 | 0.05 | 0.00 | 0.87 | 0.02 | $1.07 \cdot 10^{-16}$ | $3.31 \cdot 10^{-17}$ | $9.8 \cdot 10^{-17}$ | $3.0 \cdot 10^{-17}$ |
| R14 | 297.20 | 2.20 | 500 | 1719780 | MS | 0.41 | 0.14 | 0 | 0.00 | 0.59 | 0.02 | $1.97 \cdot 10^{-16}$ | $5.77 \cdot 10^{-17}$ | $1.9 \cdot 10^{-16}$ | $0.6 \cdot 10^{-16}$ |

# PART D - Data of intercalation experiments at uniaxial pressure

Detailed overview of the data from intercalation experiments of $TiS_2$ at uniaxial pressure. All samples were intercalated using 1.6 M BuLi. Intensity-distance profiles were measured using LA-ICP-MS. The error of Δt was constrained to be 600 s.

| sample | y in $Ti_{1+y}S_2$ | T / K | ΔT / K | P / MPa | ΔP / MPa | t / s | z | Δz | $x_{Li,0}$ | $\Delta x_{Li,0}$ | $x_{Li,S}$ | $\Delta x_{Li,S}$ | $D_{meas}$ / $m^2/s$ | $\Delta D_{meas}$ / $m^2/s$ | $D_{Li}$ / $m^2/s$ | $\Delta D_{Li}$ / $m^2/s$ |
|---|---|---|---|---|---|---|---|---|---|---|---|---|---|---|---|---|
| R26 | 0.007 | 306.54 | 0.17 | 0.1 | 0.0 | 348600 | 0.34 | 0.10 | 0.00 | 0.00 | 0.14 | 0.00 | $1.81 \cdot 10^{-15}$ | $2.56 \cdot 10^{-16}$ | $1.78 \cdot 10^{-15}$ | $0.25 \cdot 10^{-15}$ |
| R30.1 | - | 304.59 | 0.39 | 225.5 | 30.2 | 381024 | 0.27 | 0.09 | 0.00 | 0.00 | 0.19 | 0.01 | $1.99 \cdot 10^{-15}$ | $3.29 \cdot 10^{-16}$ | $1.97 \cdot 10^{-15}$ | $0.33 \cdot 10^{-15}$ |
| R30.2 | - | 304.59 | 0.39 | 225.5 | 30.2 | 381024 | 0.29 | 0.10 | 0.00 | 0.00 | 0.19 | 0.00 | $1.70 \cdot 10^{-15}$ | $2.49 \cdot 10^{-16}$ | $1.68 \cdot 10^{-15}$ | $0.25 \cdot 10^{-15}$ |
| R32 | 0.0083 | 304.97 | 0.53 | 885.3 | 21.5 | 340832 | 0.30 | 0.10 | 0.00 | 0.00 | 0.16 | 0.01 | $1.81 \cdot 10^{-15}$ | $2.50 \cdot 10^{-16}$ | $1.79 \cdot 10^{-15}$ | $0.25 \cdot 10^{-15}$ |
| R34.1 | 0.008 | 305.46 | 0.33 | 595.6 | 57.3 | 343800 | 0.35 | 0.13 | 0.01 | 0.00 | 0.12 | 0.00 | $1.15 \cdot 10^{-15}$ | $1.67 \cdot 10^{-16}$ | $1.13 \cdot 10^{-15}$ | $0.16 \cdot 10^{-15}$ |
| R34.2 | 0.008 | 305.46 | 0.33 | 595.6 | 57.3 | 343800 | 0.28 | 0.10 | 0.00 | 0.00 | 0.13 | 0.00 | $1.76 \cdot 10^{-15}$ | $2.55 \cdot 10^{-16}$ | $1.74 \cdot 10^{-15}$ | $0.25 \cdot 10^{-15}$ |
| R37.1 | 0.01 | 306.40 | 0.24 | 0.1 | 0.0 | 341728 | 0.28 | 0.08 | 0.01 | 0.00 | 0.15 | 0.00 | $3.07 \cdot 10^{-15}$ | $4.97 \cdot 10^{-16}$ | $3.03 \cdot 10^{-15}$ | $0.49 \cdot 10^{-15}$ |
| R37.2 | 0.007 | 306.40 | 0.24 | 0.1 | 0.0 | 341728 | 0.34 | 0.09 | 0.01 | 0.00 | 0.17 | 0.00 | $2.09 \cdot 10^{-15}$ | $2.99 \cdot 10^{-16}$ | $2.06 \cdot 10^{-15}$ | $0.30 \cdot 10^{-15}$ |
| R39 | 0.0069 | 306.35 | 0.49 | 0.1 | 0.0 | 348240 | 0.28 | 0.09 | 0.00 | 0.00 | 0.16 | 0.00 | $2.02 \cdot 10^{-15}$ | $2.85 \cdot 10^{-16}$ | $2.00 \cdot 10^{-15}$ | $0.28 \cdot 10^{-15}$ |

# Curriculum Vitae

## Robert Knobel


| | | | |
|---|---|---|---|
| Adress: | Viktoriastraße 37 | Date of birth: | 26th January 1983 |
| | 30451 Hannover | Marital status: | Unmarried |
| Phone: | 0179 - 1456596 | Nationality: | German |
| Email: | r.knobel@mineralogie.uni-hannover.de | | |
| | robert.kc@gmx.de | | |


## Work experiences and internships

| | |
|---|---|
| 04.2010 – 03.2013 | Research associate at the Insitute of Mineralogy, Leibniz Universität Hannover, Germany (LUH) |
| 10.2010. – 02.2013 | Teaching assistant for „Thermodynamics for geoscientists“ at the Institute for Mineralogy, LUH |
| 05.2009 – 03.2010 | Research associate at the Insitute of Production Engineering and Machine Tools, LUH |
| 09.2007 - 04.2009 | Student research assistant at the Institute of Mineralogy, Department of Crystallography, LUH |
| 07./08.2007 | Internship at the AMS Laboratory of the Scottish Universities Environmental Research Centre, East Kilbride, Glasgow, Scotland |
| 03./04.2007 | Internship at the Institute for Solarenergy Research Hamelin (ISFH) |
| 04.2006 - 07.2007 | Student research assistant at the Institute of Mineralogy, Department of Geochemistry, LUH |
| 03.2006 | Internship at the Department of „Mineral Economis“ at the Federal Institute for Geosciences and Natural Resources (BGR), Hannover |
| 10.2005 - 02.2007 | Undergraduate teaching assistant for „Chemistry for Geoscientists“, LUH |
| 09.2005 | Internship at the Department of „Raw Materials Research“ at the BGR , Hannover |
| 10.2004 | Internship at the Institute of Soil Science, LUH |

## Education

| | |
|---|---|
| 04.2010 - 03.2013 | PhD student at the Institute of Mineralogy, LUH |
| 10.2003 - 01.2008 | Diploma student of Geoscience at the LUH |
| | *(final grade: 1.3, „sehr gut“)* |
| Diploma thesis: | Synthesis and characterisation of Indium-subsituted, Mullite-like Bismuth Aluminates |
| 08.2002-05.2003 | Civil service at the German Red Cross, Celle |
| 06.2002 | German final secondary-school examination (Abitur), Gymnasium Ernestinum Celle (Germany) |